

Alma Mater Studiorum – Università di Bologna

DOTTORATO DI RICERCA IN
Scienze Biomediche e Neuromotorie

Ciclo XXXII

Settore Concorsuale: 05/E3

Settore Scientifico Disciplinare: BIO/12

ADVANCED NEUROIMAGING METHODOLOGIES TO IMPROVE
CONNECTIVITY DETECTION IN NORMAL AND ABNORMAL LANGUAGE
BRAIN NETWORKS

Presentata da: LIA TALOZZI

Coordinatore Dottorato

Prof. PIETRO CORTELLI



Supervisore

Prof.ssa CATERINA TONON



Co-supervisore

Dott.ssa CLAUDIA TESTA



Esame finale anno 2019

Dedicata ai miei genitori, Claudia e Giampaolo.

ACKNOWLEDGMENTS

Ringrazio le mie tutor di dottorato, la Prof.ssa Caterina Tonon per il suo entusiasmo per la ricerca e applicazioni cliniche, la Dott.ssa Claudia Testa per il suo rigore e approccio scientifico, grazie al loro continuo sostegno ho avuto la possibilità di formarmi e crescere.

Ringrazio il Prof. Raffaele Lodi, per la sua professionalità e per avermi dato la possibilità di approfondire le tematiche di neuroimaging che da sempre mi hanno appassionata. Ringrazio la Dott.ssa Stefania Evangelisti, per i suoi insegnamenti e sostegno; la Dott.ssa Micaela Mitolo, per avermi accompagnata nello studio del linguaggio. Ringrazio poi tutti i componenti del gruppo RM funzionale di Bologna, David Neil Manners, Ludovica Laura Gramegna, Claudio Bianchini e Lorenzo Cirignotta, sempre disponibili e vicini.

I would like to thank Prof. Marco Catani for introducing me to King's College London and make me part in his research projects. I would like to thank Dr. Stephanie Jacqueline Forkel, who taught me to be passionate about research, Dr. Flavio Dell'Acqua for his explanations on diffusion modelling, and all the Nat-BrainLab members, especially Ahmad Beyh.

Ringrazio infine la mia famiglia e in particolare i miei genitori, per aver sempre creduto in me, e i miei fratelli Marco e Livio. Ringrazio Agnese Garota per la sua amicizia, Mariangela Boe per i momenti assieme a Londra, Cecilia Maria Grini e Alba Latifi che anche se a distanza, le mie persone speciali.

ABSTRACT

The language connectome was *in-vivo* investigated using multimodal non-invasive quantitative MRI.

In PPA patients (n=18) recruited by the IRCCS ISNB, Bologna, cortical thickness measures showed a predominant reduction on the left hemisphere ($p < 0.005$) with respect to matched healthy controls (HC) (n=18), and an accuracy of 86.1% in discrimination from Alzheimer's disease patients (n=18). The left temporal and para-hippocampal gyri significantly correlated ($p < 0.01$) with language fluency.

In PPA patients (n=31) recruited by the Northwestern University Chicago, DTI measures were longitudinally evaluated (2-years follow-up) under the supervision of Prof. M. Catani, Kings College London. Significant differences with matched HC (n=27) were found, tract-localized at baseline and widespread in the follow-up. Language assessment scores correlated with arcuate (AF) and uncinate (UF) fasciculi DTI measures.

In left-ischemic stroke patients (n=16) recruited by the NatBrainLab, Kings College London, language recovery was longitudinally evaluated (6-months follow-up). Using arterial spin labelling imaging a significant correlation ($p < 0.01$) between language recovery and cerebral blood flow asymmetry, was found in the middle cerebral artery perfusion, towards the right.

In HC (n=29) recruited by the DIBINEM Functional MR Unit, University of Bologna, an along-tract algorithm was developed suitable for different tractography methods, using the Laplacian operator. A higher left superior temporal gyrus and pre-central operculum AF connectivity was found (Talozzi L et al., 2018), and lateralized UF projections towards the left dorsal orbital cortex.

In HC (n=50) recruited in the Human Connectome Project, a new tractography-

driven approach was developed for left association fibres, using a principal component analysis. The first component discriminated cortical areas typically connected by the AF, suggesting a good discrimination of cortical areas sharing a similar connectivity pattern.

The evaluation of morphological, microstructural and metabolic measures could be used as *in-vivo* biomarkers to monitor language impairment related to neurodegeneration as surrogate of cognitive rehabilitation/interventional treatment efficacy.

CONTENTS

Dedication	i
Acknowledgements	ii
Abstract	iii
Table of Contents	vii
1 Introduction to the language connectome and quantitative MRI	1
1.1 Multimodal characterisation of the language brain network	2
1.1.1 Structure of the thesis	3
1.2 Language mapping from lesion to disconnection syndromes	5
1.3 Language related pathologies	10
1.3.1 Primary Progressive Aphasia	10
1.3.2 Stroke-related aphasia	14
1.4 Quantitative MRI measures	16
1.4.1 Introduction to Magnetic Resonance Imaging	16
1.4.2 T1-w imaging and cortical thickness measure	19
1.4.3 Diffusion weighted imaging and micro-structural measures .	20
1.4.4 Arterial spin labeling and cerebral blood flow quantification .	24
1.5 White matter language network and tractography techniques	27
2 Cortical thickness neurodegeneration prospective	34
2.1 Differential analysis - PPA vs AD	35

2.2	Correlations with <i>category world fluency test</i> in PPA	45
3	Mapping white matter disconnections in Primary Progressive Aphasia	48
3.1	Language assessment	52
3.2	Evaluation of DTI metrics in the language network	57
3.3	PPA vs healthy controls - Language assessment and DTI metrics . . .	59
3.4	Mapping language disconnections	68
4	Metabolic plasticity in stroke-related aphasia	71
4.1	Registration of CBF maps to MNI	76
4.2	Vascular artery territories and Broca's ROIs	82
4.3	CBF statistics in healthy controls	83
4.4	CBF statistics stroke patients and AQ correlations	84
5	Arcuate and uncinate tractography in healthy controls	92
5.1	Bilateral AF automatic tractography with different methods	95
5.2	Bilateral UF automatic tractography	100
5.3	Along-tract analysis - Laplacian modelling	102
5.4	Hemispheric asymmetries	105
6	Tractography-driven cortical clustering - HCP dataset	112
7	Discussion	118
7.1	Language function neurodegeneration	119
7.2	Language recovery after stroke: MR biomarkers	124
7.3	Along-tract analysis and tractography driven cortical mapping in healthy controls	127

A	Language assessment and DTI metrics across PPA variants	134
B	Along-tract analysis of the arcuate fasciculus using the Laplacian operator to evaluate different tractography methods	141
	List of Tables	155
	List of Figures	157
	List of Abbreviations and Acronyms	160
	Bibliography	162
	Curriculum Vitae	176

CHAPTER 1

Introduction to the language connectome and quantitative MRI

1.1 MULTIMODAL CHARACTERISATION OF THE LANGUAGE BRAIN NETWORK

The investigation of the language network is in continuous evolution, there is an high interest in the scientific community to analyse pathophysiological mechanism underling language dysfunction in different pathologies (e.g. neurodegeneration and stroke), also the ongoing improvements of magnetic resonance imaging (MRI), hardware and software, offer new potentialities for *in-vivo* biomarker detection (Dick & Tremblay, 2012).

In my PhD project, I aimed to investigate the language network with a MRI multimodal approach, evaluating morphometric, microstructural and metabolic/functional biomarkers:

- cortical thickness measures on T1w structural images (Paragraph 1.4.2);
- micro-structural Diffusion Tensor Imaging (DTI) measures (Paragraph 1.4.3);
- Cerebral Blood Flow (CBF) quantification (Paragraph 1.4.4).

The proposed multiparametric approach aim to find accurate biomarkers to target language rehabilitation or interventional treatments (transcranial direct current stimulation - TDCS). To evaluate these measures in localised brain areas automatic pipelines were developed, both using brain atlases and performing white matter (WM) tractography reconstructions.

At the University of Bologna, Functional MR unit of the Department of Biomedical and Neuromotor Sciences, it was possible to evaluate MRI data acquired with a standardised protocol for different neurodegenerative pathologies, Alzheimer's disease (AD) and PPA, and address the clinical question of differential diagnosis in patients with dementia.

Subsequently, I studied different cohorts of subjects with a language multimodal investigation, and this was possible through the collaboration with both the King's College London, Tractography and Neuroanatomy Laboratory ([NatBrainLab](#)), expert for tractography (Catani et al., 2005) and language recovery after stroke (Forkel et al., 2014), and the Northwestern University, Cognitive Neurology and Alzheimer Center, pioneers in the clinical evaluation of Primary Progressive Aphasia (PPA) (Mesulam, 1982).

Through these collaborations, I had the opportunity to perform longitudinal evaluations of language dysfunctions, both on a neurodegenerative basis (Paragraph 1.3.1) and caused by ischemic stroke (Paragraph 1.3.2).

For healthy controls (HC) clinical DTI protocols were developed and acquired at the Functional MR unit of the Department of Biomedical and Neuromotor Sciences, University of Bologna, in the prospective of clinical applications.

Furthermore, I analysed open-source high-resolution DTI data acquired for healthy controls recruited within the Human Connectome Project initiative ([HCP](#)), evaluating the left hemisphere connectivity.

1.1.1 Structure of the thesis

In the current **Chapter 1**, an introduction to the language functions will be presented, focusing on degenerative and vascular clinics, MRI acquisition techniques and the language white matter network.

To achieve robust MRI biomarkers suitable for a single-patient study level, the thesis focused on correlations between MRI measures, both micro- and macro-structurally, and comprehensive neuro-psychological assessments for language.

Chapter 2, the category world fluency test (Novelli et al., 1986) was correlated with

cortical thickness measures in PPA. I evaluated retrospectively T1w images of PPA (n=18), AD (n=18) and HC (n=18), recruited by the IRCCS *Istituto Delle Scienze Neurologiche di Bologna* and the Functional MR unit of the Department of Biomedical and Neuromotor Sciences, University of Bologna.

Chapter 3, the Western Aphasia Battery Revised (Kertesz, 2007), the Peabody Picture Naming Test (Dunn et al., 2007), the Boston Naming Test (Kaplan et al., 2001), the Pyramids and Palm Tree Test (Howard & Patterson, 1992) and the Northwestern Anagram Verbs and Sentence (Cho-Reyes & Thompson, 2012) were correlated to language tract DTI measures for PPA patients and compared to HC. I analysed retrospectively DTI data acquired longitudinally, 2 years follow-up, of PPA (n=31) and HC (n=27), recruited by the Cognitive Neurology and Alzheimer Center of Northwestern University, Chicago (USA).

Chapter 4, the Western Aphasia Battery Revised was correlated to CBF measures in cerebral vascular arterial territories for stroke patients. I evaluated Arterial Spin Labelling (ASL) data longitudinally acquired, 6-months follow-up, of left ischemic stroke patients (n=16), and HC (n=14), recruited by the NatBrainLab Stroke team, King's College London (UK). Acquisition of stroke patients are still ongoing, thus preliminary results will be presented.

In the healthy control analysis, new algorithms were developed for tractography.

Chapter 5, an along-tract parameterisation of the arcuate and uncinate fasciculi was developed to evaluate hemispheric asymmetries for DTI measures and tract curvature. I evaluated T1w and DTI data of HC (n=29), recruited by the Functional MR unit of the Department of Biomedical and Neuromotor Sciences, University of Bologna.

Chapter 6, a tractography driven cortical clustering based on Principal Component Analysis (PCA) was developed to evaluate the whole left hemisphere connectivity, dominant in language processing. I evaluated DTI data of HC (n=50), recruited by the Human Connectome Project S900.

This PhD thesis aimed to present a comprehensive investigation of the language network, focusing on specific MRI quantitative measures and correlations between multimodal *in-vivo* biomarkers and clinical assessments.

Moreover, in all the presented analyses, new software developments have been proposed to realise automatic neuroimaging pipelines that can provide accurate and specific quantitative MRI biomarkers.

1.2 LANGUAGE MAPPING FROM LESION TO DISCONNECTION SYNDROMES

"M. Broca believes that disease of the left side of the brain only, produces loss of Language; and moreover, he locates the faculty of Articulate Language in a very limited part of that hemisphere. My observations tend to support the first hypothesis, and, in a general way, the second."

This writing by John Hughlings Jackson (1835 – 1911) (York & Steinberg, 2006) summarised the revolutionary idea for the nineteenth century that localisation of focal lesion of the brain can be a key for interpret patients' symptoms, as aphasia. It was a real breakthrough in the holistic conception of human cortex, where all brain areas were thought to work synergically (Zilles & Amunts, 2010).

In fact, the first association between specific brain areas and functions was about language, based on the discoveries of Paul Broca (1861) and Carl Wernicke (1874). P. Broca, a french neurosurgeon, studied brain anatomy of aphasic patients by

post-mortem investigation, identifying an area in the frontal lobe as responsible of speech production, the "Broca's area", located in the frontal inferior gyrus including posteriorly the pars opercularis and anteriorly the pars triangularis (Figure 1.1). Subsequently, C. Wernicke, a German Neurologist, identified the temporal lobe as responsible for auditory comprehension, the "Wernicke's area". He also postulated a "*psychic reflex arc*" between the temporal and frontal areas, not necessary the modern arcuate fasciculus, but a connection by an external capsule pathway. In the meantime, the German neuroanatomists Johann Christian Reil (1812) and Karl Friedrich Burdach (1822) identified a group of WM fibres arching around the Sylvian fissure, the arcuate fasciculus; also described by Joseph Jules Dejerine (1895) as the longitudinal fasciculus (Catani & de Schotten, 2012) (Figure 1.2).

These WM pathways were then investigated by Norman Geschwind (1972), evaluating translational studies in primates. N. Geschwind also characterised a third parietal area involved in language function, an association area for "*word meaning representation*", the Geschwind's area (Figure 1.3). He was the first to make the hypothesis of *dysconnection syndroms*, in which language deficits can arise from damages of connections between integrated brain regions with distributed functions. This was a second revolutionary prospective shift from focal lesion-language deficit paradigm to connection symptoms mapping.

Nowadays, it is possible to measure *in-vivo* what was theorised by Wernicke with MRI techniques, and address new questions about language, which is the characterisation of language dysfunctions in neurodegenerative diseases or how language recovers after stroke-induced aphasia.

Moreover, in 2005 a new concept of connectome was introduced by O. Sporns, G. Tononi and R. Kötter (Sporns et al., 2005), and independently by P. Hagmann in his

PhD thesis (Hagmann et al., 2007). The connectome is a matrix representation of brain connections, at different resolution scales and with different modalities, e.g. at a macroscale functional MRI (fMRI) can quantify a the functional connectome and DTI the structural connectome.

These new powerful mathematical tools have been used in many neuroscience applications (Sporns, 2010) and allow new multimodal brain cortex parcellation (Glasser et al., 2016).

In addition, even if it seems to be established that language functions are mainly processed in the left hemisphere (Dick & Tremblay, 2012), it is worth to investigate hemispheric differences of homologous areas. Interestingly, a recent research topic is how different tractography methods can influence tractography reconstruction of the arcuate fasciculus in the right hemisphere (Bain et al., 2019).

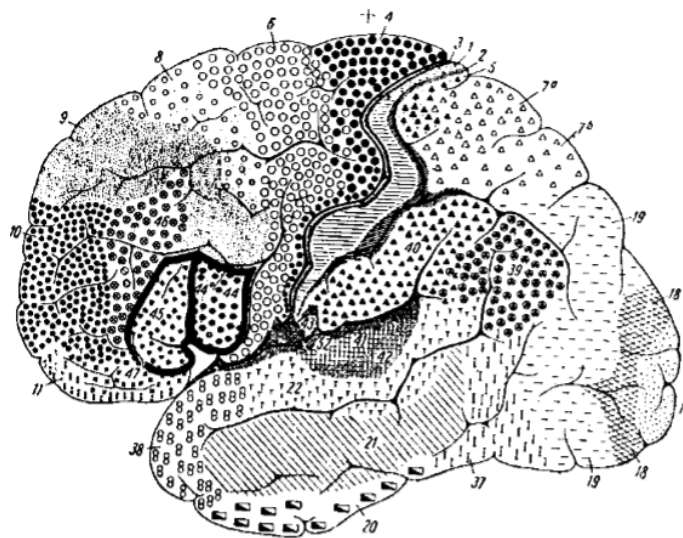


Figure 1.1: Cytoarchitectonic Brodmann areas.

Image from Amunts et al. (1999). Cytoarchitectonic mapping of human lateral brain surface, adapted from Brodmann (1909). Numbers are according Brodmann area classifications. The locations of areas 44 and 45 are indicated by bold lines.

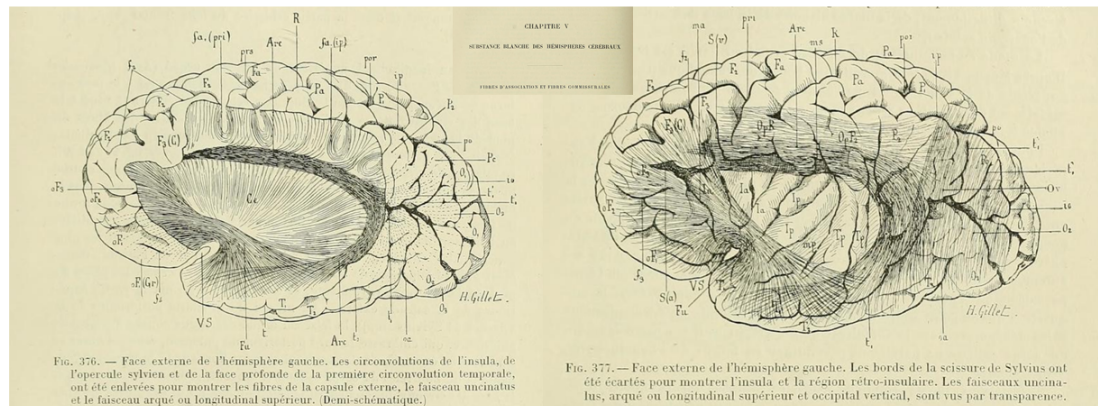


Figure 1.2: "Anatomie des centres nerveux" white matter fibre representation.

Images from pages 754 and 756 of [Anatomie des centres nerveux](#) by Dejerine & Dejerine-Klumpke (1895), representing the left hemisphere lateral view. **On the left:** fibres of the external capsule, the uncinatus fasciculus and arcuate or longitudinal fasciculi are shown. **On the right:** left hemisphere uncinatus fasciculus, the arcuate fasciculus or superior longitudinal fasciculus and the vertical occipital fasciculus are shown in transparency.

Arc, arcuate fasciculus or superior longitudinal fasciculus. - Ce, external capsule. - F2, F3, second and third frontal convolutions. - f2- f3, second and third (or H sulcus) frontal sulcus. - F3(C), Cape of the third frontal convolution. - f4, olfactory sulcus. - Fa, ascending frontal convolution. - fa(pri), U-shaped fibers of the inferior pre-Rolandic sulcus. - Fu, uncinatus fasciculus. - io, intra-occipital sulcus. - ip, intra-parietal sulcus. - O1, O2, O3, first, second and third occipital convolutions. - oF1, oF2, oF3, orbital part of the first, second, and third frontal convolutions. - oF1(Gr), rectus gyrus. - P1, P2, first and second parietal convolutions. - Pa, ascending parietal convolution. - Pc, pli courbe. - po, occipito-parietal fissure. - OpR, Rolandic opercula. - por, post-Rolandic sulcus. - pri, inferior pre-Rolandic sulcus. - prs, superior pre-Rolandic sulcus. - R, Rolando fissure. - T1, T2, first and second temporal convolutions. - t1, parallel or first temporal sulcus. - t'1, vertical branches of the parallel sulcus. - t2, second temporal sulcus. - Tp, deep temporal convolution. - VS, Valley of Sylvius. - S(a), S(v), anterior and vertical branches of the Sylvian fissure. - Ia, anterior insular convolution. - Ip, posterior insular convolution. - ma, anterior marginal sulcus. - mp, posterior marginal sulcus. - ms, superior marginal sulcus. - oa, anterior occipital sulcus of Wernicke. - OpP2, parietal opercula. - Ov, vertical occipital fasciculus.

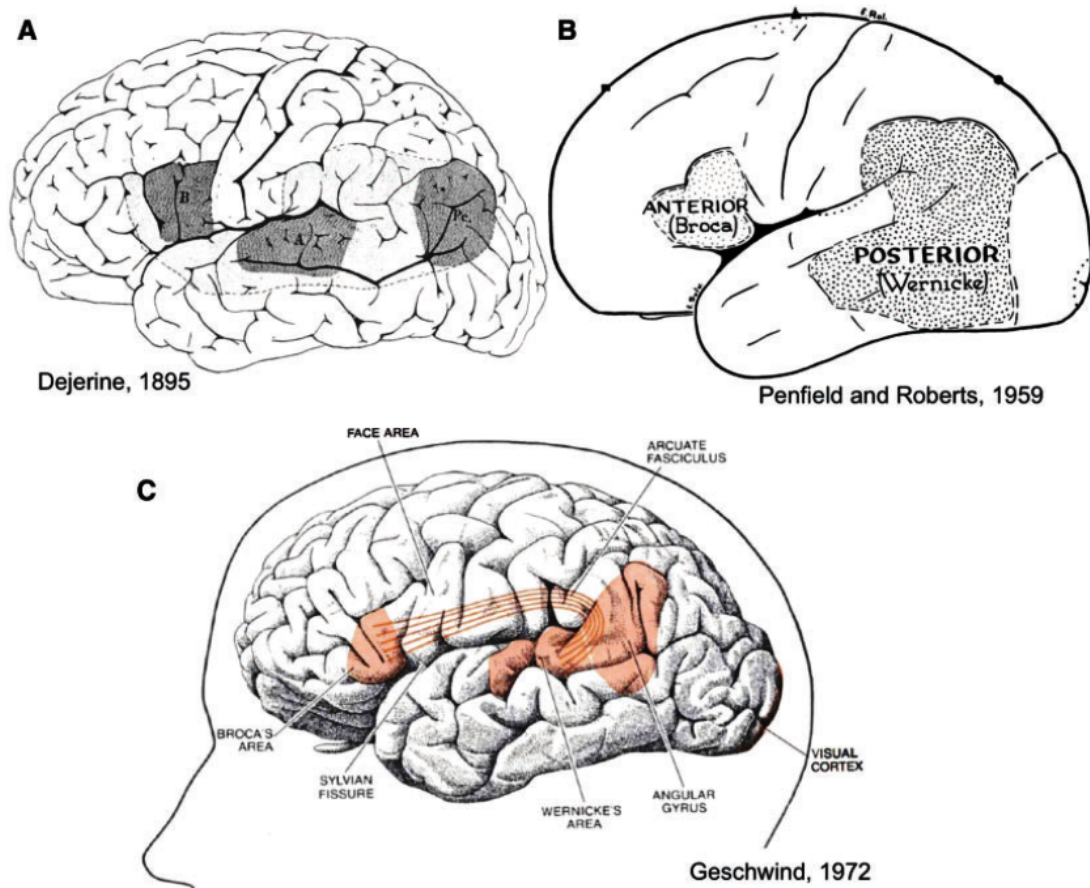


Figure 1.3: Broca-Wernicke-Geschwind language model.

from Mesulam et al. (2015). A panel: from Dejerine and Dejerine-Klumpke (1895) where the Wernicke's centre for auditory images of words is indicated with 'A', 'B' is the the Brocas centre for motor images of articulation and 'Pc' is the the centre for visual images of words. B panel: it is shown an evolution of the Wernicke's area definition by Penfield and Roberts (1959). C panel: The Geschwind connectivity representation of the arcuate fasciculus connecting these areas.

1.3 LANGUAGE RELATED PATHOLOGIES

1.3.1 Primary Progressive Aphasia

In the late nineteenth century, two psychiatrists, the Czech Arnold Pick (1892) and the French Paul Serieux (1893), described a progressive language disorder involving atrophy patterns in the frontal and temporal left hemisphere regions.

Subsequently, Mesulam (1982) described as first six patients who presented a progressive aphasia without a generalised dementia:

"The initial difficulty was an anomic aphasia in five of the patients and pure word deafness in the sixth. [...] Neurodiagnostic procedures were consistent with preferential involvement of the left perisylvian region." (Mesulam, 1982)

Starting from these observations, criteria to diagnosis PPA have been defined by Mesulam (2001, 2003) (Table 1.1).

Table 1.1: Primary Progressive Aphasia (PPA) diagnosis.

PPA diagnosis criteria (Mesulam, 2003):

Inclusion

criteria 1-3 must be answered positively

1. Most prominent clinical feature is difficulty with language;
 2. These deficits are the principal cause of impaired daily living activities;
 3. Aphasia should be the most prominent deficit at symptom onset and for the initial phases of the disease.
-

Exclusion

criteria 1-4 must be answered negatively for a PPA diagnosis

1. Pattern of deficits is better accounted for by other non-degenerative nervous system or medical disorders;
 2. Cognitive disturbance is better accounted for by a psychiatric diagnosis;
 3. Prominent initial episodic memory, visual memory, and visuo-perceptual impairments;
 4. Prominent, initial behavioural disturbance.
-

The early diagnosis of PPA is usually based on mild but persistent pauses in word-finding, which initially lead to a low-frequency in words production, or an impairment in object naming, some abnormalities in syntax, spelling and word comprehension errors (Rogalski & Mesulam, 2009).

The neuropsychological evaluation of PPA patients shows isolated language difficulties and preserved other cognitive domains and daily activity. On the contrary, personality changes are associated to the behavioural variant of fronto-temporal dementia (Rogalski & Mesulam, 2009).

Moreover, PPA patients can be categorised into different variants according to presented language impairment (Rogalski & Mesulam, 2009; Gorno-Tempini et al., 2011)

- semantic PPA (sPPA), characterised by a poor comprehension but a good syntax;
- agrammatic PPA (aPPA), presenting a partial overlap with non-fluent PPA, characterised by a poor syntax and fluency, but comprehension is preserved;
- logopenic PPA (lPPA), characterised by frequent pauses during word-finding, but syntax and word comprehension are preserved;
- mixed PPA is a form where patient can have both syntax errors and poor single word comprehension.

The classification of PPA into one of these variants may occur at one of three levels: clinical, imaging supported or definite pathologic diagnosis. Clinical diagnosis occurs when a case presents with speech and language features that are characteristic of a specific variant. In addition, clinical diagnosis criteria can be imaging-supported, when the typical structural and functional neuroimaging changes are

present. The third level, a definite pathology diagnosis, refers to cases that present with typical clinical characteristics (with or without neuroimaging evidence) of each variant and pathologic or genetic mutations associated with definite or Fronto Temporal Lobar Degeneration (FTLD) spectrum, AD, or other specific etiology.

Gorno-Tempini et al. (2011) consensus paper provide criteria for non-fluent/agrammatic, semantic and logopenic PPA diagnosis, which are respectively reported in Tables 1.2, 1.3 and 1.4.

The PPA variant characterisation is still in a evolving definition and also PPA patients may transit from a subtype to another in time (Rogalski & Mesulam, 2009). Definite pathology diagnosis may occur when there is a clinical diagnosis of PPA, and either histopathologic evidence of a specific neurodegenerative pathology (e.g., FTLD-tau, FTLD-TDP, AD, other) or presence of a known pathogenic mutation (Gorno-Tempini et al., 2011).

NON FLUENT/AGRAMMATICAL PPA VARIANT

Clinical diagnosis

At least one the following core features must be present

1. Agrammatism in language production;
2. Effortful, halting speech with inconsistent speech sound errors and distortions (apraxia of speech).

At least 2 of 3 of the following other features must be present:

1. Impaired comprehension of syntactically complex sentences;
 2. Spared single-word comprehension
 3. Spared object knowledge
-

Imaging-supported diagnosis

In addition to clinical diagnosis, imaging must show one or more of the following results:

- a. Predominant left posterior fronto-insular atrophy on MRI or
 - b. Predominant left posterior fronto-insular hypoperfusion or hypometabolism on SPECT or PET.
-

Table 1.2: Non-fluent or agrammatical Primary Progressive Aphasia (PPA) variant clinical and imaging-supported diagnosis (Gorno-Tempini et al., 2011).

SEMANTIC PPA VARIANT

Clinical diagnosis

Both of the following core features must be present:

1. Impaired confrontation naming;
2. Impaired single-world comprehension.

At least three of the following diagnostic features must be present:

1. Impaired object knowledge, particularly for low-frequency or low-familiarity items;
 2. Surface dyslexia or dysgraphia;
 3. Spared repetition;
 4. Spared speech production (grammar and motor speech).
-

Imaging-supported diagnosis

In addition to clinical diagnosis, imaging must show one or more of the following results:

- a. Predominant anterior temporal lobe atrophy;
 - b. Predominant anterior temporal hypoperfusion or hypometabolism on SPECT or PET.
-

Table 1.3: Semantic Primary Progressive Aphasia (PPA) variant clinical and imaging-supported diagnosis (Gorno-Tempini et al., 2011).

LOGOPENIC PPA VARIANT

Clinical diagnosis

Both of the following core features must be present:

1. Impaired single-word retrieval in spontaneous speech and naming;
2. Impaired repetition of sentences and phrases.

At least 3 of the following other features must be present:

1. Speech (phonologic) errors in spontaneous speech and naming;
 2. Spared single-word comprehension and object knowledge;
 3. Spared motor speech;
 4. Absence of frank agrammatism.
-

Imaging-supported diagnosis

In addition to clinical diagnosis, imaging must show at least one of the following results:

- a. Predominant left posterior perisylvian or parietal atrophy on MRI;
 - b. Predominant left posterior perisylvian or parietal hypoperfusion or hypometabolism on SPECT or PET.
-

Table 1.4: Logopenic Primary Progressive Aphasia (PPA) variant clinical and imaging-supported diagnosis (Gorno-Tempini et al., 2011).

1.3.2 Stroke-related aphasia

Language dysfunctions may occur after stroke, in particular aphasia is present in 21 – 38 % of acute stroke (Berthier, 2005). Stroke-induced aphasia significantly negatively impacts quality of life and speech-language therapy remains the mainstay treatment for these patients (Berthier, 2005).

Aphasia is typically correlated to ischemic or hemorrhagic stroke of the middle cerebral artery (MCA) which supplies the medial regions, insula cortex and frontal operculum areas, involved in language processing (Figure 1.4).

Stroke can be divided into two main categories:

- ischemic stroke: arterial occlusion (84%);
- haemorrhagic stroke (16%) affecting brain parenchyma divided in intracerebral and subarachnoidal haemorrhage.

Neurological symptoms can be: motor, sensory, behavioural, cognitive or behavioural on the basis of the vascular territory involved.

Aphasia typically occurs when the stroke is located in the left hemisphere, dominant for language, and in rare cases of "*cross aphasia*" the lesion is present in the right hemisphere.

Historically, stroke-induced aphasia may have two clinical aphasia presentations:

- Broca-type, impairment of the grammatical system and in sequencing of articulatory movements required for speaking (apraxia);
- Wernicke-type, impairment in the lexical/semantic systems.

Recently, Ardila (2010) proposed a reclassification of aphasic syndromes considering: primary language impairment (central aphasia), secondary language disturbances (peripheral aphasia) and executive control impairments (dysexecutive aphasia).

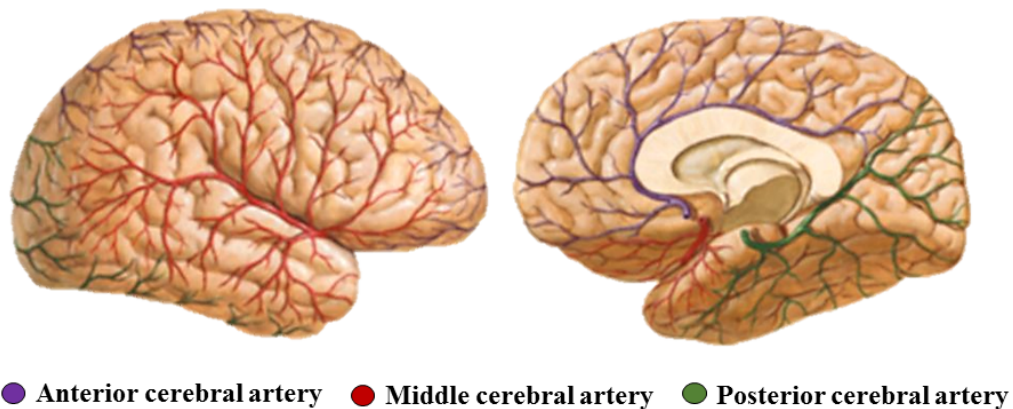


Figure 1.4: Cerebral vascular artery territories.

Images modified from Netter (2019) representing the blood supply of the brain by the cerebral arteries (anterior, middle and posterior). Lateral (left) and medial (right) views.

Type	Impairment
Primary (central) aphasia	Language system impaired
Wernicke-type (fluent aphasia)	Phonological level, Lexical level, Semantic level
Broca-type (non-fluent aphasia)	Sequencing expressive elements at syntactic and phonetic level
Secondary (peripheral) aphasia	Mechanisms of production impaired
Conduction aphasia	Disconnection (or segmentary ideomotor verbal apraxia)
SMA aphasia	To initiate and maintain voluntary speech production
Dysexecutive aphasia	Language executive control impaired
Extra-Sylvian (transcortical) motor aphasia	Executive control of language

Table 1.5: Ardila (2010) classification of aphasia syndromes.

1.4 QUANTITATIVE MRI MEASURES

1.4.1 Introduction to Magnetic Resonance Imaging

MRI is a multimodal imaging technique, changing the acquisition scheme is possible to appreciate different contrasts in brain tissues, e.g. grey matter (GM) and WM, and also measure specific tissue properties, such as proton diffusivity and arterial blood perfusion. This MRI flexibility and sensitivity is a powerful tool in the detection of brain tissue abnormalities.

Additionally, MRI is a *non invasive* technique, contrarily to PET or X-ray imaging, MRI does not employ ionising radiation. The MRI physics exploited the resonance between molecular protons (H^1) and radiofrequency (RF) waves (frequency range of MHz), described by the Larmor frequency law:

$$\omega_{Larmor} = \gamma B_0 \quad (1.1)$$

where γ is the gyromagnetic ratio characteristic of the proton nuclei H^1 : $\gamma = 42.58 \frac{MHz}{T}$ and B_0 is the external static magnetic field (e.g. 1.5T or 3T).

Proton spin orientation can be manipulated by applying an external electromagnetic fields with frequency ω_{Larmor} and a significant signal emerges from the sum of the all affected proton fields. Changing in spin orientations can be measure though the interaction of the protons' magnetic fields with a coil detector, described by the Faraday's law of electromagnetic induction.

Moreover, in the evaluation of the MRI signal it is important to consider the interaction of proton spins and the neighbouring atoms, resulting in changing of H^1 spin precession frequency.

Protons are part of an atom lattice, with which are in thermal contact. In terms, of quantum language, a spin exchange a quantum of energy with the lattice, resulting in a reduction of the longitudinal component of the proton local magnetic moment per unit volume, or magnetisation: $\vec{M}(\vec{r}, t)$.

The rate of change of the longitudinal component $dM_z(t)/dt$ is proportional to a constant, empirically defined (T_1):

$$\frac{dM_z}{dt} = \frac{1}{T_1}(M_0 - M_z) \quad (1.2)$$

where M_0 is the magnetisation equilibrium value, M_z is the longitudinal component and T_1 is the empirically defined "spin-lattice relaxation time". The integration of Eq. 1.2 results in the exponential decay of the magnetisation longitudinal component:

$$M_z(t) = M_z(0)e^{t/T_1} + M_0(1 - e^{t/T_1}) \quad (1.3)$$

Variations in local magnetic fields will influence the spin precessional frequencies, causing a spin fanning out over time and a reduction of the transverse magnetisation component (M_{xy}). This transverse decay is described by another empirical parameter: the "spin-spin" relaxation time T_2 :

$$M_{xy}(t) = M_{xy}(0)e^{t/T_2} \quad (1.4)$$

In addition, spin dephasing is caused by inhomogeneities of the external magnetic field, described by a separate decay time T_2' . Thus, the total M_{xy} relaxation rate will be described by:

$$\frac{1}{T_{2*}} = \frac{1}{T_2} + \frac{1}{T_2'} \quad (1.5)$$

Considering both the Eq. 1.3 and 1.4, the vector equation of the magnetisation equation is defined by the empirical law, known as the "Bloch equation":

$$\frac{d\vec{M}}{dt} = \gamma\vec{M} \times \vec{B}_{ext} + \frac{1}{T_1}(M_0 - M_z)\hat{z} - \frac{1}{T_2}\vec{M}_{xy} \quad (1.6)$$

Longitudinal and transverse relaxation behaviours can be manipulated to obtain different contrasts between tissues in MRI, such as T1-weighted (T1w) or T2-weighted (T2w) images. To accomplish this, RF fields are applied for a short time, thus are called RF pulses, and consequently the magnetisation vector rotates away from the alignment along the B_0 static magnetic field. A $\pi/2$ pulse will rotate the \vec{M} in a direction orthogonal to B_0 , and a π pulse will invert the precession orientation of the proton spins.

Other important parameters in the collection of the MRI signal are:

- the timing on which the signal is acquired with respect to the application of

the RF pulse, time of echo (TE).

- the timing that is given to proton spin to achieve to the magnetisation equilibrium, time of relaxation (TR);

where $TE \ll TR$, and the measure signal is given by the Bloch equation solution (Eq. 1.6) at TE.

Each MRI modality is characterised by a specific RF pulse sequence, where the acquisition imaging parameters are defined. Subsequently, further spin manipulation are needed to obtain a 3D volume imaging. To this purpose additional magnetic gradients are used to associate a spatial position to specific phase and frequency spin precession. A conventional 3D imaging approach is acquiring 2D images along a slice select direction by phase encoding.

In the following paragraphs, I will introduce the MRI sequences used in the characterisation of the language network.

1.4.2 T1-w imaging and cortical thickness measure

To obtain a T1-w MRI imaging, appropriate choices of TE and TR must be taken. If we consider a spin-echo sequence, in which first a $\pi/2$ pulse is applied and subsequently a π pulse, the MRI signal will be given by following formula:

$$S = N(H)(1 - e^{TR/T_1})e^{TE/T_2^*} \quad (1.7)$$

where if $TE \ll T_2^*$, thus $e^{TE/T_2^*} \rightarrow 1$, leading to a MRI signal mostly weighted on T1 relaxation time.

Using automated method from T1w images, it is possible to extract cortical thickness measures, defined as the distance between brain pial surface and the

GM-WM interface (Figure 1.5). Cortical thickness measures can be used to detect focal atrophy in small cohort of patients or even in individual subjects (Fischl & Dale, 2000).

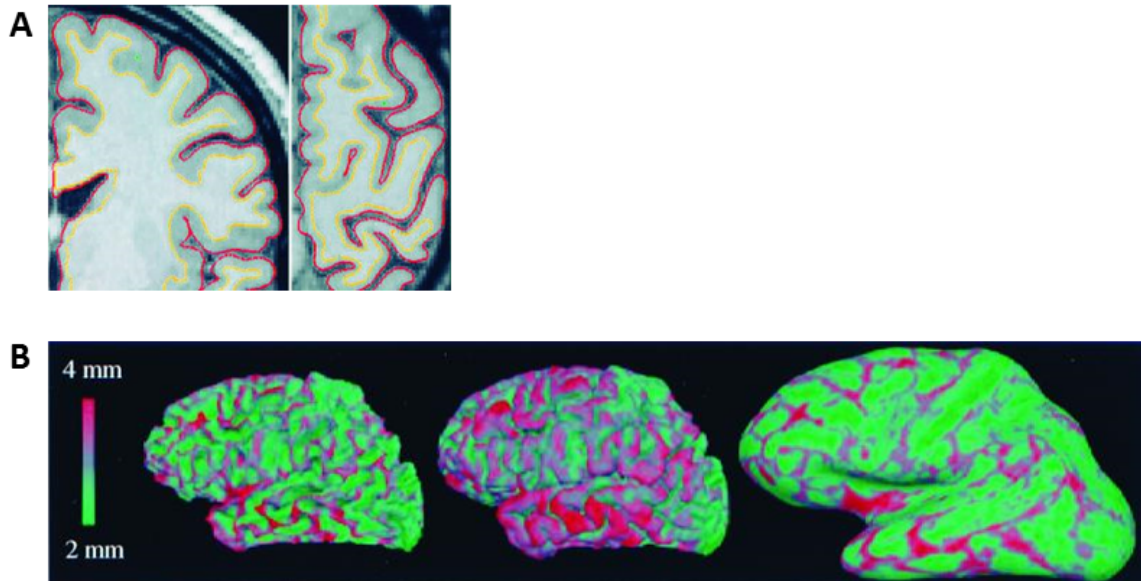


Figure 1.5: Cortical thickness measure extraction.

Figure adapted from Fischl & Dale (2000). **Panel A:** Coronal (left) and axial (right) slices of the left hemisphere. Overlapped to T1w image, in yellow the grey-white matter interface and in red the pial surface. **Panel B:** later view of three-dimensional surface reconstruction of grey-white matter (Left), pial (Center) and inflated (Right) surface representation. Overlaid, cortical thickness measures.

1.4.3 Diffusion weighted imaging and micro-structural measures

Albert Einstein (1905) in his PhD thesis described molecular self-diffusivity, expanding the Fick laws of particle diffusivity in the absence of a concentration gradient. He made a microscopic and probabilistic interpretation of the Fick laws, showing that molecules move by a random Brownian motion with a coefficient of

diffusivity (D) proportional to molecular size and temperature.

Focusing on MRI, water self-diffusivity coefficient at body temperature is: $D = 3 \times 10^{-3} \text{mm}^2/\text{s}$. In terms of MRI signal, protons Brownian motion lead to a signal loss, since proton fluctuations in presence of local fields variations caused phase changing and thus spin dephasing.

In 1956, Henry C. Torrey as first integrated the self-diffusivity contribution in the Bloch equation (Eq. 1.6) for proton spin relaxation. Thus, an expanded Bloch-Torrey equation for spin magnetisation relaxation was introduced:

$$\frac{d\vec{M}}{dt} = \gamma(\vec{M} \times \vec{B}_0) + D\nabla^2 M \quad (1.8)$$

Afterwards, in 1965, Edward O. Stejskal and John E. Tanner proposed an MRI sequence to measure D through MRI (Stejskal & Tanner, 1965). They introduced two pulse magnetic gradient field in the spin-echo sequence, the first before the π RF pulse and the second after, with the same intensity (G) and duration (δ), separated by time interval Δ .

In this manner, if proton spin move, the phase shift introduced by the first magnetic gradient will not be canceled by the second one, causing a reduction in the echo signal intensity (Figure 1.6).

Thus, in presence of diffusion the acquired MRI signal will be modulated by an additional exponential factor with respect to Eq.1.7:

$$S = N(H)(1 - e^{-TR/T_1})e^{-TE/T_2^*}e^{-bD} \quad (1.9)$$

where D is the coefficient of water diffusivity and b is a factor resulting by the integration of the applied magnetic field in time:

$$b = \gamma^2 \int_0^{TE} \left(\int_0^t G(t') dt' \right)^2 dt = \gamma^2 G^2 \delta^2 \left(\Delta - \frac{\delta}{3} \right) \quad (1.10)$$

In biological tissues, diffusivity is often restricted by microstructural barriers that hinder molecule random walk. Thus, diffusivity will not be isotropic in space, without a preferential direction, but restricted and/or directed in a specific direction, showing then an anisotropic diffusivity profile. This is the case of diffusivity within axons, in which water molecule diffusion follows the direction of the axon fibrillar structure in a preferential direction, parallel to white matter fibre trajectories.

Carlo Pierpaoli at the second meeting of the *Society of Magnetic Resonance*, San Francisco 1994 (Pierpaoli et al., 1994), proposed as first anisotropy indexes of brain white matter, basing on DTI model proposed by Basser et al. (1994) (Pierpaoli & Basser, 1996). In Figure 1.7 a schematic representation of an ellipsoidal diffusion profile with reported eigenvalues: λ_1 , λ_2 and λ_3 , and in Figure 1.8 the first proposed anisotropy index ("volume ratio").

Nowadays, diffusion measures are commonly used for clinical evaluations, and some of the most used diffusion tensor metrics are (Johansen-Berg & Behrens, 2013):

- the Fractional Anisotropy (FA), evaluated as:

$$FA = \sqrt{\frac{3}{2} \frac{(\lambda_1 - \langle \lambda \rangle)^2 + (\lambda_2 - \langle \lambda \rangle)^2 + (\lambda_3 - \langle \lambda \rangle)^2}{\lambda_1^2 + \lambda_2^2 + \lambda_3^2}} \quad (1.11)$$

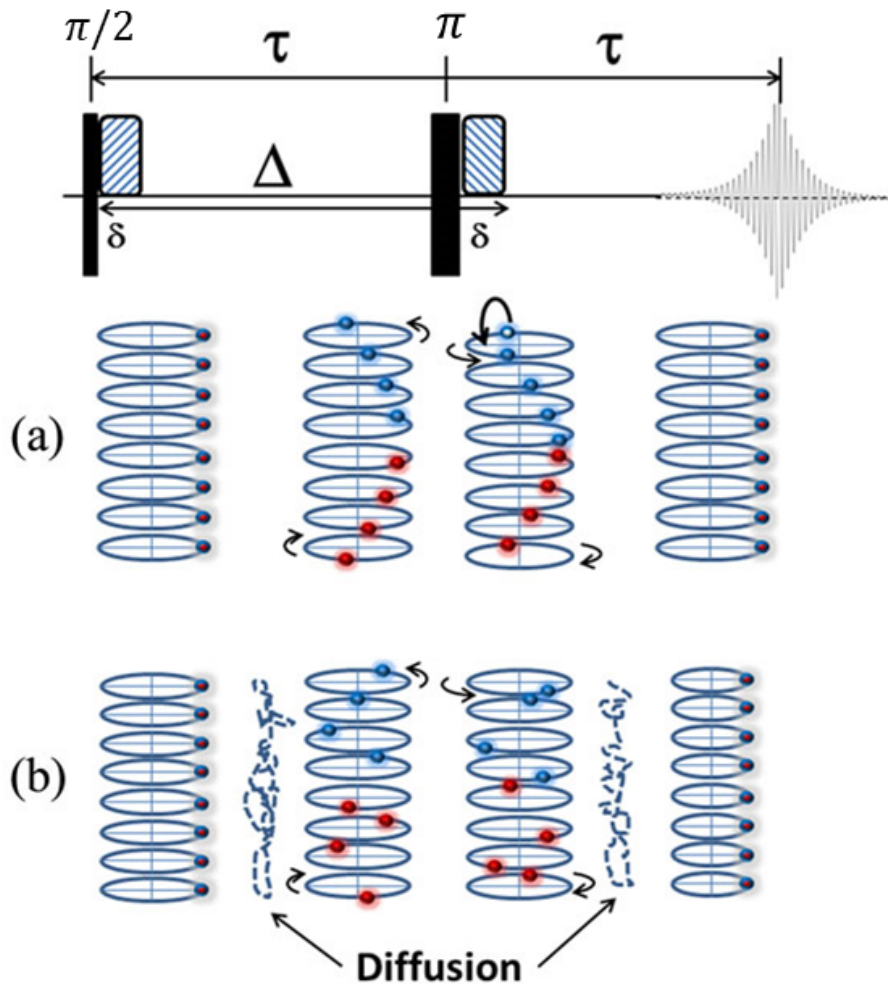


Figure 1.6: Stejskal and Tanner sequence for measuring the diffusion coefficient in MRI.

Figure modified from Heisel et al. (2012). **On the top:** the RF pulse sequence, a first $\frac{\pi}{2}$ pulse is applied, followed by a second π pulse after a time interval τ . At $TE = 2\tau$ the echo signal is acquired. δ is the duration of the diffusion magnetic gradient applied and Δ is the time separating the two gradients. **Panel A:** in the first column all the spins are pushed in the plane orthogonal to the static magnetic field by the $\frac{\pi}{2}$ pulse, in the second column spin start to dephase, in the third column after the application of the π pulse spin precession direction is inverted, and in the fourth column all the spins are in phase producing the echo. **Panel B:** the same scheme of panel A is illustrated but in presence of spin diffusivity, in this case spins do not see the same magnetic gradient strength, causing a signal attenuation showed in the fourth column.

where $\langle \lambda \rangle$ is the eigenvalue average.

- Mean Diffusivity (MD), evaluated as:

$$MD = \frac{\lambda_1 + \lambda_2 + \lambda_3}{3} \quad (1.12)$$

- Radial Diffusivity (RD), evaluated as:

$$RD = \frac{\lambda_2 + \lambda_3}{3} \quad (1.13)$$

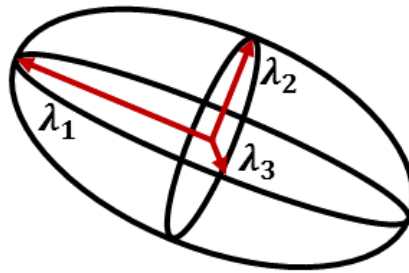


Figure 1.7: Schematics for the diffusion ellipsoid eigenvalues.

Schematic representation of an ellipsoid anisotropic diffusion profile, where eigenvalues (λ_1 , λ_2 and λ_3) are reported next to the principal axes (red).

1.4.4 Arterial spin labeling and cerebral blood flow quantification

Perfusion in the brain can be non invasively evaluated using ASL. This technique does not require contrast agent injection, but uses the blood itself as tracer. In particular the arterial flow, passing through the neck, is labelled before reaching tissues and perfusion images are obtained as a subtraction of label and control images (Chappell et al., 2018). Different labelling techniques are possible: pulsed,

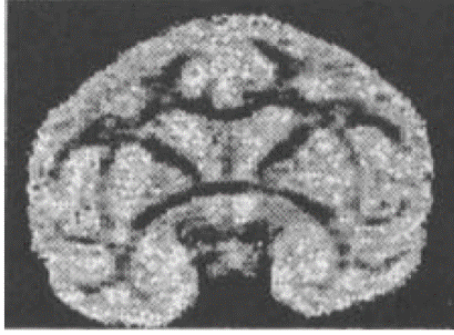


Figure 1.8: First diffusion anisotropy index for brain white matter.

Image from Pierpaoli et al. (1994). A coronal section of a monkey brain for which the volume ratio anisotropy index, defined as $Vol - ratio = 27 \frac{\lambda_1 \lambda_2 \lambda_3}{(\lambda_1 + \lambda_2 + \lambda_3)}$, was evaluated.

continuous and pseudo-continuous (Alsop et al., 2015) (Figure 1.9 A).

Perfusion, defined as the volume of blood travelling through a tissue mass over time, is tissue-dependent: GM perfusion is approximately 60mL/100g/min and WM is about 20 mL/100g/min (Huettel et al., 2004) (Figure 1.9 B).

ASL can be used as a quantitative technique to measure CBF, defined as established in the Alsop et al. (2015) white paper:

$$CBF = 6000 \frac{\lambda(S_{control} - S_{label})e^{PLD/T_1}}{2\alpha T_1 S_{PD}(1 - e^{-\tau/T_1})} \quad (1.14)$$

where S_{PD} is the magnitude of the proton-density-weighted image, PLD is the post-labelling delay, T_1 longitudinal relaxation time of arterial blood at 3T (as standard considered 1.65s), α the standard value of labelling efficacy (for a pseudo-continuous ASL sequence is 0.85), λ is the single whole brain partition coefficient (0.9 taking account density differences in water, blood and tissue); the value 6000 is for converting in the standard units ml/100g/min.

Moreover, Chen et al. (2015a) showed how ASL can be used to assess resting state

functions in the brain comparing to resting-Functional MRI (rFMRI). In fact, CBF is normally coupled to glucose, metabolism and neuronal activity, strictly related to Blood Oxygen Level Dependent (BOLD) signal (Huettel et al., 2004).

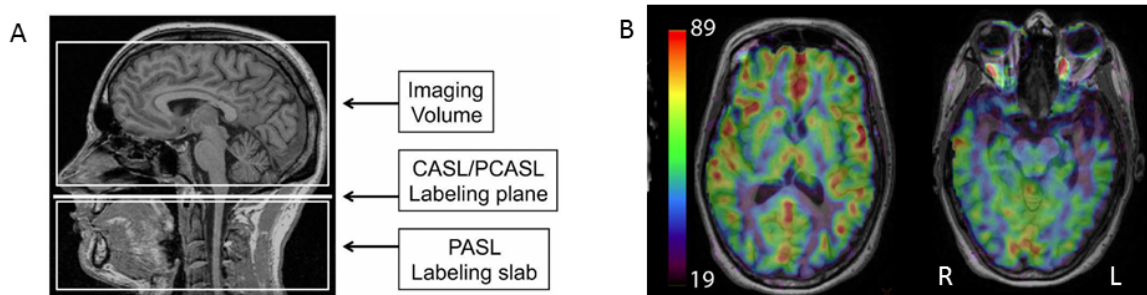


Figure 1.9: Cerebral blood flow quantification using ASL.

Images modified from Alsop et al. (2015). **Panel A:** schematic diagram of Arterial Spin Labelling (ASL) blood labelling: selecting a slab of tissue, including arterial blood, with a pulse impulse (PASL), or selecting a labelling plane using a continuous (CASL) or pseudo-continuous (PCASL) pulse. **Panel B:** Example of a Cerebral Blood Flow (CBF) map (ml/100g/min) overlay to a T1w image for a patient with semantic dementia (not low CBF in left temporal lobe).

1.5 WHITE MATTER LANGUAGE NETWORK AND TRACTOGRAPHY TECHNIQUES

In the modern literature, the predominant Broca-Wernicke-Geschwind language model (Figure 1.3) has been revised in favour of a more distributed cortical and sub-cortical system for language processing (Dick et al., 2014).

The most promising framework is the dual stream language processing: a dorsal route involving the arcuate fasciculus (Figure 1.10 A), and a ventral route composed by tracts passing through the external capsule towards the frontal lobe, and connecting the anterior temporal lobe to occipital cortex (Figure 1.10 B). In addition, new emphasis has been given to the speech "motor stream" with the investigation of the frontal aslant tract, connecting the inferior frontal lobe to pre-supplementary motor area and anterior cingulate cortex (Catani et al., 2013) (Figure 1.10 C).

Tractography methods

In 1999, the first tractography algorithms were published (Jones et al., 1999; Con-turo et al., 1999; Mori et al., 1999). It was a breakthrough in the neuroimaging field. New algorithms to visualise *in vivo* and non-invasively neuronal projections were developed (Mori et al., 1999). There was a great enthusiasm in the scientific community, looking towards the new potentiality of connectivity investigation and applications in neurological, psychiatric, and developmental disorders (Jones et al., 1999).

However, the challenge of mapping the human connectome, based on DTI, brought to a great variety of tractography algorithms, ranging from deterministic to probabilistic fibre modelling (Maier-Hein et al., 2017).

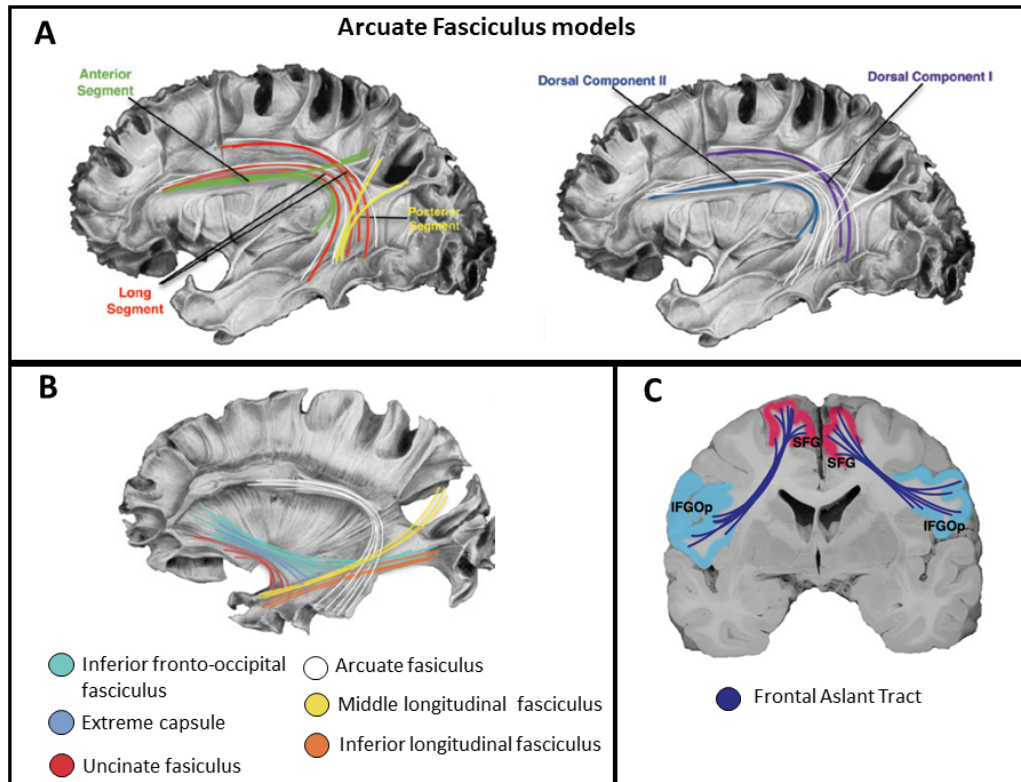


Figure 1.10: Schematics for the language network tracts.

Images modified from Dick et al. (2014). In the background, brain lateral views from dissections by Ludwig and Klingler (1956; Table 6 and 8). **Panel A:** on the left, the arcuate three segment model, composed by a long component, and the indirect anterior and posterior segments (Catani et al., 2005). On the right, the arcuate two-segment model composed by two long segment connecting the middle or superior temporal gyri (Rilling et al., 2008). **Panel B:** the ventral streams labelled with different colours, whereas the dorsal arcuate stream is represented in white. **Panel C:** bilateral connections of the frontal aslant tract in a coronal section, with outline origins in the inferior frontal gyrus pars opercularis (IFGOp) and the superior frontal gyrus (SFG).

The different approaches to fibre reconstruction can be classified in single or multiple fibre modelling at voxel level (Figure 1.11). As first, tractography algorithms based on diffusion tensor modelling provided information of a dominant single fibre orientation, used to integrate connectivity pathway trajectories. Subsequently, the mapping of complex WM configurations, such as crossing fibres, has been addressed (Tuch et al., 2002), and new high-order multiple fibre algorithm proposed (Anderson, 2005).

Behrens et al. (2003) proposed the *"ball and sticks model"*, where the isotropic diffusion background (ball) is separated from the anisotropic tensors (sticks) evaluating partial volume effects. Subsequently, different fibre orientations are estimated by Bayesian interference (Figure 1.12). Using a Monte Carlo chain modelling the uncertainty of diffusion parameters can be estimated. A probabilistic streamline propagation is performed by random sampling of the possible angular fibre orientations. This approach has been shown to offer a significant advantage in non-dominant fibre tracking (Behrens et al., 2007).

Diffusion modelling can be performed also using spherical deconvolution, which allows a direct estimation of fibre orientation distribution (Tournier et al., 2004). First a single-fibre response function has to be estimated, one method is making the assumption that in voxels with higher FA, there is only one dominant fibre orientation. The response function is needed as kernel to deconvolve the diffusion signal in the different fibre orientations (Tournier et al., 2004).

In the spherical deconvolution framework different implementations are possible, Tournier et al. (2007) proposed the constrained spherical deconvolution, in which non-negativity constraints are imposed, whereas Dell'Acqua et al. (2007) proposed the Richardson-Lucy spherical deconvolution. This algorithm was first proposed

to restore astronomical images (White, 1994), and it has been modified by Flavio Dell'Acqua to take into account noise contributions in DTI data.

The tractography modelling evolution has been deeply connected to improvements in DWI acquisition protocols, offering nowadays the possibility to acquire High Angular Resolution Diffusion Imaging (HARDI). In fact, it has been shown that intravoxel white matter fiber heterogeneity could be resolved by using high b-value diffusion gradient sampling schemes (Tuch et al., 2002).

These advanced tractography methods improve fibre reconstruction, and are used in presurgical evaluation to offer potential patient's personalised treatment strategies (Castellano et al., 2017).

However, even if a "gold standard" for fibre reconstruction has not been established, *post-mortem* can be used as validation method. In Figure 1.13 left-hemisphere dissection (De Benedictis et al., 2014) showing the arcuate fasciculus three segment model proposed by (Catani et al., 2005) using tractography. In Figure 1.14 the dissection of the uncinate fasciculus (Kier et al., 2004) is shown.

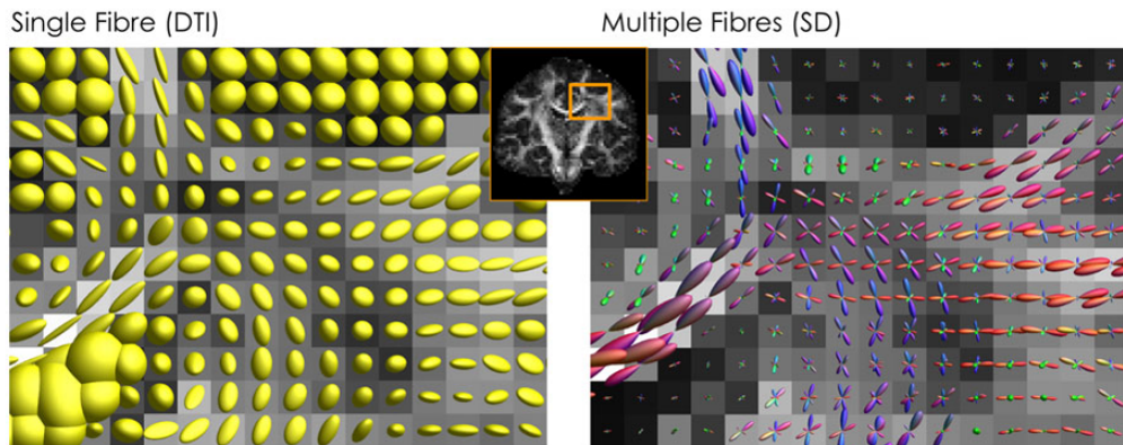


Figure 1.11: Single and multiple fibre modelling.

Image from Dell'Acqua & Tournier (2019). Different modelling of the diffusion signal are shown. **On the left:** diffusion ellipsoids obtained with diffusion tensor imaging (DTI) model, describing a single dominant fiber orientation within each voxel. **On the right:** multiple fiber evaluation within each voxel, using spherical deconvolution (SD) modelling.

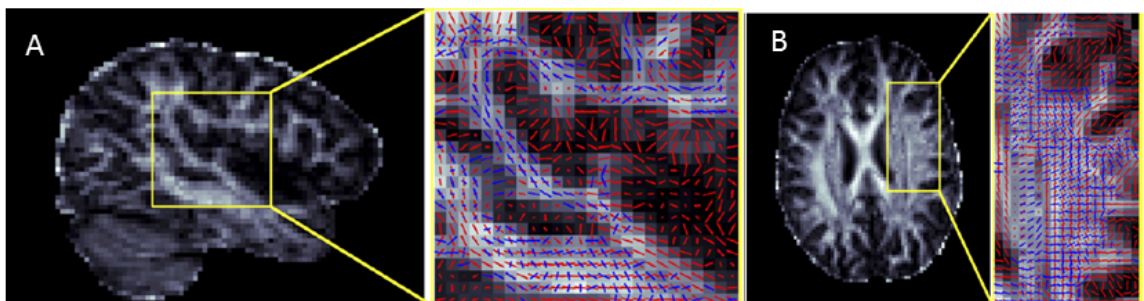


Figure 1.12: Ball and sticks multi-compartment diffusion modelling.

Image modified from Behrens et al. (2007) showing probabilistic multi-orientation fitting. Sagittal (A) and axial (B) slices with close ups of crossing fibre bundles of the arcuate fasciculus. In red first dominant fibre orientation and in blue the second.

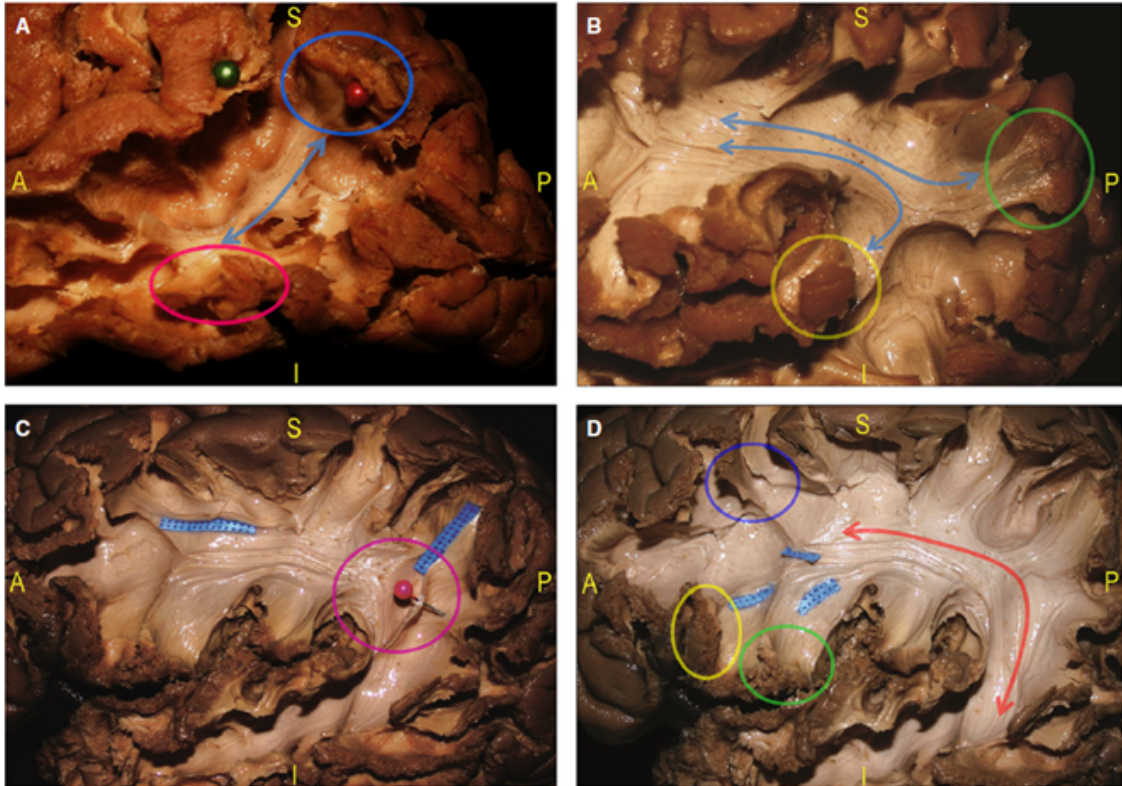


Figure 1.13: Arcuate *post-mortem* dissection.

Image from De Benedictis et al. (2014) showing the arcuate fasciculus (AF) dissection for the left hemisphere, proceeding in a lateral-medial direction. **Panel A:** starting at the tempo-parietal junction the posterior AF segment (blue arrow) was identified, connecting the posterior superior and middle temporal gyri (pink circle) with the ventral part of the inferior parietal lobe (blue circle, red pin). **Panel B:** the anterior AF group (blue arrows) connecting to the inferior frontal gyrus to the dorsal inferior parietal lobe (green circle) and to the posterior part of the superior temporal gyrus (yellow arrow). **Panel C:** the posterior AF component was lifted and separated (pink circle, pink pin) from the deeper AF fibres. **Panel D:** complete exposure of the AF long segment, connecting directly part of the superior and middle temporal gyri to the frontal lobe. AF terminations (blue tags) are directed to the pars opercularis (green circle), pars triangularis (yellow circle) and middle frontal gyrus (violet circle).

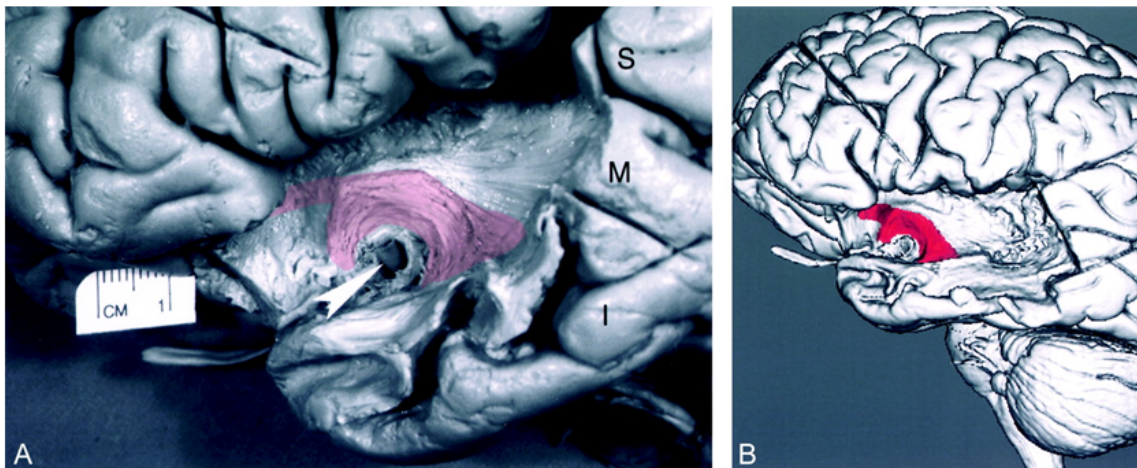


Figure 1.14: Uncinate *post-mortem* dissection.

Image from Kier et al. (2004) for the uncinate fasciculus (UF) dissection. **Panel A:** photograph of the lateral aspect of the dissected brain showing the UF (transparent red) connecting the temporal and frontal lobe. To visualise the UF it has been removed: part of the anterior segment of the superior temporal gyrus (S), portion of the middle temporal gyrus (M) and the temporal lobe. The white arrow indicates the horizontal segment of the middle cerebral artery. **Panel B:** with a three-dimensional MRI rendering the same UF lateral dissection (red) is shown.

CHAPTER 2

Cortical thickness neurodegeneration prospective

In this chapter, cortical thickness atrophy patterns in neurodegenerative pathologies were investigated. Patients were recruited by the IRCCS *Istituto delle Scienze Neurologiche di Bologna*. I had the possibility to collaborate with the clinical neuropsychologist PhD Micaela Mitolo to evaluate patient clinical assessments and discuss brain area involvement in the different neurodegeneration processes.

Preliminary results of this study has been presented at the X AIRMM Congress (Talozzi et al., 2019c), and I was awarded with the AIRMM Grant to attend the meeting.

Aim of the study was the evaluation of differences between patients with prominent language dysfunctions, PPA, patients with AD and a control group of HC. Additionally, within the PPA group, correlation of cortical thickness measures and a *category world fluency test* (Novelli et al., 1986) was evaluated.

2.1 DIFFERENTIAL ANALYSIS - PPA vs AD

Material and Methods

Participants

AD and PPA patients were recruited by the IRCCS *Istituto delle Scienze Neurologiche di Bologna*, whereas healthy controls by the Functional MR Unit - Department of Biomedical and Neuromotor Sciences, University of Bologna. PPA patients were diagnosed following the criteria of Mesulam (2003) (Table 1.1), whereas AD patients were diagnosed following the criteria published in McKhann et al. (2011), because their recruitment started before Dubois et al. (2014) criteria, then not for all AD patients PET scan or cerebral spinal fluid analysis were available.

In summary, participants of the study were (mean \pm standard deviation):

- n=18 PPA, 6M/12F, 69 ± 7 years old;
- n=18 AD, 9M/9F, 68 ± 8 years old;
- n=18 HC, 10M/8F, 65 ± 9 years old.

In addition to the root PPA diagnosis, patients were characterised in clinical variant according to specific language deficits: n=4 semantic, n=11 agrammatic, n=3 logopenic variants. Demographic features are reported in Table 2.1.

The three groups were matched with respect to age and gender.

Imaging

All participants of the study underwent a standardised T1-weighted protocol at the S.Orsola-Malpighi Hospital, Bologna; acquisition parameters are reported in Table 2.2.

Table 2.1: Demographics features of cortical thickness study participants.

PPA			AD			HC		
ID	Gender	Age (y)	ID	Gender	Age (y)	ID	Gender	Age (y)
sPPA_1	F	73	AD_1	F	62	HC_1	F	67
sPPA_2	M	69	AD_2	F	74	HC_2	M	81
sPPA_3	F	75	AD_3	F	69	HC_3	M	70
sPPA_4	F	69	AD_4	F	63	HC_4	F	58
aPPA_5	F	71	AD_5	M	64	HC_5	M	60
aPPA_6	F	52	AD_6	M	65	HC_6	M	67
aPPA_7	F	57	AD_7	M	75	HC_7	F	53
aPPA_8	M	72	AD_8	M	56	HC_8	M	59
aPPA_9	M	74	AD_9	F	77	HC_9	M	64
aPPA_10	M	76	AD_10	M	78	HC_10	F	70
aPPA_11	F	72	AD_11	M	78	HC_11	M	76
aPPA_12	M	76	AD_12	F	80	HC_12	F	73
aPPA_13	F	79	AD_13	F	65	HC_13	M	60
aPPA_14	F	72	AD_14	F	66	HC_14	F	74
aPPA_15	F	57	AD_15	M	79	HC_15	F	83
IPPA_16	F	70	AD_16	F	51	HC_16	M	52
IPPA_17	F	68	AD_17	M	65	HC_17	F	56
IPPA_18	M	63	AD_18	M	60	HC_18	M	55

F=Female; M=Male; PPA=Primary Progressive Aphasia; sPPA= semantic PPA, aPPA= agrammatic PPA, IPPA= logopenic PPA; AD=Alzheimer Disease; HC=Healthy Control.
Patients recruitment: IRCCS Istituto delle Scienze Neurologiche Bologna.
Controls recruitment: Functional MR Unit - Department of Biomedical and Neuromotor Sciences, University of Bologna.

[FreeSurfer v6](#) software was used to extract cortical thickness measures according to the Desikan-Killiany atlas (Desikan et al., 2006) in the left and right hemisphere. Thirty-three cortical regions were segmented for each hemisphere, as shown in Figure 2.1.

Table 2.2: Acquisition parameters T1w - cortical thickness study.

Static field strength =	1.5 T
Scanner model =	SIGNA HDx 15 GE
Coil =	Birdcage head coil
Sequence =	Fast Spoiled Gradient echo (FSPGR)
Time of echo =	5.1 ms
Time of relaxation =	12.5 ms
Time of inversion =	600 ms
In plane resolution =	1 x 1 mm ²
Slice thickness =	1 mm
Field of view =	25.6 x 25.6 cm ²

Acquisition of T1-weighted images was performed at S.Orsola-Malpighi Hospital, Pad. 11, Bologna (IT).

Statistical analysis

First, data normality was evaluated using the Shapiro-Wilk test, and since some of the extracted cortical thickness measures did not follow a Gaussian distribution (n=15 left and right cortical regions), the non-parametric Mann-Whitney test was used for group comparison. Moreover, p-values were corrected for false discovery rate (fdr) errors (Benjamini & Hochberg, 1995), taking into account multiple comparisons across the sixty-six cortical regions.

Subsequently, a discriminant function analysis was evaluated to differentiate PPA and AD. This is a pattern recognition algorithm that uses reduction dimensionality of multiple input variables, before applying a linear classifier to discriminate groups. Subsequently, a leave-one-out classification method was used for cross-

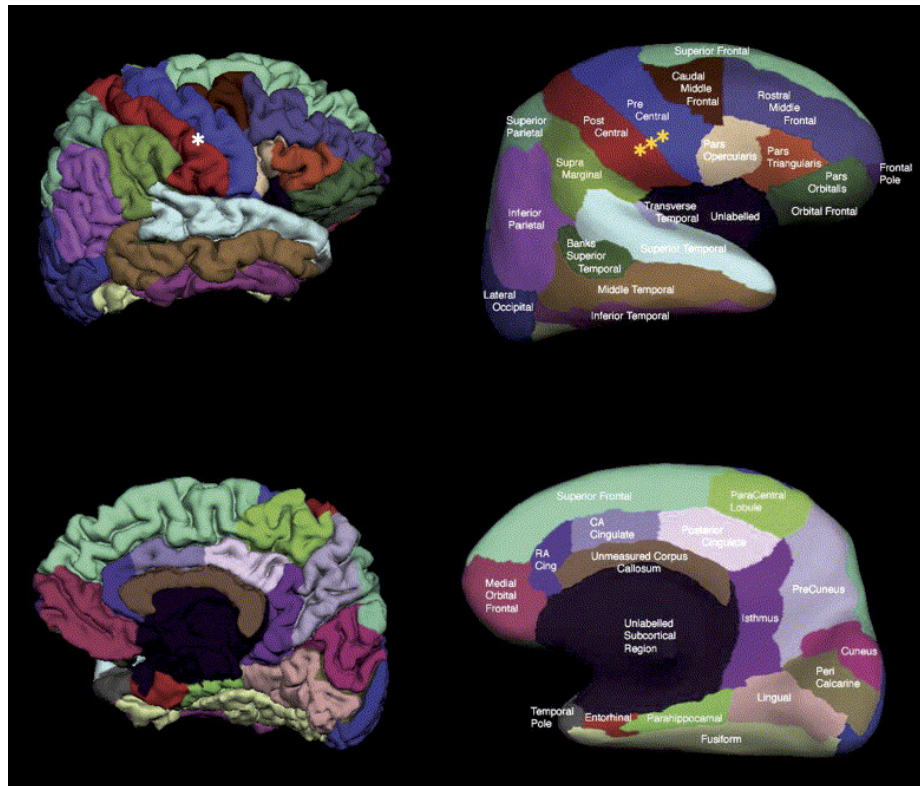


Figure 2.1: Desikan-Killiany atlas cortical parcelization.

Image from (Desikan et al., 2006). Desikan-Killiany atlas cortical parcelization implemented in the Freesurfer software.

validation, where at each iteration one of the subject is excluded from the training set to test the method accuracy, by looking if it is correctly classified in one of the two groups. Statistical analyses were performed both using [SPSS v25](#) and [Matlab R2018a](#) software.

Results - group comparisons

In Figure 2.2 surface projections of p-values corresponding to comparisons across all groups are reported. In particular, in AD patients and controls comparison, the patients' cortical thickness atrophy was widespread, involving bilateral temporal, occipital and mesial areas, whereas frontal regions were more reduced in the right hemisphere. See Table 2.3 for quantitative cortical thickness values and reported p-values.

On the contrary, comparing PPA vs controls, the patients' cortical atrophy pattern is predominantly present on the left, including temporo-parietal areas, frontal and motor cortex and portion of the dorsal cingulate. On the right, the precentral cortex is also more reduced in PPA, and with less extent also the angular, supramarginal and middle temporal gyrus, see Table 2.4 for comparison results.

Then considering the two neurodegenerative diseases, we were not able to find strong significant differences as in the comparisons with controls (p-values < 0.005 , *fdr* corrected). However, if we consider differences with a p-value < 0.05 non *fdr* corrected (Table 2.5), a consistent cortical eloquent thickness reduction is measured in PPA with respect to AD: left pars opercularis and triangularis, middle and superior temporal gyri. On the contrary, right portion of the posterior cingulate and the right later occipital cortex presented a reduced cortical thickness in AD patients.

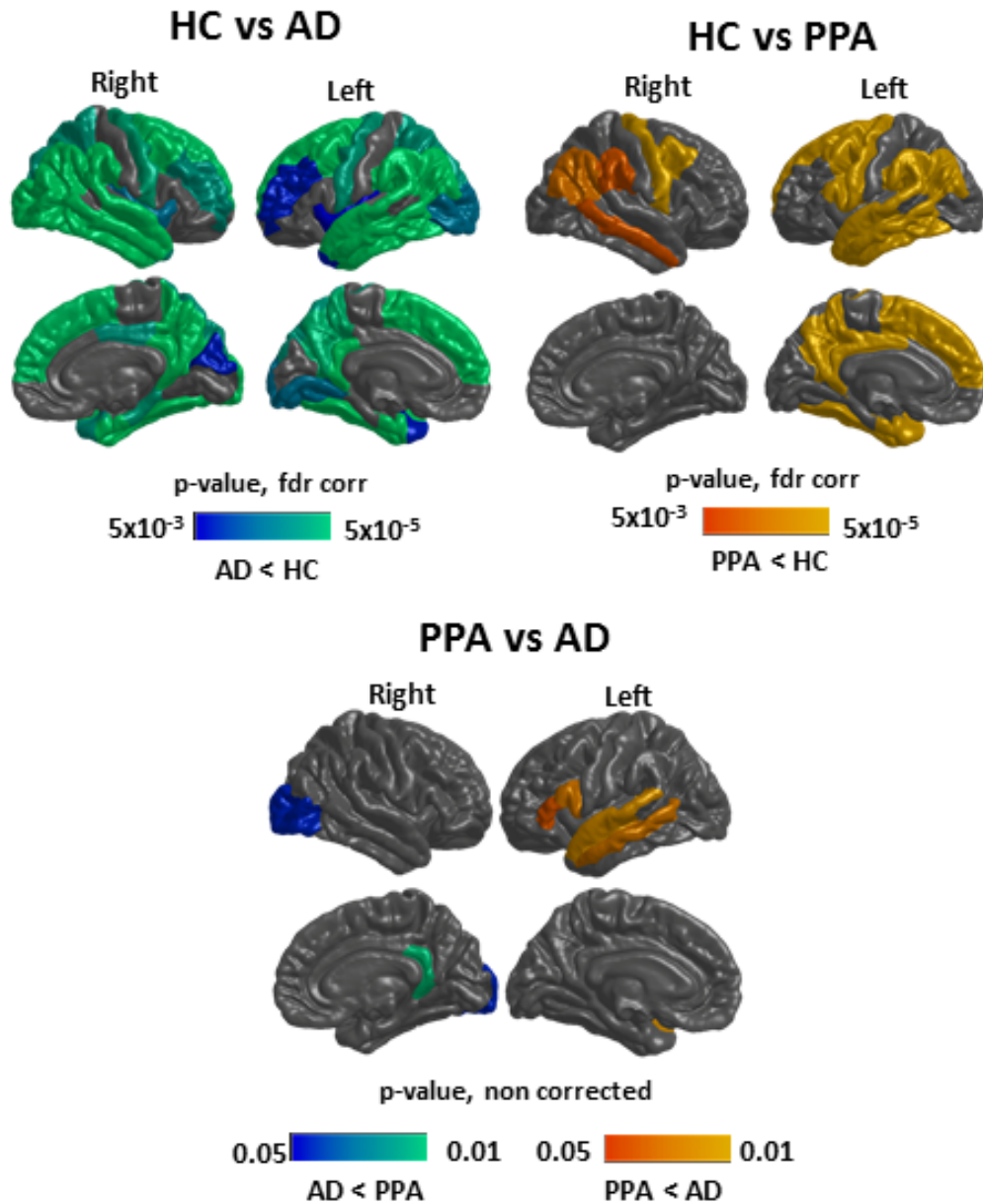


Figure 2.2: Surface projections of group comparison p-values.

P-values resulted from the Mann Whitney test are shown, projected an average brain surface using [freesurfer_statsurf_display](#) Matlab function. **Top left:** comparison of AD and controls, regions with p-values < 0.005, fdr corrected, are shown. **Top right:** comparison of PPA and controls regions with p-values < 0.005, fdr corrected, are shown. **Bottom:** comparison of PPA and AD, regions with p-values < 0.05 are shown.

HC=Healthy Controls; AD=Alzheimer's Disease; PPA=Primary Progressive Aphasia; fdr=false discovery rate.

Table 2.3: Results of the Mann-Whitney test for comparison of Healthy Controls (HC) and Alzheimer’s Disease (AD) cortical thickness (CT) values in the left and right hemisphere.

Cortical regions	p-value	HC CT (mm)	AD CT (mm)
Right caudal middle frontal gyrus	1.29E-03	2.4	2.1
Right isthmus cingulate	1.29E-03	2.2	1.8
Right pre-cuneus	1.29E-03	2.2	2
Left entorhinal cortex	1.51E-03	3.1	2.5
Left isthmus cingulate	1.51E-03	2.2	1.9
Left superior temporal gyrus	1.51E-03	2.5	2.2
Left caudal middle frontal gyrus	1.67E-03	2.4	2.2
Left inferior parietal gyrus	1.70E-03	2.3	2
Left superior frontal gyrus	1.70E-03	2.6	2.4
Right fusiform gyrus	1.70E-03	2.4	2.2
Right entorhinal cortex	1.81E-03	3.2	2.6
Right lateral occipital cortex	1.81E-03	2	1.9
Left supramarginal gyrus	1.89E-03	2.3	2.1
Left fusiform gyrus	2.06E-03	2.4	2.1
Left middle temporal gyrus	2.06E-03	2.7	2.4
Right superior temporal gyrus	2.06E-03	2.5	2.3
Right inferior parietal gyrus	2.46E-03	2.3	2
Right middle temporal gyrus	2.46E-03	2.6	2.4
Left inferior temporal gyrus	2.93E-03	2.6	2.3
Right supramarginal gyrus	3.12E-03	2.3	2.1
Right inferior temporal gyrus	3.32E-03	2.6	2.4

Cortical regions are sorted with increasing p-values, corrected for false discovery rate (only p-value < 0.005 are shown). For HC and AD, median values of CT are shown, in bold the lowest median CT across groups, which correspond to all the CT values of AD.

Table 2.4: Results of the Mann-Whitney test for comparison of Healthy Controls (HC) and Primary Progressive Aphasia (PPA) cortical thickness (CT) values in the left and right hemisphere.

Cortical regions	p-value	HC CT (mm)	PPA CT (mm)
Left caudal middle frontal gyrus	3.65E-04	2.4	2.2
Left inferior temporal gyrus	3.65E-04	2.6	2.2
Left middle temporal gyrus	3.65E-04	2.7	2.3
Left pars opercularis	3.65E-04	2.4	2.1
Left superior frontal gyrus	3.65E-04	2.6	2.3
Left superior temporal gyrus	6.89E-04	2.5	2.1
Left precuneus	7.71E-04	2.1	2
Left supramarginal gyrus	8.75E-04	2.3	2.1
Left inferior parietal gyrus	9.08E-04	2.3	2
Right caudal middle frontal gyrus	9.08E-04	2.4	2.2
Left precentral gyrus	1.55E-03	2.4	2.2
Left entorhinal cortex	3.11E-03	3.1	2.5
Left fusiform gyrus	3.11E-03	2.4	2.1
Left isthmus cingulate	3.11E-03	2.2	2
Left posterior cingulate	3.11E-03	2.3	2.2
Right precentral gyrus	3.11E-03	2.4	2.2
Left temporal pole	3.67E-03	3.5	3
Right inferior parietal gyrus	4.33E-03	2.3	2.1
Right supramarginal gyrus	4.59E-03	2.3	2.1
Right middle temporal gyrus	4.60E-03	2.6	2.4

Cortical regions are sorted with increasing p-values, corrected for false discovery rate (only p-value < 0.005 are shown). For HC and PPA median values of CT are shown, in bold the lowest median CT across groups, which correspond to all the CT values for PPA.

Table 2.5: Results of the Mann-Whitney test for comparison of Primary Progressive Aphasia (PPA) and Alzheimer’s Disease (AD) cortical thickness (CT) values in the left and right hemisphere.

Cortical regions	p-value	PPA CT (mm)	AD CT (mm)
Right isthmus cingulate	0.009	2.1	1.8
Left superior temporal gyrus	0.011	2.1	2.2
Left middle temporal gyrus	0.018	2.3	2.4
Left pars opercularis	0.019	2.1	2.3
Left pars triangularis	0.034	2.1	2.2
Right lateral occipital cortex	0.043	2	1.9

Cortical regions are sorted with increasing p-values, only p-value < 0.05 are shown. For PPA and AD median values of CT are shown, in bold the lowest median CT across groups.

Results - discriminant function analysis

Regions that significantly different in PPA and AD (Table 2.5) were considered in the discriminant function analysis. In particular, one of the requirements of this analysis is independence, thus the following variables were excluded after performing a Person’s correlation and considering the one with a lower p-value in the Mann Whitney test:

- the left middle temporal gyrus that significantly correlates with the left superior temporal gyrus $R=0.718$ (p-value= $5.3E-06$);
- left pars triangularis that significantly correlates with the left pars opercularis $R=0.621$ (p-value= $8.1E-08$);
- right lateral occipital cortex since significantly correlates with the right isthmus cortex $R=0.574$ (p-value= $2.5E-04$).

After these considerations, variables of the discriminant function were the left pars opercularis, the left superior temporal gyrus and right isthmus cortex. These vari-

ables also fulfil the Leven's criteria of equality in error variance ($p > 0.1$).

As result, one discriminant function was found that explains the 100% of variable's variance and discriminated the two groups with a p -value= $2.3E-6$ (Wilks' Lambda= 0.476). In Table 2.6 the polled within-groups correlations between the discriminant function and variables are reported. Discriminant function analysis showed different pattern of cortical reduction between the two groups: in AD patients the right isthmus cingulate was reduced, and in PPA the left superior temporal and pars opercularis.

Moreover, the leave-one out cross-validation method showed a corrected classification of 86.1% of subjects: 83.3% PPA were correctly classified and 88.9% of AD were correctly classified.

Table 2.6: Discriminant function analysis to classify PPA and AD patients.

Cortical regions	R
Right isthmus cingulate	-0.479
Left superior temporal gyrus	0.434
Left pars opercularis	0.334

Correlations between the discriminant function and variables are shown. 86.1% of subjects were correctly classified using a leave-one out classification method.

2.2 CORRELATIONS WITH *CATEGORY WORLD FLUENCY TEST* IN PPA

Material and Methods

Within the PPA patient group (Table 2.1) only patients who performed the *category world fluency test* (Novelli et al., 1986) were considered, excluding aPPA_5 and aPPA_9. Patient aPPA_19 was added in this analysis. Thus, in n=17 PPA patients, the *category world fluency test* was evaluated by asking to produce as many words as possible from selected categories (animals, fruits and car brands), subsequently, with a given 60 seconds for each category.

All patients were caucasian Italian native speakers, and raw scores were corrected for age and education according to the national normative guidelines (Table 2.7) (Novelli et al., 1986).

Patients performances in semantic fluency were correlated to cortical thickness measures, evaluated as reported in Section 2.1, using Pearson correlation coefficients.

Results

Results of Pearson correlations between cortical thickness measures and semantic fluency scores are reported in Table 2.8 and shown in Figure 2.3. In particular, the most significant correlations were found in the left hemisphere (p-value ≤ 0.01): temporal-occipital and para-limbic areas.

Table 2.7: *category world fluency test* scores (Novelli et al., 1986) and demographic features of recruited PPA patients (n=17).

ID	Semantic fluency score	Education (y)	Age (y)	Gender
sPPA_1	10	13	73	F
sPPA_2	16	18	69	M
sPPA_3	9	13	75	F
sPPA_4	22	5	69	F
aPPA_6	17	13	52	F
aPPA_7	13	12	57	F
aPPA_8	14	18	72	M
aPPA_10	22	18	76	M
aPPA_11	29	8	72	F
aPPA_12	20	5	76	M
aPPA_13	23	5	79	F
aPPA_14	15	5	72	F
aPPA_15	27	11	57	F
lPPA_16	14	12	70	F
lPPA_17	11	17	68	F
lPPA_18	32	13	63	M
aPPA_19	15	8	76	M

F=Female; M=Male; PPA=Primary Progressive Aphasia; sPPA= semantic PPA, aPPA=agrammatic PPA, lPPA= logopenic PPA.

Patients recruitment: IRCCS Istituto delle Scienze Neurologiche di Bologna.

Table 2.8: Cortical thickness and *category world fluency test* correlations.

Cortical region	R	p-value
Left inferior temporal gyrus	0.661	0.004
Left middle temporal gyrus	0.658	0.004
Left parahippocampal gyrus	0.657	0.004
Left fusiform gyrus	0.608	0.01

Significant correlations between cortical thickness measures and *category world fluency test* scores (p-value ≤ 0.01).

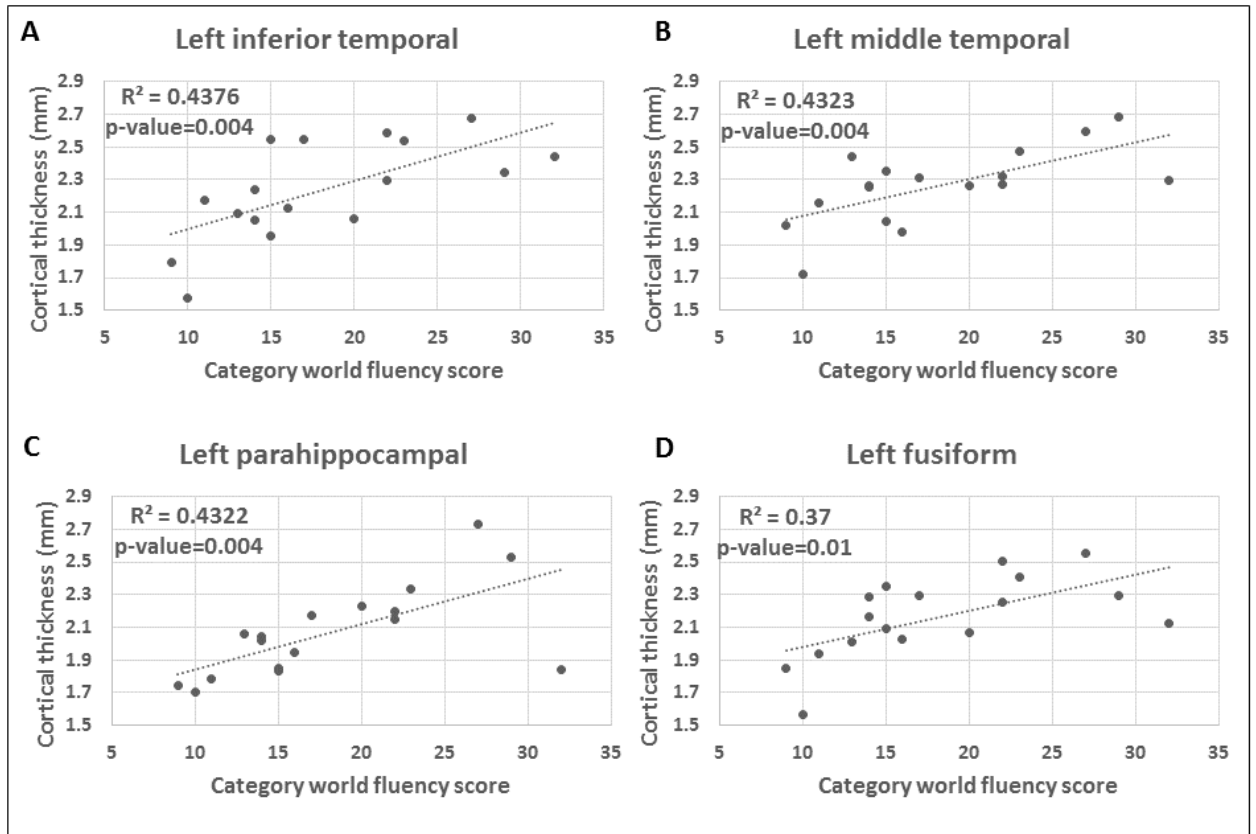


Figure 2.3: Correlation plots of *category world fluency test* scores and cortical thickness measures.

Correlation plots between cortical thickness areas and semantic fluency scores for PPA patients are reported. Dashed lines represent the linear regression fitting and R^2 the Pearson correlation coefficients. Only cortical regions with significant correlations ($p\text{-value} \leq 0.01$) are shown: left inferior temporal cortex (A), left middle temporal cortex (B), left parahippocampal cortex (C) and left fusiform cortex (D).

CHAPTER 3

Mapping white matter disconnections in Primary Progressive Aphasia

Thanks to the *Marco Polo International Research Exchange Scholarship*, I spent nine months (from 1/9/2018 to 31/05/2019) at the Neuroanatomy and Tractography Laboratory ([NatBrainLab](#)), Kings College London, under the supervision of Professor Marco Catani. I met him during the *20th Neuroanatomy and tractography Workshop*, Kings College London (26-28/2/2018), a course that I attended during my PhD training. In that occasion we discussed about a research project on PPA data acquired by Professor Marek Marsel Mesulam at the Northwestern University, Chicago (USA).

The aim of this study was the longitudinal evaluation of language and white matter integrity, in PPA and healthy controls. I evaluated DTI metrics in the language network with a ROI-based approach, comparing the two groups, both acquired with a 2-years follow-up. Moreover, correlations between language assessment scores and DTI metrics were analysed.

Participants

PPA patients and HC were recruited by the Cognitive Neurology and Alzheimer Center of Northwestern University, Feinberg School of Medicine, Chicago (USA).

In summary, the participants of this study were (mean \pm standard deviation):

- n=31 PPA, 16M/15F, 66 ± 6 years old, 3.6 ± 1.9 disease duration, 16 ± 2.6 education years, 24 ± 1.3 follow-up months;
- n=27 HC, 15M/12F, 63 ± 6 years old, 16 ± 2 education years, 25 ± 1.5 follow-up months;

Complete demographic and clinical features are reported in Table 3.1 for patients and in Table 3.2 for controls. The two groups were matched for age, gender, education and handedness, evaluated with the Edinburgh Handedness Inventory (Oldfield, 1971).

In addition to the root PPA diagnosis, patients were characterised in clinical variants according to language deficits: n=11 semantic variant, n=13 agrammatic and n=7 logopenic.

Participants underwent clinical assessments and MRI scan at the baseline and after 2-years.

Table 3.1: Demographic and clinical features of PPA patients - DTI longitudinal study.

ID	Gender	Age (y)	Disease Duration (y)	Education (y)	Handedness
sPPA_CH6	F	56	2.58	18	100
sPPA_P101	M	64	2.32	18	70
sPPA_P47	F	61	2.25	13	100
sPPA_P51	M	65	1.87	20	100
sPPA_P59	M	63	3.08	14	80
sPPA_P60	M	69	5.67	20	90
sPPA_P64	M	61	5	14	100
sPPA_P69	F	61	1.83	12	100
sPPA_P82	M	73	4.01	20	95
sPPA_P83	M	73	2.5	18	90
sPPA_P98	M	60	6.05	16	90
aPPA_P42	F	80	0.92	14	100
aPPA_P53	F	63	2.83	18	100
aPPA_P58	M	67	3.25	14	80
aPPA_P63	M	72	5	14	100
aPPA_P66	F	66	5.08	12	100
aPPA_P68	F	62	6.75	13	100
aPPA_P72	F	70	3.67	18	100
aPPA_P78	M	60	1.42	19	90
aPPA_P86	M	80	6.04	18	100
aPPA_P89	M	62	7.19	16	100
aPPA_P92	F	69	1.23	14	100
aPPA_P94	F	63	2.54	16	100
aPPA_P99	F	66	2.5	12	100
IPPA_P100	M	64	3.8	16	80
IPPA_P103	F	58	2.03	18	95
IPPA_P56	F	65	1.33	18	100
IPPA_P62	M	58	7.92	20	100
IPPA_P70	F	72	4.58	14	100
IPPA_P73	F	65	3.33	18	100
IPPA_P88	M	68	3.82	16	100

ID=Identification key used in the research study.

sPPA=semantic PPA, aPPA=agrammatic PPA, IPPA=logopenic PPA,
F=Female; M=Male.

Recruitment: Cognitive Neurology and Alzheimer Center of North-western University, Feinberg School of Medicine, Chicago (USA).

Table 3.2: Demographic features of HC - DTI longitudinal study.

ID	Gender	Age (y)	Education (y)	Handedness
HC_C12	F	50	16	100
HC_C30	F	57	16	100
HC_C38	F	58	14	100
HC_C40	F	61	18	100
HC_C5	F	61	16	80
HC_C21	F	62	13	85
HC_C15	F	63	18	100
HC_C52	F	64	12	90
HC_C23	F	66	16	80
HC_C3	F	68	16	90
HC_C1	F	69	12	100
HC_C49	F	72	16	100
HC_C24	M	55	18	100
HC_C48	M	55	16	100
HC_C39	M	56	16	100
HC_C2	M	57	18	85
HC_C29	M	60	14	95
HC_C35	M	60	14	95
HC_C45	M	61	16	100
HC_C8	M	64	18	65
HC_C4	M	67	14	100
HC_C41	M	67	14	90
HC_C17	M	69	12	85
HC_C44	M	70	19	90
HC_C27	M	71	18	100
HC_C13	M	73	16	100
HC_C37	M	73	18	100

ID=Identification key used in the research study.

F=Female; M=Male; HC=Healthy Controls.

Recruitment: Cognitive Neurology and Alzheimer Center of Northwestern University, Feinberg School of Medicine, Chicago (USA).

3.1 LANGUAGE ASSESSMENT

Language functions, in PPA and HC, were tested using the following neuro-psychological tests:

- the **Western Aphasia Battery Revised** (Kertesz, 2007) to obtain an overall language impairment score, and for sentence repetition scores;
- the **Peabody Picture Vocabulary Test IV** edition (Dunn et al., 2007) to measure impairment in word comprehension;
- the **Boston Naming Test** (Goodglass et al., 1983; Kaplan et al., 2001) to assess naming performance;
- the **Pyramids and Palm Trees Test** (Howard & Patterson, 1992) to assess object knowledge;
- the **Northwestern Anagram Verbs and Sentence** (Cho-Reyes & Thompson, 2012) as a measure of impairment in sentence comprehension.

Western Aphasia Battery Revised - AQ

To obtain an overall score of language impairment the revised Western Aphasia Battery (WAB-R) was used (Kertesz, 2007), and particularly the Aphasia Quotient (AQ) score. The AQ ranges between 0-100, and scores above 93.8 are considered normal for language functions (Pedersen et al., 2004). In the WAB-R several language abilities were considered. The AQ is a score composed by four categories (total of 32 sub-tests):

- spontaneous speech score - evaluating information content, fluency, grammatical competence and paraphrases;

- auditory verbal comprehension score - considering yes/no questions, auditory word recognition and sequential commands;
- repetition score;
- naming and word finding - object naming, word fluency, sentence comprehension and responsive speech.

Western Aphasia Battery Revised - Rep66

From the WAB-R, test sentence repetition was considered. In particular, the WAB-R repetition scale contains 100 items with ascending difficulties from repetition of a single word to strings, phrases, and sentences. In Rep66 we considered only 66 items related to sentence repetition.

Peabody Picture Vocabulary Test - PPVT

The Peabody Picture Vocabulary Test (PPVT), IV edition (Dunn et al., 2007), is designed to measure vocabulary performance. It contains a total of 228 items, and a subset of 36 moderately difficult items (157 – 192) was considered. A choice of four pictures was shown and ask participants to match an auditory word representing an object, action or attribute to one of the pictures (Figure 3.1).

Boston Naming Test - BNT

The Boston Naming Test (BNT) was used as a measure of impairment in naming (Kaplan et al., 2001). In particular, 60 items were administered in order of decreasing frequency of occurrence in language, and asked to name them within 20 seconds. If patients are not able to name the picture, a semantic clue is given, and

if this is not determinant, after 20 second a second phonemic clue is given (Figure 3.2).

Pyramids and Palm Trees Test - PPT

The Pyramids and Palm Trees Test (PPT) was used to investigate non-verbal object knowledge using the test picture version containing 52 items (Howard & Patterson, 1992). Three pictures were presented and it was asked to choose which of the two pictures in the bottom was conceptually more closely associated with the target object on the top (Figure 3.3).

Northwestern Anagram Verbs and Sentence - NAVS SCT

The Northwestern Anagram Verbs and Sentence, sentence comprehension part (NAVS SCT) was used to assess grammatical competence and to measure impairment in sentence comprehension (Cho-Reyes & Thompson, 2012). In particular, 15 items were considered: long items (n=10) and short (n=5). During the test, the target sentence is read aloud and it is asked to point items corresponding to the listened sentence. 10 seconds were given to participants to respond. Sentences were repeated once on request (Figure 3.4).

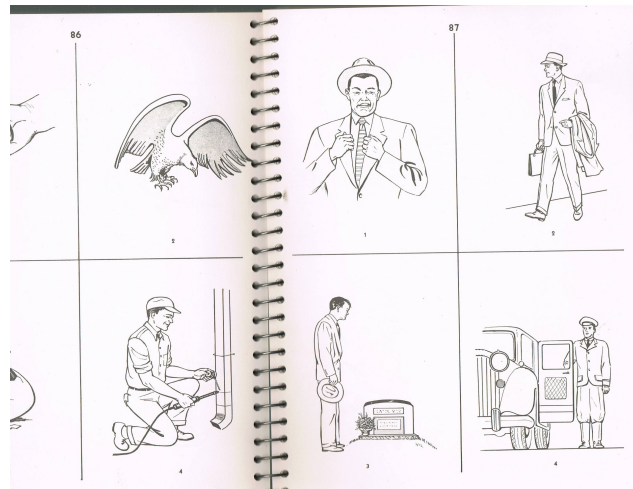


Figure 3.1: Peabody Picture Vocabulary Test items.

Example of a four picture choice used in the Peabody Picture Vocabulary Test, where it is asked to match an auditory word representing an object, action or attribute to one of the pictures.



Figure 3.2: Boston Naming Test items.

Example of five items used in the Boston Naming Test, where it is asked to name items with a different occurrence in language.

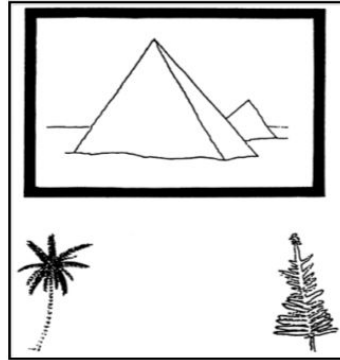


Figure 3.3: Pyramids and Palm Trees Test items.

Example of one item used in the Pyramids and Palm Trees Test, where it is asked to match one of the two pictures in the bottom to the picture on the top, choosing the one that is conceptually close to the target image.

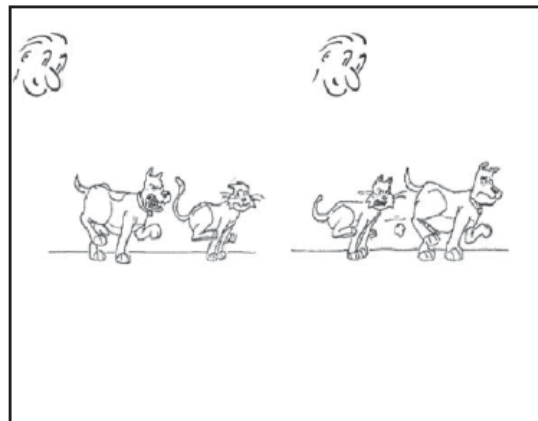


Figure 3.4: Northwestern Anagram Verbs and Sentence items.

Example of sentence comprehension item of the Northwestern Anagram Verbs and Sentence. The examiner reads aloud the sentence: «Pete saw the cat who was chasing the dog» and it is asked to point the figure that matches the listened sentence.

3.2 EVALUATION OF DTI METRICS IN THE LANGUAGE NETWORK

DWI protocol acquisition

PPA patients and HC underwent a standardised MRI protocol at the Cognitive Neurology and Alzheimer Center of Northwestern University, Feinberg School of Medicine, Chicago (USA).

In this study, I evaluated DWI data longitudinally acquired, whose acquisition parameters were reported in Table 3.3, and remained constant in the 2-years follow-up.

Table 3.3: Acquisition parameters DTI - baseline and 2-years follow-up.

Scanner model =	Siemens TRioTim
Static field strength =	3T
Coil =	12 channels
b-value =	1000 s/mm^2
Time of echo =	88 ms
Time of relaxation =	16 R-R intervals
Voxel dimension =	2x2x2 mm^3
Acquisition matrix =	128x128x72
n. of diffusion gradient directions =	60
n. of null b-value =	8

The acquisition was gated to the cardiac cycle, thus the time of relaxation is a function of the subject's heart rate variability (R-R).

Site: Cognitive Neurology and Alzheimer Center of Northwestern University, Feinberg School of Medicine, Chicago (USA).

DWI pre-processing

Imaging pre-processing was performed in collaboration with Ahmad Beyh, PhD candidate of the Natbrainlab group, King's College London.

We used the method described by Veraart et al. (2016) for de-noising and the one described by Kellner et al. (2016) for Gibbs ringing correction, for both methods we used the [Tortoise](#) software C implementation (Pierpaoli et al., 2010).

Atlas-approach for language tracts

To evaluate DTI metrics in both PPA patients and HC, a tract atlas-based approach was used, in particular, group variability maps were evaluated with the MegaTrack software (Dell'Acqua et al., 2015), which concatenates in a single group tractogram tractography results obtained from different subjects using the [StarTrack](#) software. Tract group-variability maps were downloaded from the website recently created by Stones et al. (2019). This website allows to set a query for control subjects controlling for age and gender, and obtain group-variability maps of different WM tracts in the MNI-152 space. For this analysis, a deterministic tensor model was used and only control subjects older than 40 years old were considered. Thus, we obtained a control group of 49 healthy volunteers, ageing between 58 ± 11 years old, 22 females and 27 males. Tract group variability maps were thresholded to contain at least the 50 % of controls.

In particular, I evaluated WM tracts of the left hemisphere involved in language processing (Catani & de Schotten, 2012; Forkel & Catani, 2019):

- the arcuate fasciculus (AF), long segment, anterior and posterior indirect segments (Catani et al., 2005);
- the uncinate fasciculus (UF) (Catani et al., 2002);
- aslant tract (FAT) (Catani et al., 2012, 2013);
- inferior longitudinal fasciculus (ILF) (Catani & Dawson, 2017).

A 3D representation of tract group-variability maps is shown in figure (3.5).

MNI-152 registration

The obtained group variability maps for language tracts were used as ROIs to evaluate DTI metrics (FA, MD and RD), in PPA patients and controls. For this purpose, ROIs were registered from the MNI-152 space to subject's DWI native space, using the [Ants software](#).

This method applies a diffeomorphic transformation between two different image spaces to a third common space where coordinates of input images are transformed. For this purpose, Ants software calculated optimal translation matrices and vector field by linear and non-linear registration algorithms.

In particular, for ROIs registration I used an FA-based approach, in which subject's FA maps were registered to an FA template in the MNI space, which has been created using the HCP dataset (Human Connectome Project S900) reported in Chapter 6.

3.3 PPA vs HEALTHY CONTROLS - LANGUAGE ASSESSMENT AND DTI METRICS

Statistical methods

All the statistical tests were performed at t_0 , t_{0+2y} and evaluating the longitudinal variation rate Δ , defined as:

- t_0 - DTI metrics and language score at the baseline;
- t_{0+2y} - DTI metrics and language score at the 2-years follow-up;

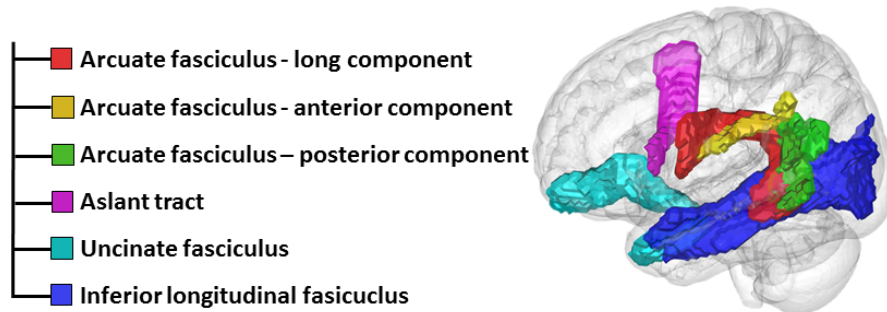


Figure 3.5: White matter atlas for language network evaluation.

Associative WM tracts involved in language processing are shown for the left hemisphere. Tract group variability maps for control volunteers from the database in Stones et al. (2019) website, using Megatrack software (Dell’Acqua et al., 2015), and thresholded to include at least the 50% of controls. 3D rendering was obtained with ([Brain-R software](#)).

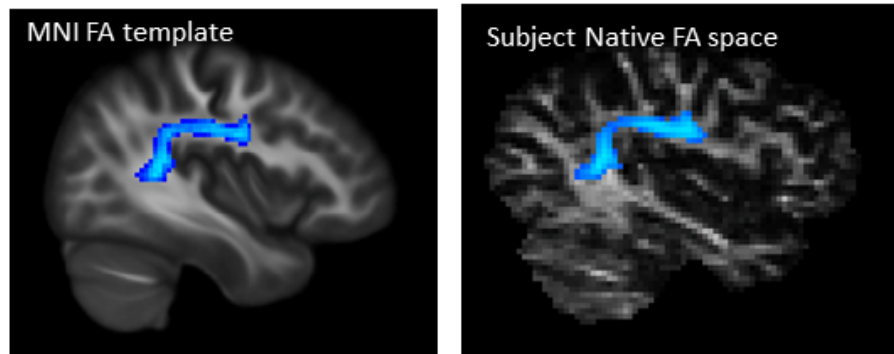


Figure 3.6: FA-based registration of language tracts.

In blue the group variability map of the Arcuate Fasciculus (AF), long component, thresholded to include at least the 50% of controls. On the left the MNI-152 FA map where the AF is defined in the MegaTrack atlas, on the right a PPA patient FA map and the registered AF using the ANTs software.

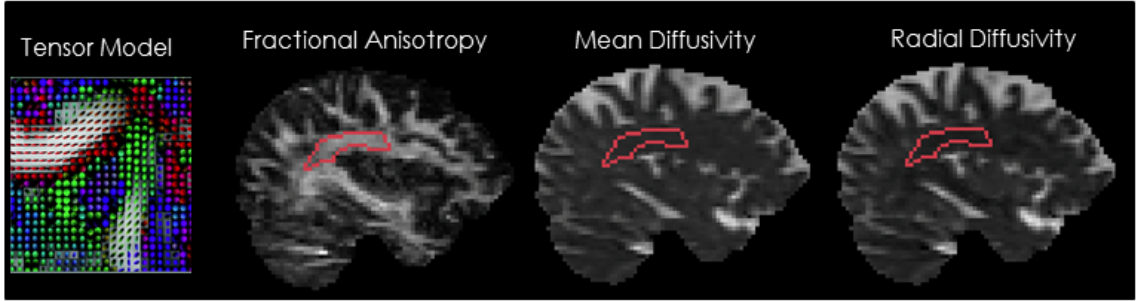


Figure 3.7: Arcuate ROI to evaluate DTI measures.

On the left a tensor model RGB zoomed representation. On the middle and right, the arcuate ROI borders (red) on sagittal projections of different DTI measures evaluated in a PPA patients: fractional anisotropy, mean and radial diffusivity.

- Δ - variation rate between baseline (t_0) and follow-up (t_{0+2y}), where the variation rate formula (Rogalski et al., 2007) was:

for language assessment

$$\Delta \text{ score} = \frac{(\text{score at } t_0) - (\text{score at } t_{0+2y})}{(\text{score at } t_0)} \quad (3.1)$$

and for DTI measures

$$\Delta \text{ DTI measure} = \frac{(\text{DTI measure at } t_0) - (\text{DTI measure at } t_{0+2y})}{(\text{DTI measure at } t_0)} \quad (3.2)$$

In this manner, the longitudinal variation measures has been normalised by the baseline value.

As described in Paragraph 2.1, comparisons between patients and controls were evaluated with the non-parametric Mann-Whitney test, and p-values corrected taking into account for multiple comparisons across different ROIs and DTI met-

rics (Benjamini & Hochberg, 1995) ([Matlab R2018a](#)).

Subsequently, to evaluate differences across the three PPA variants the non parametric Kruskal-Wallis Test was used, and p-values corrected for multiple comparisons across groups, using Bonferroni ([SPSS v25](#)).

Results

Language assessment

Language assessment mean scores and significant differences between PPA variants and controls were reported in Table 3.4.

WAB repetition scores were lower in aPPA and lPPA, whereas PPVT and BNT scores were lower in sPPA. The PPT scores were mostly lower in sPPA at the baseline, whereas at the follow-up significantly lower in all the PPA variants with respect to controls. In addition, the NAVS longitudinal progression rate Δ was significantly higher for score reduction only in aPPA.

For more details, about language assessment scores in PPA clinical variants, in Appendix A results of Kruskal-Wallis comparisons across PPA variants were reported and also box-plot of *post-hoc* significant differences between sPPA vs aPPA and sPPA vs lPPA.

DTI metrics

At the baseline, significant differences between PPA patients and healthy controls were found (Table 3.5). Considering p-value < 0.01 and clinical PPA variants:

- in the FAT, higher FA measure in sPPA;
- in the ILF, higher MD measure in sPPA;

Language test	HC	sPPA	aPPA	lPPA
WAB AQ (100) t_0	100	88***	87***	91**
WAB AQ (100) $t_0 + 2y$	-	70	63	73
Δ WAB AQ	-	-0.2	-0.28	-0.2
WAB Rep (66) t_0	65	59***	51***	49***
WAB Rep (66) $t_0 + 2y$	65	49***	31***	32***
Δ WAB Rep	0	-0.17***	-0.41***	-0.34**
PPVT (36) t_0	35	22***	34*	34*
PPVT (36) $t_0 + 2y$	35	13***	31***	30**
Δ PPVT	0.01	-0.38**	-0.09*	-0.11*
BNT (60) t_0	58	10***	46***	53**
BNT (60) $t_0 + 2y$	58	5***	33***	33***
Δ BNT	0	-0.48***	-0.35**	-0.39***
PPT Pic (52) t_0	51	45***	50**	50
PPT Pic (52) $t_0 + 2y$	51	38***	48***	46***
Δ PPT Pic	0	-0.17***	-0.03**	-0.08***
NAVS-SCTnc (15) t_0	15	15	14**	14*
NAVS-SCTnc (15) $t_0 + 2y$	15	14*	10**	14*
Δ NAVS-SCTnc	0	-0.07	-0.26*	-0.05

Table 3.4: PPA vs HC, language assessment score comparison.

Mean language assessment scores for controls and PPA variants (sPPA, aPPA and lPPA) are reported, at the baseline t_0 , at 2-years follow-up $t_0 + 2y$ and evaluating the longitudinal variation rate Δ (Equation 3.1). Significant results for Mann-Whitney test comparison between PPA and controls are signed with asterisks corresponding to p-values: * < 0.05, ** < 0.01, *** < 0.001.

At the follow-up, a greater DTI measure difference between patients and controls was detected (Table 3.6). Considering p -value < 0.001 and clinical PPA variants:

- in the AF posterior segment and UF, the FA was lower, and MD and RD measures higher in all PPA variants;
- in the ILF, the MD measure higher in all PPA variants.

Moreover, evaluating the Δ longitudinal variation rate of DTI measures (Equation 3.2), significant differences between PPA and controls were found in all the investigated language networks (Table 3.7). Considering p -value < 0.001 and clinical PPA variants:

- in the the AF long segment, the FA measure was decreased in sPPA and aPPA, and the RD measure increased in sPPA;
- in the AF anterior segment, the FA measure was decreased in lPPA;
- in the AF posterior, the MD measure increased in sPPA, the FA measure was reduced and the RD measure decreased in all PPA variants;
- in the UF, MD and RD measures increased in sPPA, and FA measure was decreased in all PPA variants.

Additionally, in Appendix A results of Kruskal-Wallis comparisons of DTI metrics across PPA variants were reported, and also box-plot of post-hoc significantly differences between sPPA vs aPPA and sPPA vs lPPA.

DTI metrics t_0					
	HC	all PPA	sPPA	aPPA	lPPA
AF FA	0.44	0.44	0.45	0.44	0.44
AF MD ($mm^2/s \times 10^{-3}$)	0.74	0.75	0.74	0.77*	0.75
AF RD ($mm^2/s \times 10^{-3}$)	0.56	0.56	0.54	0.58	0.56
AF ant FA	0.4	0.39	0.4	0.37	0.39
AF ant MD ($mm^2/s \times 10^{-3}$)	0.76	0.76	0.74	0.81*	0.75
AF ant RD ($mm^2/s \times 10^{-3}$)	0.59	0.6	0.57	0.65	0.59
AF post FA	0.34	0.32	0.33	0.32	0.3*
AF post MD ($mm^2/s \times 10^{-3}$)	0.77	0.79**	0.78	0.82*	0.81*
AF post RD ($mm^2/s \times 10^{-3}$)	0.62	0.66*	0.63	0.67*	0.67
UF FA	0.34	0.33	0.3*	0.34	0.34
UF MD ($mm^2/s \times 10^{-3}$)	0.8	0.81	0.83*	0.8	0.79
UF RD ($mm^2/s \times 10^{-3}$)	0.64	0.65	0.68*	0.64	0.65
FAT FA	0.41	0.43	0.44**	0.38	0.44*
FAT MD ($mm^2/s \times 10^{-3}$)	0.74	0.75	0.73	0.77*	0.73
FAT RD ($mm^2/s \times 10^{-3}$)	0.57	0.57	0.54	0.61	0.54
ILF FA	0.39	0.39	0.38	0.39	0.4
ILF MD ($mm^2/s \times 10^{-3}$)	0.8	0.82*	0.85**	0.83	0.81
ILF RD ($mm^2/s \times 10^{-3}$)	0.61	0.62	0.66	0.65	0.62

Table 3.5: PPA vs HC, DTI measures at baseline.

Median DTI measures (FA, MD and RD), evaluated in language tracts at baseline t_0 , are reported for controls, PPA group and PPA variant sub-groups (sPPA, aPPA and lPPA). Significant results for Mann-Whitney test comparison between patients and controls are signed with asterisks corresponding to p-values: * < 0.05, ** < 0.01, *** < 0.001.

	DTI metrics $t_0 + 2y$				
	HC	all PPA	sPPA	aPPA	lPPA
AF FA	0.45	0.42**	0.42**	0.42**	0.41**
AF MD ($mm^2/s \times 10^{-3}$)	0.73	0.77**	0.76**	0.79**	0.77**
AF RD ($mm^2/s \times 10^{-3}$)	0.54	0.58*	0.57*	0.6*	0.58*
AF ant FA	0.4	0.37**	0.39**	0.37**	0.36**
AF ant MD ($mm^2/s \times 10^{-3}$)	0.76	0.78*	0.77*	0.81*	0.78*
AF ant RD ($mm^2/s \times 10^{-3}$)	0.59	0.62*	0.61*	0.64*	0.62*
AF post FA	0.35	0.29***	0.31***	0.29***	0.27***
AF post MD ($mm^2/s \times 10^{-3}$)	0.76	0.83***	0.81***	0.83***	0.86***
AF post RD ($mm^2/s \times 10^{-3}$)	0.62	0.69***	0.66***	0.69***	0.72***
UF FA	0.34	0.31***	0.28***	0.32***	0.33***
UF MD ($mm^2/s \times 10^{-3}$)	0.79	0.83***	0.9***	0.83***	0.83***
UF RD ($mm^2/s \times 10^{-3}$)	0.64	0.69***	0.74***	0.68***	0.67***
FAT FA	0.41	0.42	0.43	0.36	0.43
FAT MD ($mm^2/s \times 10^{-3}$)	0.75	0.77	0.74	0.82	0.75
FAT RD ($mm^2/s \times 10^{-3}$)	0.57	0.58	0.55	0.66	0.56
ILF FA	0.39	0.37	0.36	0.36	0.38
ILF MD ($mm^2/s \times 10^{-3}$)	0.8	0.85***	0.85***	0.84***	0.84***
ILF RD ($mm^2/s \times 10^{-3}$)	0.62	0.65	0.65	0.66	0.65

Table 3.6: PPA vs HC, DTI measures at follow-up.

Median DTI measures (FA, MD and RD), evaluated in language tracts at 2-years follow-up t_{0+2y} , are reported for controls, PPA group and PPA variant sub-groups (sPPA, aPPA and lPPA). Significant results for Mann-Whitney test comparison between patients and controls are signed with asterisks corresponding to p-values: * < 0.05, ** < 0.01, *** < 0.001.

	DTI metrics Δ				
	HC	all PPA	sPPA	aPPA	IPPA
AF FA	0.02	-0.04***	-0.05***	-0.03***	-0.05**
AF MD	0	0.02**	0.03**	0.02*	0.03*
AF RD	-0.01	0.03***	0.03***	0.03**	0.05**
AF ant FA	0.02	-0.04***	-0.05	-0.03*	-0.06***
AF ant MD	0	0.01	0.03	0.01	0.02
AF ant RD	-0.02	0.02**	0.04**	0.02	0.02*
AF post FA	0.01	-0.08***	-0.08***	-0.08***	-0.11***
AF post MD	0	0.04***	0.04***	0.02**	0.05**
AF post RD	0	0.05***	0.05***	0.03***	0.07***
UF FA	0.03	-0.07***	-0.1***	-0.07***	-0.04***
UF MD	0	0.04***	0.05***	0.02**	0.02*
UF RD	-0.02	0.05***	0.07***	0.04**	0.03*
FAT FA	0.02	-0.02**	-0.02**	-0.02	-0.04**
FAT MD	0.01	0.03**	0.01	0.03	0.04**
FAT RD	0	0.04***	0	0.05**	0.06**
ILF FA	0.02	-0.06**	-0.05*	-0.06**	-0.06
ILF MD	0	0.03***	0.05**	0.02*	0.04**
ILF RD	0	0.06***	0.08*	0.03**	0.06*

Table 3.7: PPA vs HC, DTI measures at longitudinal variation rate.

Median DTI measures (FA, MD and RD) of the longitudinal variation rate, Δ (Equation 3.2) is reported for controls, PPA group and PPA variant sub-groups (sPPA, aPPA and IPPA). Significant results for Mann-Whitney test comparison between patients and controls are signed with asterisks corresponding to p-values: * < 0.05, ** < 0.01, *** < 0.001.

3.4 MAPPING LANGUAGE DISCONNECTIONS

Statistical methods

Language disconnection mapping in the language network was evaluated in PPA patients, calculating correlations between DTI measures and language assessment at baseline t_0 , the 2-years follow-up t_{0+2y} and considering the progression rate Δ as reported in paragraph 3.3. Correlations were evaluated using the [SPSS v25](#) partial correlation function, controlling for gender, education, age at visit and disease duration. The language disconnection mapping was performed considering all PPA (n=31).

Results

Correlations results between DTI measures and language assesment scores are reported in Table 3.8 (p-values < 0.01). At the baseline significant correlations were:

- WAB-repetition scores and MD and RD measures in the AF posterior;
- PPVT and MD measure in the UF;
- BNT and MD and RD measures in the UF.

In the follow-up:

- PPVT and FA measure in the UF;
- PPT and all DTI measures in the UF.

Considering longitudinal variations of language test scores (Equation 3.1) and DTI measures (Equation 3.2):

- PPT and MD measure in the UF.

Scatter plots of the significant correlations are shown in Figure 3.8.

Correlations between DTI measures and language assessment scores

WAB-Rep t_0	PPVT t_0	BNT t_0
AF post MD (-0.514)	UF MD (-0.494)	UF MD (-0.568)
AF post RD (-0.497)		UF RD (-0.522)
PPVT t_{0+2y}	PPT t_{0+2y}	Δ PPT
UF FA (0.58)	UF FA (0.544)	Δ UF MD (-0.525)
	UF MD (-0.602)	
	UF RD (-0.597)	

Table 3.8: Mapping language disconnections in PPA.

Significant correlations (p-value < 0.01) between language assessment scores and DTI measures in language tracts are reported, correlation R in brackets. Correlations were evaluated at the baseline t_0 , 2-years follow-up $t_0 + 2y$ and evaluating the longitudinal variation rate Δ . No significant correlations were found for WAB-AQ.

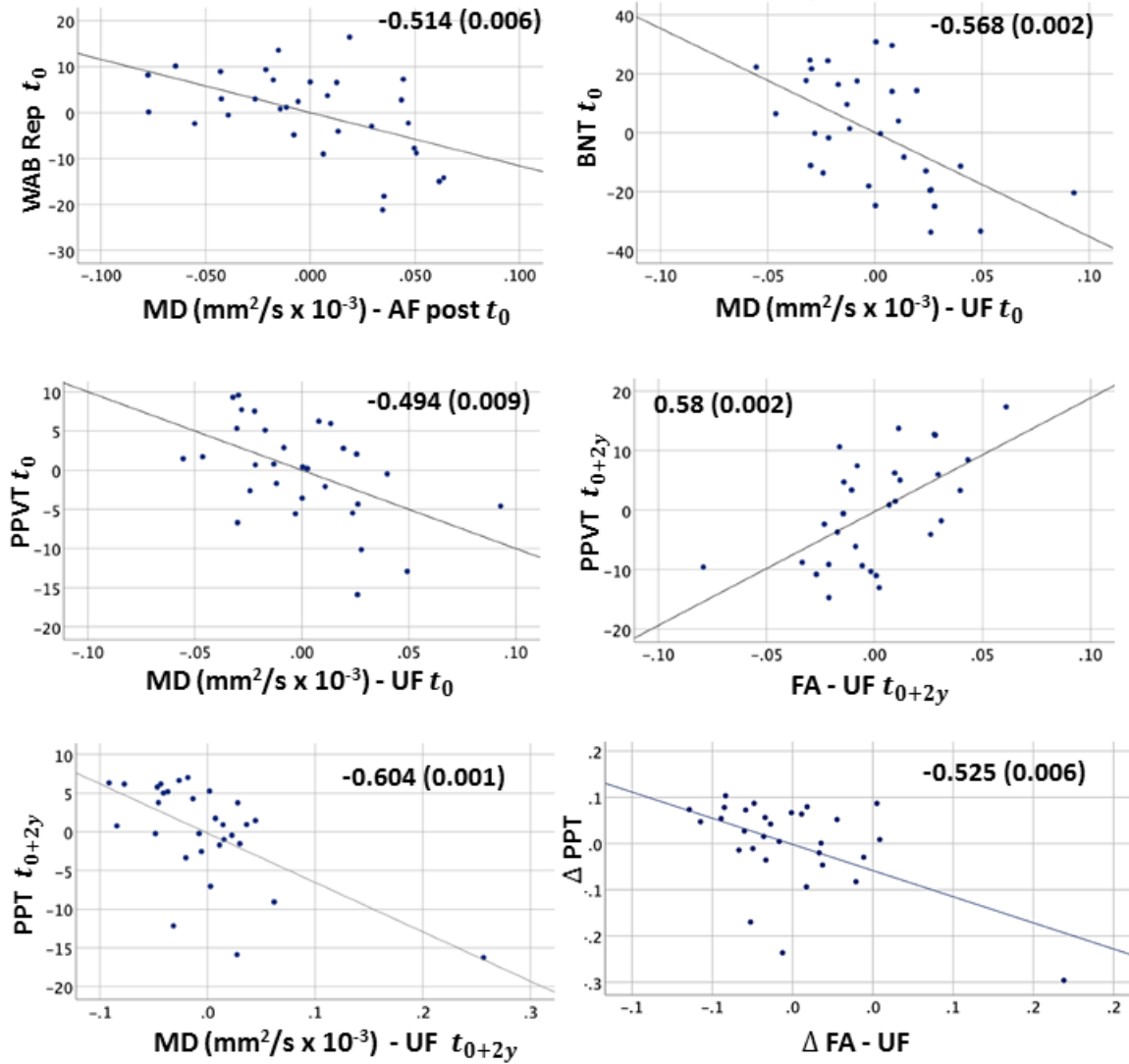


Figure 3.8: Correlation scatter plots of DTI measures and language assessment.

Scatter plots corresponding to the most significant correlations between DTI measures and language assessment are reported (p-value < 0.01). Correlations were evaluated controlling for gender, education, age at visit and disease duration. Thus, the residual values are reported in the scatter plots, showing the correlation R (p-values) and regression line.

CHAPTER 4

Metabolic plasticity in stroke-related aphasia

During my research period at the King's College London (from 1/9/2018 to 31/05/2019), at the Neuroanatomy and Tractography Laboratory ([NatBrainLab](#)), under the supervision of Prof. M.Catani, I had the possibility to collaborate with Dr. Jacqueline Stephanie Forkel, who is currently working on brain re-wiring and plasticity after stroke (Forkel et al., 2014; Forkel & Catani, 2018). In particular, she had a leading position in the prospective stroke project founding by [Welcome Trust](#).

Aim of this study was the longitudinal evaluation of stroke patients using ASL imaging and quantification of CBF in bilateral arterial territories and Broca's areas. Moreover, CBF measures were evaluated in a group of healthy controls.

The WAB-R scale was used to assess aphasia severity, and correlations between AQ and CBF were performed. Patients were recruited on the basis of clinical symptoms, in particular aphasia, by the the [NatBrainLab](#) stroke team, King's College. They underwent neuropsychological assessment and MRI, at baseline and at follow up: three months (language assessment only), six months (language assessment and MRI).

MATERIAL AND METHODS

Participants

Patients who had left ischemic stroke lesions and presented language dysfunctions were recruited by the [NatBrainLab](#) Stroke team, in summary:

- n=16 patients, 4M/12F, 63 ± 14 years old (mean \pm std).

Complete patients' demographics is reported in Table 4.1. Patients with hemorrhagic stroke were excluded from this study, and not any of the selected patients underwent thrombectomy; whereas n=6 had a thrombolysis treatment with Tissue-type Plasminogen Activator (TPA).

In addition, healthy controls have been recruited in the study:

- n=14 controls, 10M/4F, 54 ± 14 years old (mean \pm std).

Controls' demographic features are reported in Table 4.2.

In the current dataset (Tables 4.1 and 4.2), patients and controls are matched for age, education and handedness, but not for ethnicity and gender.

Thus, group comparisons between patients and controls were not performed, hopefully it will be possible after a new control recruitment.

WAB-R language evaluation

The Revised Western Aphasia Battery (Kertesz, 2007) was administrated to evaluate aphasia severity. Patients' AQ scores (Paragraph 3.1) are reported in Table 4.3, evaluated at baseline, with a 3 months and 6 months follow-up.

Table 4.1: Stroke patient study: demographic and clinical features.

ID	Gender	Age (y)	Education (y)	Ethnicity	Handedness	TPA
P_04	F	61	17	CAUCASIAN	R	yes
P_09	F	86	12	AFRO-CARRIBEAN	R	no
P_10	F	62	13	CAUCASIAN	R	no
P_13	F	76	14	CAUCASIAN	R	no
P_14	F	39	14	CAUCASIAN	R	yes
P_17	F	61	14	CAUCASIAN	R	no
P_22	M	67	23	SOUTH ASIAN	R	no
P_23	F	62	12	AFRO-CARRIBEAN	R	no
P_25	F	50	12	AFRICAN	R	no
P_38	F	72	12	CAUCASIAN	R	yes
P_46	M	74	17	CAUCASIAN	R	yes
P_48	M	72	12	AFRO-CARRIBEAN	R	no
P_49	M	77	17	CAUCASIAN	R	yes
P_44	F	34	14	CAUCASIAN	R	no
P_50	F	58	18	CAUCASIAN	R	yes
P_36	F	57	17	AFRO-CARRIBEAN	R	no

ID=Identification; F=Female; M=Male; R=Right; L=Left;

TPA=Tissue-type Plasminogen Activator treatment; P=Patient.

Recruitment: NatBrainLab Stroke team, King's College, London (UK).

Table 4.2: HC who underwent ASL imaging: demographic features.

ID	Gender	Age (y)	Education (y)	Ethnicity	Handedness
H001	F	41	14	CAUCASIAN	L
H002	M	46	18	ASIAN	R
H006	F	32	17	CAUCASIAN	R
H007	M	31	21	CAUCASIAN	R
H009	M	64	15	CAUCASIAN	R
H012	M	61	21	CAUCASIAN	R
H019	M	51	18	CAUCASIAN	R
H024	M	62	17	CAUCASIAN	R
H026	M	44	19	CAUCASIAN	R
H034	M	59	17	CAUCASIAN	L
H045	M	73	20	CAUCASIAN	R
H046	F	75	12	CAUCASIAN	R
H047	M	60	18	CAUCASIAN	R
H050	F	56	18	CAUCASIAN	R

F=Female; M=Male; R=Right; L=Left; H=Healthy controls.

Recruitment: NatBrainLab Stroke team, King's College, London (UK).

Table 4.3: Stroke patients WAB-R Aphasic Quotient (AQ).

ID	AQ baseline	AQ at 3 m	AQ at 6 m
P_04	49.6	76	83.8
P_09	64.3	70.7	71.2
P_10	88.3	98.2	97.1
P_13	83.7	97	97
P_14	40.1	96.8	96.2
P_17	78.6	97	96.6
P_22	59.7	90.7	90.8
P_23	81.6	88	87.2
P_25	72.1	88.6	80.3
P_38	75	91.3	93.5
P_46	39.5	94.4	93.4
P_48	59.5	80	80.3
P_49	96.6	97.6	99.3
P_44	88.3	99.6	94.6
P_50	90.8	100	99.4
P_36	45.2	82.3	91.9

P=Patient; AQ=Aphasic Quotient.

AQ baseline evaluated at 2.8 ± 1.3 days from stroke.

AQ 3 months follow-up evaluated at 91.6 ± 0.7 days from stroke.

AQ 6 months follow-up evaluated at 182.3 ± 1.2 days from stroke

Imaging

Recruited controls and stroke patients underwent a standardised MRI protocol at the Centre for Neuroimaging Sciences, Maudsley Hospital, London (UK), including T1w and ASL; acquisition parameters are reported in Table 4.4.

In addition, stroke patients underwent MRI longitudinally, at baseline acute/sub-acute and with a six months follow-up. MRI time post onset is reported in Table 4.5.

Scanner model = DISCOVERY_MR750			
Static field strength = 3T			
Coil = 32-channel head			
T1w		ASL	
Time of echo =	3.25 <i>ms</i>	Time of echo =	11 <i>ms</i>
Time of relaxation =	8.23 <i>ms</i>	Time of relaxation =	5124 <i>ms</i>
In-plane resolution =	0.9x0.9 <i>mm</i> ²	In-plane resolution =	1.88x1.88 <i>mm</i> ²
Slice thickness =	0.9 <i>mm</i>	Slice thickness =	3 <i>mm</i>
Field of view =	25.6 x 25.6 <i>cm</i> ²	Acquisition matrix =	128x128x55
Flip angle =	12°	Flip angle =	111°
Time of inversion =	450 <i>ms</i>	Post Delay Labelling =	2025 <i>ms</i>
		Number of excitations =	4

Table 4.4: Acquisition parameters of T1w and ASL imaging.

Site: Centre for Neuroimaging Sciences, King’s College London, Maudsley Hospital, London (UK).

4.1 REGISTRATION OF CBF MAPS TO MNI

The used GE scan (Table 4.4) automatically evaluated CBF maps, using the formula reported in the white paper by Alsop et al. (2015) (Equation 1.14). Subsequently, CBF maps were normalised to the MNI using the [ASLToolbox](#) software, developed by Abad et al. (2016) in collaboration with the Centre for Neuroimaging Sciences, King’s College London. This software is a matlab toolbox, [SPM](#) based, which com-

Table 4.5: MRI time post onset (TPO) from stroke.

ID	MRI baseline TPO (days)	MRI Follow-up TPO (days)
P_04	12	193
P_09	11	292
P_10	9	288
P_13	19	201
P_14	15	186
P_17	40	186
P_22	-	188
P_23	9	179
P_25	4	187
P_38	10	183
P_46	27	210
P_48	10	186
P_49	9	182
P_44	11	-
P_50	7	-
P_36	-	194

P=patient.

The dash symbol '-' indicates patients who did not undergo MRI.

puted the ASL processing pipeline shown in Figure 4.1. ASL analysis data input were:

- CBF maps, which were automatically calculated by the GE scanner;
- Proton Density (PD) images, which were acquired during the ASL sequence, and thus co-registered to the CBF map;
- T1w structural images acquired with high resolution (isotropic voxel 0.9 mm).

In particular, the PD images were used to register CBF maps to the structural T1w, which were subsequently registered to the MNI-152 2mm resolution space. In this manner, the CBF maps were first registered to T1w images, using the PD contrast, and then normalised to the MNI.

Results

T1w and CBF maps registered to the MNI space were reported for the healthy controls in Figure 4.2, for stroke patients longitudinally acquired in Figure 4.3, and for patients acquired only at one time point, baseline or follow-up, in Figure 4.4.

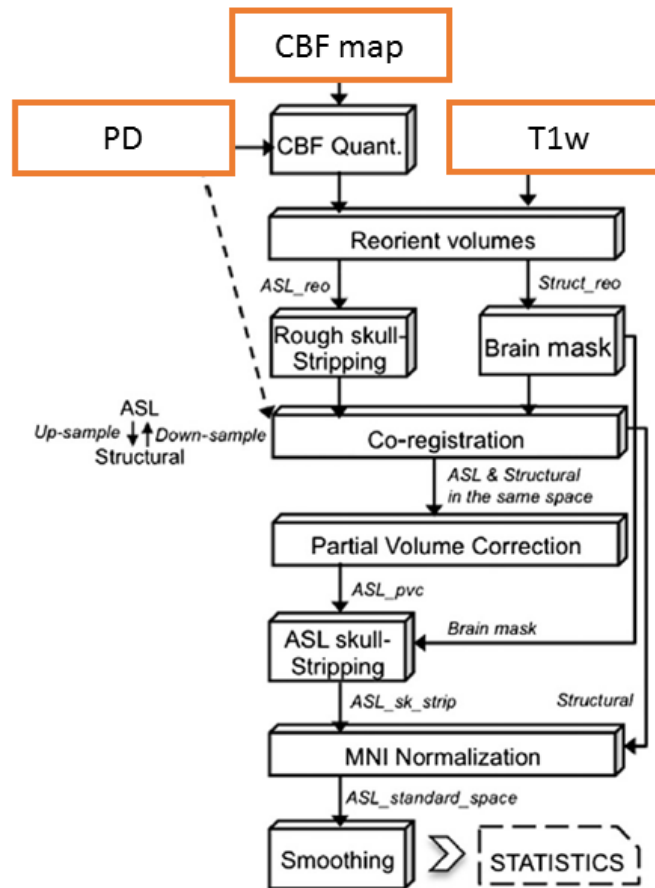


Figure 4.1: ASL registration pipeline to MNI space.

Image modified from Abad et al. (2016) representing the pipeline for processing ASL datasets in [ASLToolbox](#). Each box represents a main step in ASLToolbox procedure to register CBF maps to the MNI space, using PD and T1w registration. On the top, orange line boxes represent pipeline input data.

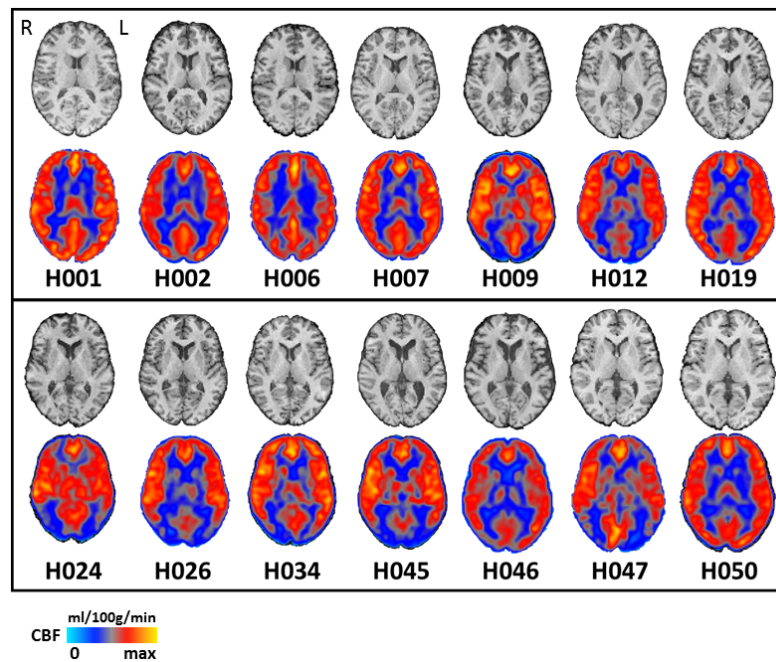


Figure 4.2: T1w and CBF maps of healthy controls.

Axial slices (MNI $z=4\text{mm}$) of T1w and CBF maps are shown for the $n=14$ healthy controls with corresponding ID (H0) (Table 4.2). CBF maps ($\text{ml}/100\text{g}/\text{min}$) has been re-scaled to better show intensity contrasts.

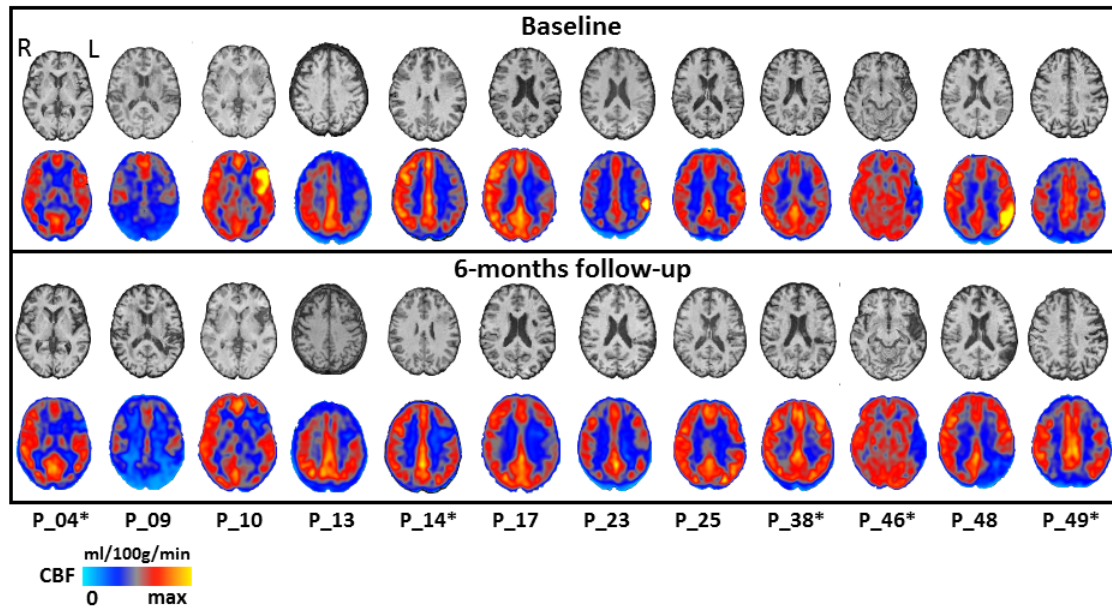


Figure 4.3: T1w and CBF maps, at baseline and follow-up, of stroke patients.

Axial slices of T1w and CBF maps registered to the MNI space are shown for stroke patients longitudinally acquired, at baseline top panel and at the 6-months follow-up in bottom panel. Axial slices have been selected related to stroke lesion localisation and CBF maps (ml/100g/min) and have been re-scaled for a better intensity contrast. In the bottom, corresponding patient ID (P_), introduced in Table 4.1, where the asterisks '*' indicate patients who had thrombolysis (TPA) treatment.

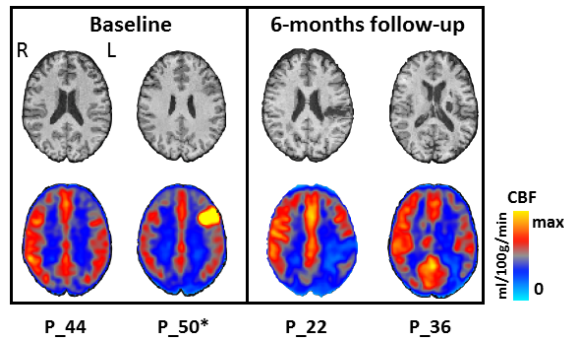


Figure 4.4: T1w and CBF maps, single time point, of stroke patients.

T1w and CBF maps registered to the MNI space are shown for stroke patients acquired with on time point, at baseline (left panel) or in the follow-up (right panel). Axial slices have been selected related to stroke lesion localisation and CBF maps (ml/100g/min) and have been re-scaled for a better intensity contrast. In the bottom, corresponding patient ID (P_), introduced in Table 4.1, where the asterisks '*' indicate patients who had thrombolysis (TPA) treatment.

4.2 VASCULAR ARTERY TERRITORIES AND BROCA'S ROIS

ROI statistics was evaluated both in different arterial territories defined by Tatu et al. (2012), and in the Broca area, defined using the cytoarchitectonic [JuBrain atlas](#):

- Anterior Cerebral Artery (ACA) territory ;
- Middle Cerebral Artery (MCA) territory;
- Posterior Cerebral Artery (PCA) territory;
- Broca's area (Brodmann 44 and 45) (Amunts et al., 1999).

The arterial territories ROIs were defined in the MNI-152 2mm brain (Figure 4.5), whereas Broca's regions, originally in the Colin27 1mm brain¹(Holmes et al., 1998), were registered to the MNI-152 atlas using linear ([FLIRT](#)) and non linear ([FNIRT](#))

¹Colin Holmes, a member of the MNI lab, was scanned 27 times. This was used as the standard template in SPM, matched to the MNI space.

registration tools from the fsl library. Calculated transformations were applied to Brodmann area 44 and 45 (Figure 4.6), merged to defined the Broca area. In these ROIs, median CBF measure was bilaterally evaluated.

In addition, I investigated hemispheric asymmetries by the calculation of the Laterality Index (LI), defined as proposed by Seghier (2008):

$$LI = \frac{CBF_{left} - CBF_{right}}{CBF_{left} + CBF_{right}} \quad (4.1)$$

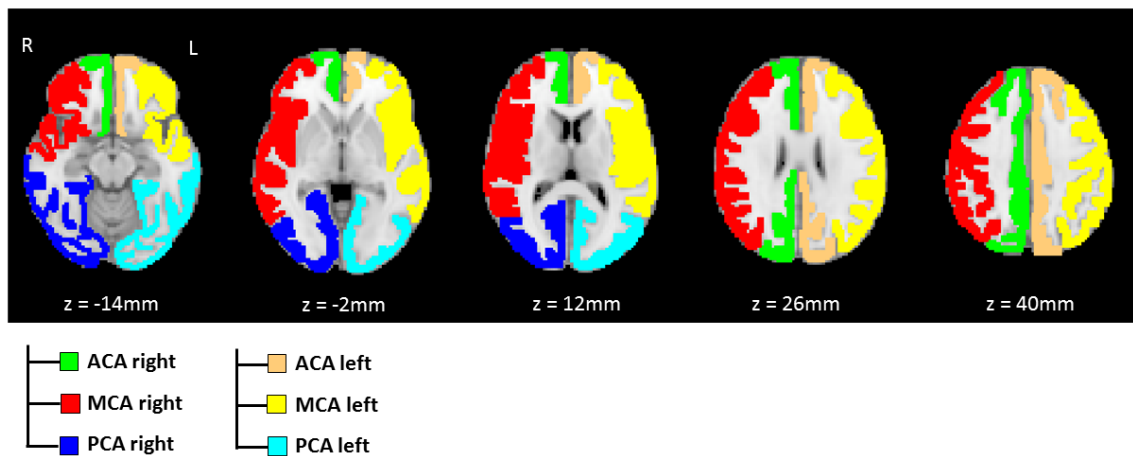


Figure 4.5: Cerebral vascular artery territory ROIs.

Axial projection of the arterial cerebral vascular (artery) territory ROIs (Tatu et al., 2012), evaluated bilaterally (anterior, middle and posterior). Coordinates are reported in the MNI-152 reference system.

4.3 CBF STATISTICS IN HEALTHY CONTROLS

In controls, CBF variability has been evaluated. In Figure 4.7, median and standard deviation of CBF maps across the n=14 healthy controls is shown. The highest standard deviation is in the posterior cerebral artery territory. Quantitative bilateral

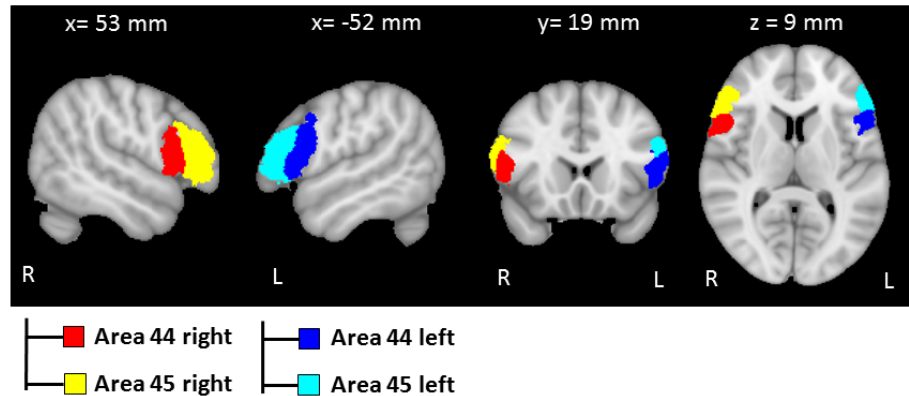


Figure 4.6: Broca area, Brodmann area 44 and 45

Axial projections of bilateral Brodmann area 44 and 45 (Amunts et al., 1999), registered to the MNI-152 space and the corresponding coordinates are reported.

median values for the different artery territories (anterior, middle and posterior) and Broca area are reported in the boxplots shown in Figure 4.8.

On the contrary, less variability across subjects was measured for the laterality index (equation 4.1) in the defined CBF ROIs (Figure 4.9).

Evaluating Pearson correlations between ASL ROI statistics and controls' age, significant correlations were present between absolute CBF quantification, whereas no any with CBF laterality index (Table 4.6).

4.4 CBF STATISTICS STROKE PATIENTS AND AQ CORRELATIONS

Baseline

Evaluating CBF ROI statistics at the baseline, significant correlations were found between LI in the MCA only and the MR timing post onset, on which patients underwent MRI, $R=-0.748$ $p\text{-value}=0.002$. Thus, with the passing of time from the stroke event, the CBF asymmetry of the MCA shifts from no lateralisation to an

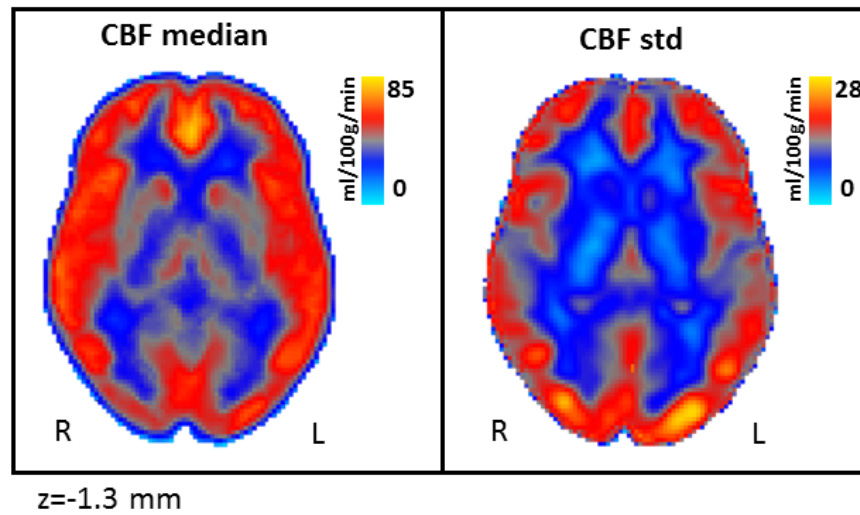


Figure 4.7: CBF median and standard deviation across healthy controls.

Axial slice on the MNI-152 2mm template, coordinate on the bottom left corner.

Left panel: median CBF measure across the $n=14$ healthy controls.

Right panel: standard deviation (std) of CBF measure in healthy controls.

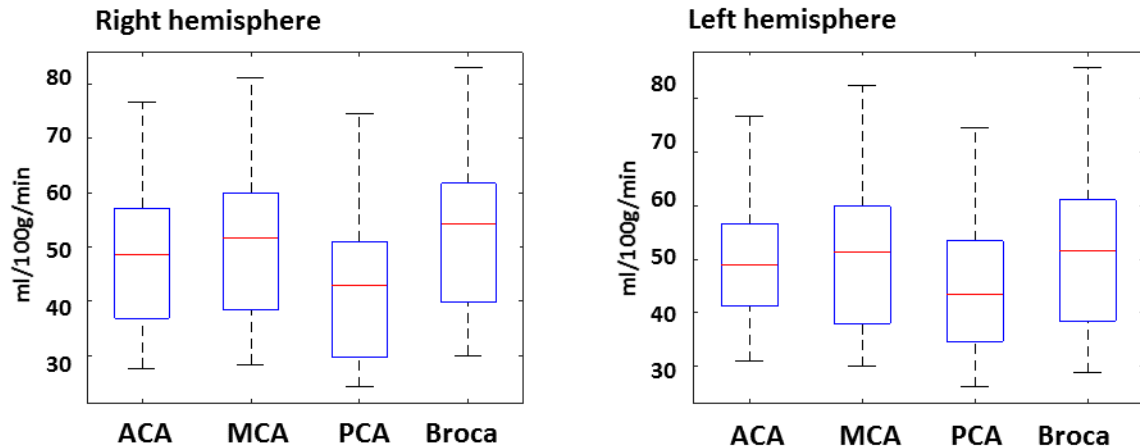


Figure 4.8: Bilateral CBF ROI statistics in healthy controls.

Boxplots of CBF median values in healthy controls ($n=14$) bilaterally evaluated for different cerebral arteries territories, anterior (ACA), middle (MCA) and posterior (PCA), and for the defined Broca areas (Brodmann 44 and 45).

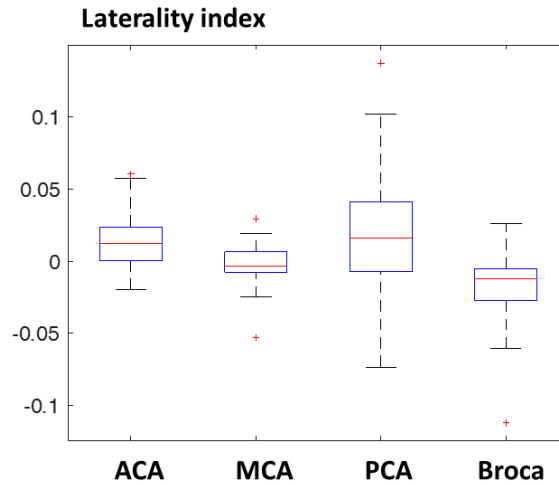


Figure 4.9: CBF LI ROI statistics in healthy controls.

Boxplots of CBF LI (equation 4.1), for healthy controls ($n=14$), bilaterally evaluated for the cerebral arteries territories, anterior (ACA), middle (MCA) and posterior (PCA), and for the defined Broca areas (Brodmann 44 and 45).

Table 4.6: Correlation of CBF statistics with age in controls.

CBF ROI	R	p-value
ACA right	-0.612	*
MCA right	-0.614	*
PCA right	-0.622	*
Broca right	-0.671	**
ACA left	-0.645	*
MCA left	-0.617	**
PCA left	-0.608	*
Broca left	-0.683	**
ACA LI	0.063	n.s.
MCA LI	-0.231	n.s.
PCA LI	0.152	n.s.
Broca LI	-0.318	n.s.

Pearson correlations between absolute CBF quantification and LI (Equation 4.1), evaluated bilaterally for the cerebral arteries territories, anterior (ACA), middle (MCA) and posterior (PCA), and for the defined Broca's areas (Brodmann 44 and 45). P-values are marked with asterisks (* < 0.05 , ** < 0.01) or not significant (n.s.) when p-value > 0.05 .

higher perfusion on the right hemisphere (Figure 4.10).

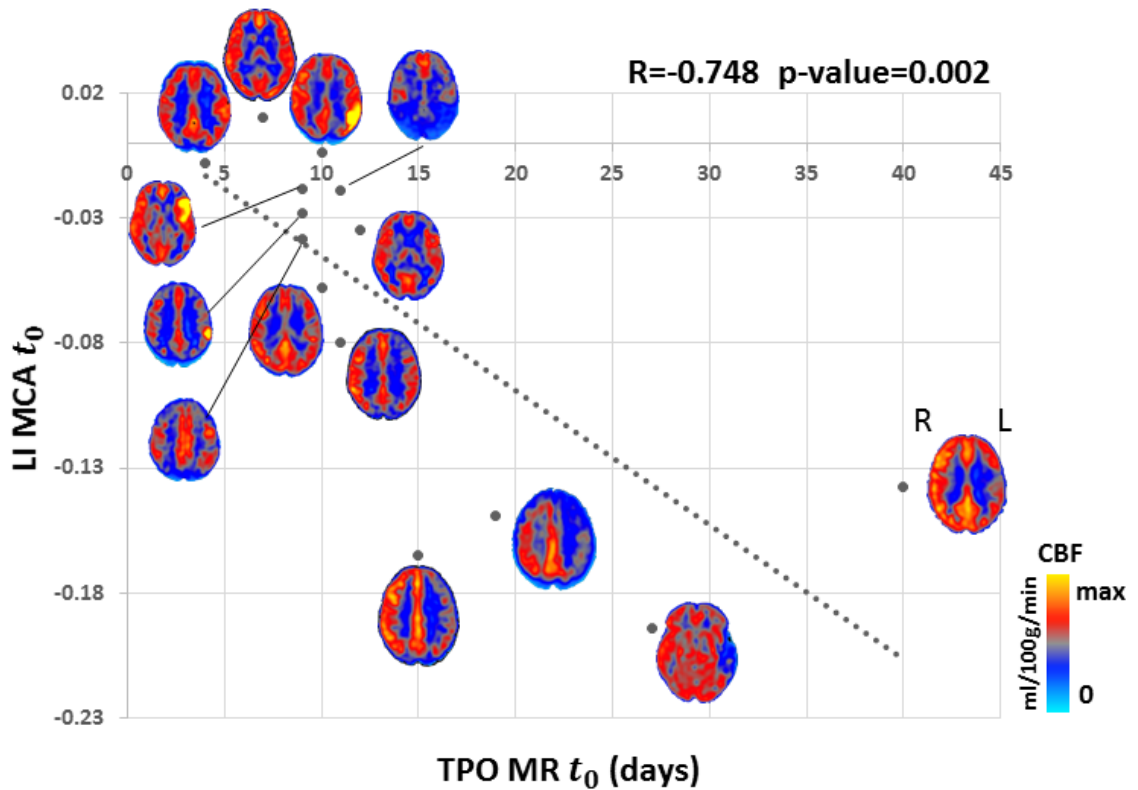


Figure 4.10: Scatter plot of LI MCA and Time Post Onset (TPO) MRI correlation.

Scatter plot reporting in x-axis the Time Post Onset (TPO) on which patients underwent MRI and in y-axis Laterality Index (LI) of the Middle Cerebral Artery (MCA) (Equation 4.1). Closely to scatter points the corresponding patient CBF map. On top right corner, Pearson correlation R and p -value. Correlation regression line is shown in dashed.

Follow-up

Evaluating CBF at a 6-months follow-up significant correlations were found between CBF ROI statistics and language scores using the WAB-R battery (Paragraph 3.1). In particular, significant correlations were found only for the MCA LI (Table 4.7) with:

- AQ at baseline;
- AQ differences between baseline and AQ at three and six months after stroke.

In addition, a significant correlation between MCA LI and patients' education was found ($R=-0.67$, $p\text{-value}=0.009$).

In Figure 4.11 the scatter plot for MCA LI and corresponding AQ difference between baseline and 6-months follow-up is reported. This correlation ($R=-0.759$, $p\text{-value}=0.002$) indicates that an increasing perfusion asymmetry towards the right hemisphere corresponds to an higher recovery in the AQ scale.

Moreover, dividing stroke patients in normal language functions ($AQ_{t0+6m}>93.8$) and mild-aphasia ($AQ_{t0+6m}<93.8$) (Pedersen et al., 2004), boxplot of both absolute CBF and LI of the MCA are reported in Figure 4.12. Patients who completely recovery language functions had an higher median CBF value bilaterally in the MCA, but with an asymmetry towards the right hemisphere.

In Figure 4.13 laterality indexes for all the cerebral artery territories and for Broca's area are reported, even if significant correlations with AQ scores were not found in this patient group.

In all the CBF ROIs a perfusion lateralisation towards the right was measured, and in particular in the Broca's area, if the stroke lesion involved the left inferior frontal gyrus.

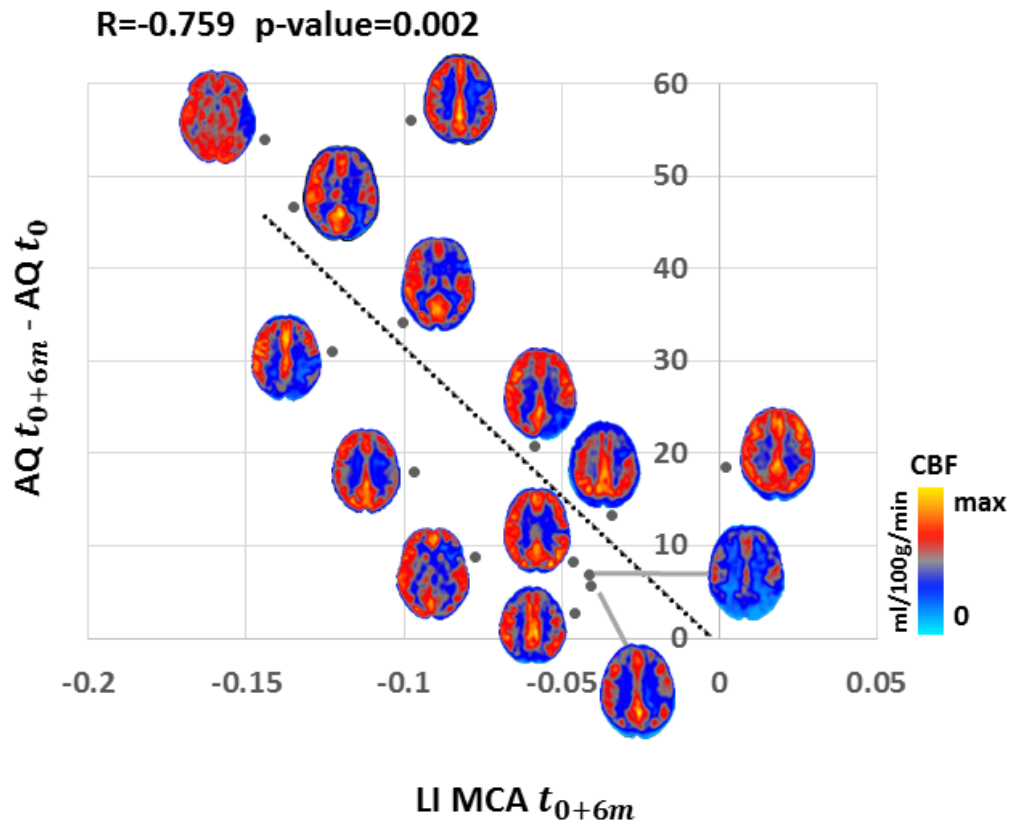


Figure 4.11: Scatter plot LI MCA and AQ recovery.

Scatter plot reporting in x-axis Laterality Index (LI) of the Middle Cerebral Artery (MCA) (Equation 4.1) and y-axis the Aphasic Quotient (AQ) difference between 6-months follow-up and baseline. Closing to scatter points the corresponding patient CBF map. On top left corner, Pearson correlation R and p-value. Correlation regression line is shown in dashed.

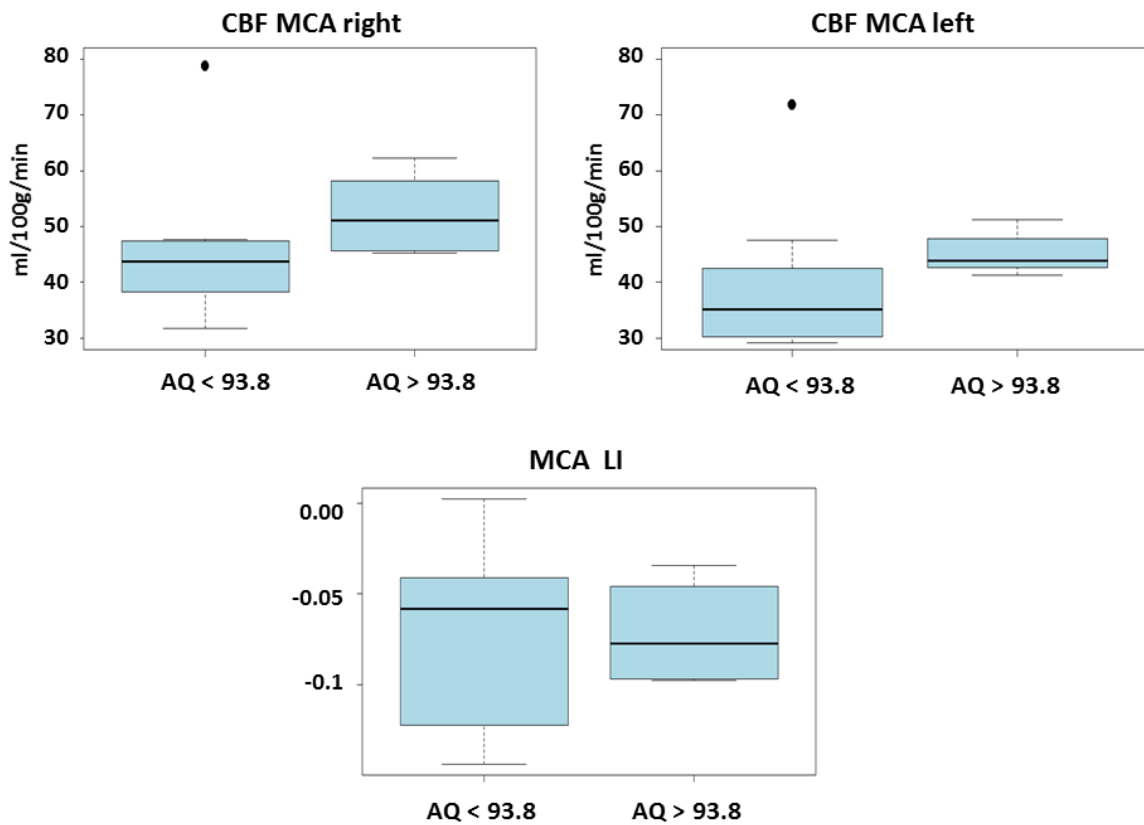


Figure 4.12: CBF quantification and LI of the MCA at 6-months follow-up.

Stroke patients were divided in two groups based on the AQ 6-months follow-up score: with normal language functions ($AQ_{t0+6m} > 93.8$) and mild-aphasia ($AQ_{t0+6m} < 93.8$) (Pedersen et al., 2004). **Top:** boxplots of Cerebral Blood Flow (CBF) absolute quantification bilaterally in the Middle Cerebral Artery (MCA). **Bottom:** boxplot for the MCA Laterality Index (LI) (Equation 4.1).

Correlations with LI MCA t_{0+6m}

	R	p-value < 0.01
AQ t_0	0.668	0.009
AQ t_{0+3m} - AQ t_0	-0.733	0.003
AQ t_{0+6m} - AQ t_0	-0.759	0.002

Table 4.7: Significant correlations CBF measures and AQ scale.

Significant correlations between the Laterality Index (LI) and the Middle Cerebral Artery (MCA) (Equation 4.1) and Aphasic Quotient (AQ) are reported. In particular with AQ at baseline, and the score differences between the 3 and 6-months follow-up and the baseline.

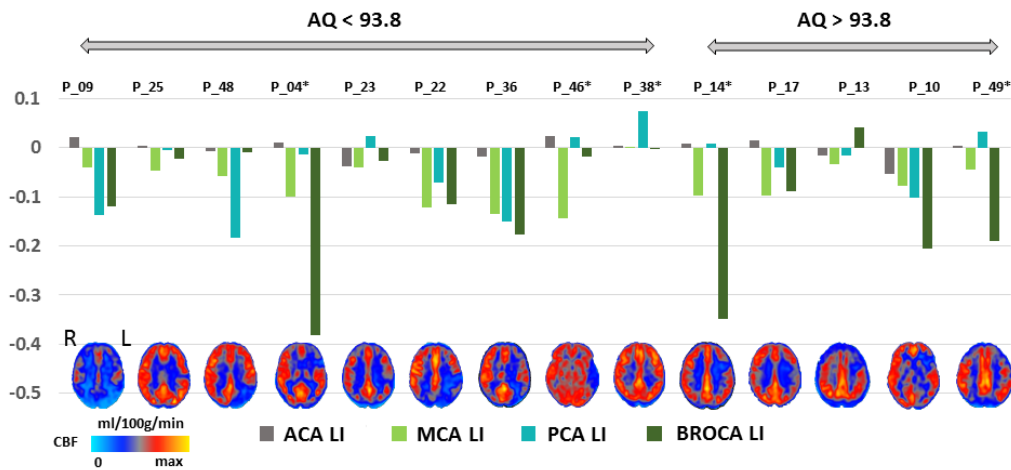


Figure 4.13: LI quantification in CBF ROI at 6-months follow-up.

Histogram representation of LI, in the x-axis patients' IDs introduced in Table 4.1, and in y-axis the corresponding Laterality Index (LI) (Equation 4.1) for the cerebral arteries territories, anterior (ACA), middle (MCA) and posterior (PCA), and for the defined Broca's areas. Patients were sorted along the x-axis with respect to AQ score at the 6-months follow-up, with normal language functions ($AQ_{t_{0+6m}} > 93.8$) and mild-aphasia ($AQ_{t_{0+6m}} < 93.8$) (Pedersen et al., 2004). On the bottom, patients CBF map axial slices corresponding to stroke lesions.

CHAPTER 5

Arcuate and uncinata tractography in healthy controls

In this chapter, the arcuate and uncinata were bilaterally investigated in a group of healthy controls. In particular, automatic tractography procedures and a new along-tract algorithm suitable for different tractography methods were implemented. Findings on the arcuate fasciculus were published last year (Talozzi et al., 2018c) (see article in section B), and previously presented at different conferences as oral communication (Talozzi et al., 2017a), electronic poster (Talozzi et al., 2017b) and traditional posters (Talozzi et al., 2016a), (Talozzi et al., 2016b).

Preliminary results on the uncinata fasciculus were presented at national (Talozzi et al., 2018b) and international meetings (Talozzi et al., 2018a).

Moreover, I was awarded with educational stipends to attend the 25th ISMRM Annual Meeting and Exhibition, 22-27/04/2017, Honolulu (USA), and the Joint Annual Meeting ISMRM-ESMRMB, 16-21/06/2018, Paris, (France). In addition, I participated to the 1st MRtrix3 workshop, 22-24/06/2018, Paris (France), to deepen my knowledge in constrained spherical deconvolution tractography.

Aim of the study was to evaluate the arcuate fasciculus using different tractography methods, both deterministic and probabilistic, to address the question of how tractography methods influence the AF tractography in the right hemisphere (Bain et al., 2019). For this purpose along-tract procedures were implemented and subsequently applied to bilateral investigate the uncinata fasciculus and hemispheric asymmetries.

Participants

In this session healthy controls recruited by the Functional MR Unit, Department of Biomedical and Neuromotor Sciences of the University of Bologna, were analysed: n=29 HC, 15M/14F, 35.8 ± 15.9 years old. Detailed controls demographics were reported in table 5.1.

Participants were recruited among Hospital and University workers and their relatives. In all participants a current or past history of neurological or psychiatric disorders and major brain injuries were excluded, signal and/or morphology alterations on brain images were excluded.

Imaging

Participants underwent a standardised brain MRI protocol including T1-weighted and DW imaging. Acquisition parameters of T1w scans were previously reported in table 2.2, and DWI parameters are reported in table 5.2.

Preprocessing

To assess the quality of DWI data, a detailed visual inspection slice by slice was performed, and subsequently automatic slice intensity dropout evaluation and interpolation correction by an homebrew developed software by PhD David Neil Manners at the Functional MR Unit, Department of Biomedical and Neuromotor Sciences of the University of Bologna.

Eddy-current correction and local fitting of the diffusion tensor parameters were performed using the [FMRIBs Diffusion Toolbox](#). For both T1w and DWI, [BET](#) was used for brain extraction, and images were non-linearly registered using [ART 3dwarper](#) software and the processing pipeline developed by Manners et al. (2017).

Table 5.1: HC recruited in the DTI study: demographic features.

ID	Gender	Age (y)	Writing hand
C_01	F	23	R
C_02	F	21	R
C_03	M	20	R
C_04	F	19	L
C_05	M	60	R
C_06	M	22	L
C_07	F	49	R
C_08	M	49	R
C_09	M	33	R
C_10	M	32	R
C_11	F	73	R
C_12	F	83	R
C_13	M	24	R
C_14	F	28	R
C_15	M	51	R corrected
C_16	F	32	R
C_17	F	28	R
C_18	M	28	R
C_19	F	46	R corrected
C_20	F	30	R
C_21	M	27	R
C_22	F	24	R
C_23	F	37	R
C_24	F	24	R
C_25	M	43	R
C_26	M	29	R
C_27	M	22	L
C_28	M	40	R
C_29	M	42	R

F=Female; M=Male; R=Right; L=Left; C=Control.

Recruitment: Functional MR Unit - Department of Biomedical and Neuromotor Sciences, University of Bologna.

Table 5.2: Acquisition parameters of DTI

Static field strength =	1.5 <i>T</i>
Scanner model =	SIGNA HDx 15 GE
Sequence =	single-shot SE-EPI
b-value =	900 <i>s/mm²</i>
Time of echo =	87 <i>ms</i>
Time of relaxation =	10000 <i>ms</i>
In plane resolution =	1.25 x 1.25 <i>mm²</i> *
Slice thickness =	3 <i>mm</i>
Field of view =	32 x 32 <i>cm²</i>
n. of diffusion gradient directions =	64
n. of null b-value =	7

*automatic scanner upsample 0.5 factor.

Site: S.Orsola-Malpighi Hospital, Pad. 11, Bologna (IT)

5.1 BILATERAL AF AUTOMATIC TRACTOGRAPHY WITH DIFFERENT METHODS

Tractography methods

Tractography of the AF was performed using three different approaches:

- probabilistic tractography based on the ball-and-sticks model - [Probtrackx2](#);
- deterministic tractography with constrained spherical deconvolution - [CSTdet](#);
- probabilistic tractography with constrained spherical deconvolution - [CSTprob](#).

Probtrackx2 is part of the [Fsl](#) software. It allows probabilistic fibre tracking after the Bayesian estimation of diffusion parameters (Bedpostx) using the ball and sticks model (Behrens et al., 2003).

CSTdet and CSTprob were performed using the [Mrtrix3](#) software, which provides an estimate of the Fibre Orientation Density (FOD) function by deconvolving the diffusion signal using non-negatively constrained spherical deconvolution (Tournier

et al., 2007). The Tournier algorithm (Tournier et al., 2013) was chosen to estimate the response function, and the maximum harmonic degree was set at $l_{max}=8$. Subsequently, both deterministic and probabilistic fiber tracking was performed. Deterministic streamlines were evaluated by stepping along the local fibre orientation and performing a peak-finding procedure on the FOD once per point (Tournier et al., 2012), using the `SD_Stream` function. Probabilistic streamlines were obtained by `iFOD2`, via random sampling of the FOD, using the 2nd order integration over fibre orientation distribution (Tournier et al., 2010).

For the AF tractography an automatic procedure was implemented. Tractography ROIs were defined in the MNI-152 space (2mm voxel resolution):

- seed mask located in the WM of the AF just anterior to the point where the tract begins to arc towards temporal GM (Giorgio et al., 2010) (in green in Figure 5.1);
- target masks located in the GM of the frontal and temporal lobes, according to the Harvard-Oxford probabilistic atlas which was thresholded at 25% of subjects (in blue in Figure 5.1), adapting the procedure of (Galantucci et al., 2011).

The AF was delineated starting from the defined WM seed mask and requiring the streamlines to traverse both frontal and temporal GM targets. Tractography results were thresholded at 10% with respect to the maximum of connectivity within each voxel.

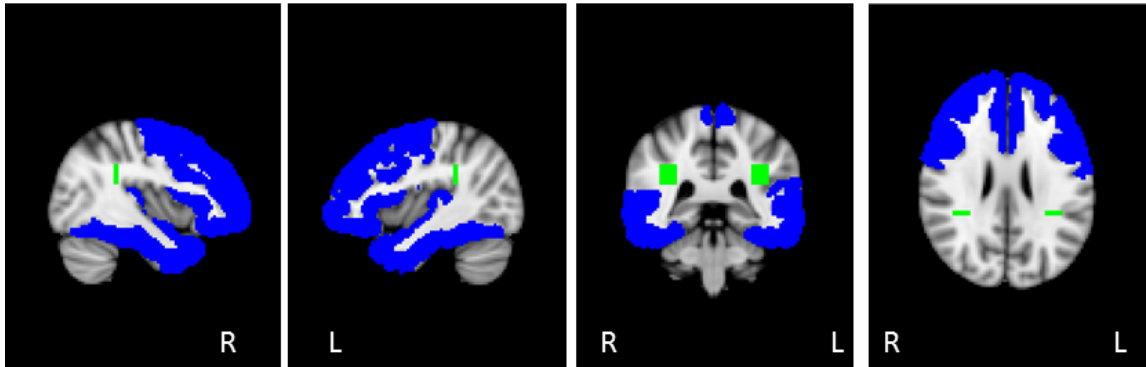


Figure 5.1: Tractography ROIs for the AF

The ROIs used for the AF tractography were reported on the MNI-152 space. The seed ROI (green) was defined in the WM underlying the angular gyrus; the target ROIs (blue) were defined in the frontal and temporal GM according to the Harvard-Oxford probabilistic atlas, thresholded at 10% of subjects.

Results

Tractography results are shown in Figure 5.2 using group variability maps. Tractography of the AF was bilaterally successful for all the subjects with the exception of the right AF in one control (male, right handed). Moreover, for CSTdet group variability maps there were not voxels were all controls presented the AF tracts, in fact the group variability maximum was at the 65.5% of controls for the right AF and 75.9% on the left. On the contrary, for probabilistic methods group variability maximum was 100 % of subjects bilaterally.

In addition, in Figure 5.2 and 5.3 cortical terminations were signed, and in particular bilateral middle temporal gyrus terminations were detected, whereas superior temporal gyrus projections were found only on the left. With respect to frontal AF terminations, bilateral inferior frontal gyrus projections were detected, whereas terminations towards the precentral operculum were detected only on the left.

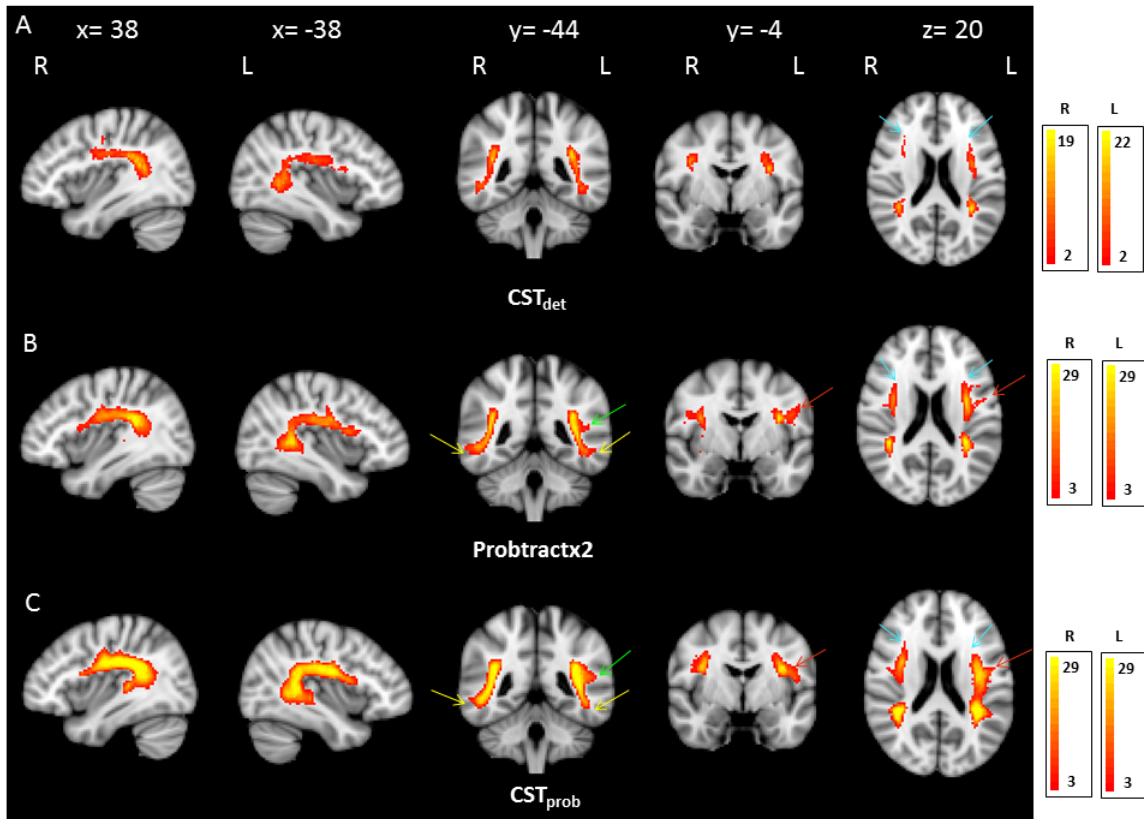


Figure 5.2: Bilateral AF group variability maps.

Sagittal, coronal and axial views of the group variability (GV) maps, thresholded at the 10% of subjects, for the different tractography algorithms: CSTdet (A), Probtrackx2 (B), CSTprob (C). The intensity scales of the maps are associated to the minimum and maximum of the subjects represented by the GV maps. Coordinates of the shown projections are reported in mm in the MNI space. The arrows indicate with different colours characteristic GM terminations of the AF: superior temporal gyrus (green), middle temporal gyrus (yellow), precentral operculum (red) and inferior frontal gyrus (turquoise).

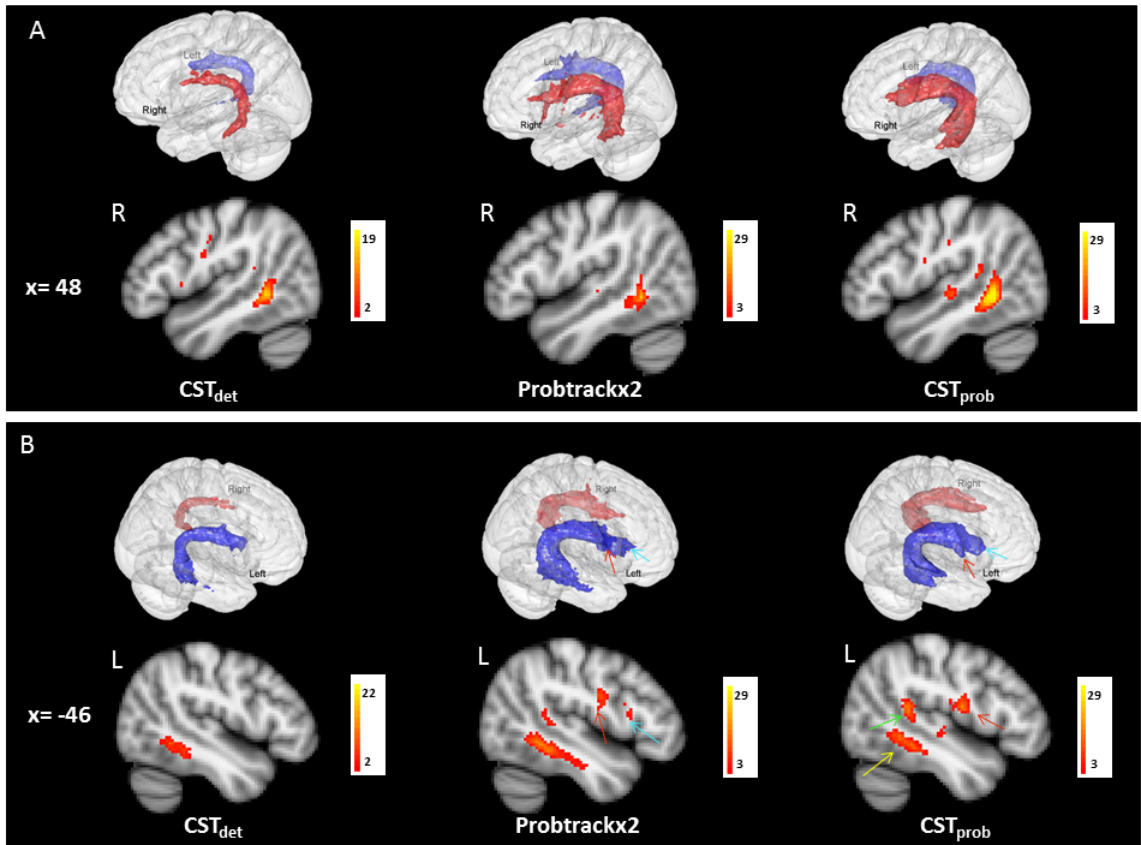


Figure 5.3: Bilateral AF 3D-rendering and group variability maps.

For both A and B, upper: 3-dimensional rendering of group variability (GV) maps volume for the three tractography algorithms, left AF (blue) and right AF (red); lower: GV map of GM projections of the AF, on the MNI-152 brain. A upper: right lateral view. A lower: right sagittal section. B upper: left lateral view. B lower: left sagittal section. The angle of view of the 3-dimensional rendering is set individually for each algorithm to better visualise GM projections. The coordinates of the GV projections shown are reported in mm in the MNI space. The coloured arrows indicate characteristic GM terminations of the AF: superior temporal gyrus (green), middle temporal gyrus (yellow), precentral operculum (red) and inferior frontal gyrus (turquoise).

5.2 BILATERAL UF AUTOMATIC TRACTOGRAPHY

Tractography methods

The UF tractography was performed using the CSTprob (defined in paragraph 5.1). Tractography ROIs were defined on the MNI space, in the WM before reaching both the anterior temporal lobe and the fronto-orbital cortex, as suggested in the [AutoPtx](#) fsl toolbox (see figure 5.4). Tractography results were thresholded at 10% of the maximum of connectivity within each voxel.

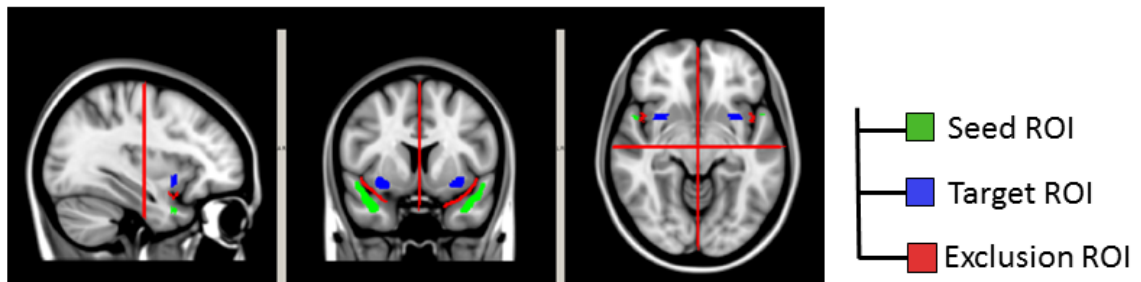


Figure 5.4: Tractography ROIs for the UF.

The ROIs used for the UF tractography were reported on the MNI-152 space and defined as in the [AutoPtx](#) toolbox.

Results

For all subjects the UF was successfully reconstructed in both hemispheres. Group variability maps showed different cortical terminations towards the frontal lobe in particular, the left UF was more dorsally located projecting towards the lateral frontal orbital cortex, whereas the right UF was more ventrally located targeting the right medial frontal orbital cortex and frontal pole (see Figure 5.5).

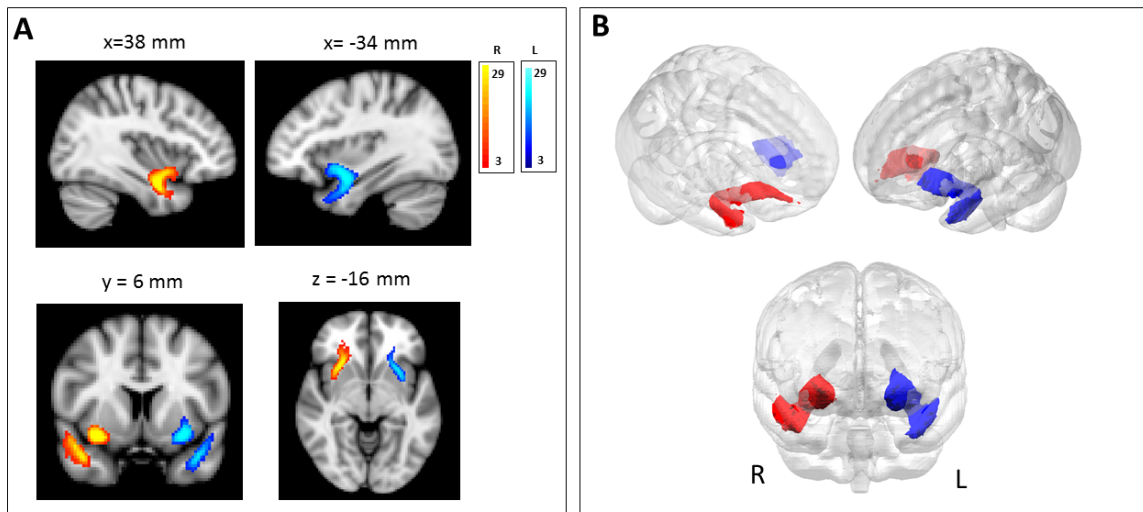


Figure 5.5: Bilateral UF group variability maps.

A: Sagittal, coronal and axial views of the group variability (GV) maps, thresholded at the 10% of subjects; the intensity scales of the maps are scaled to the minimum and maximum of the subjects represented by the GV maps. Coordinates of the projections shown were reported in mm in the MNI-152 standard space.

B: 3-dimensional rendering of GV maps volume on the MNI-152 brain, thresholded at the 10% of subjects. The left UF was coloured in blue, the right UF in red.

5.3 ALONG-TRACT ANALYSIS - LAPLACIAN MODELLING

Along-tract algorithm

During my PhD course, I developed an along-tract algorithm that can be applied to both deterministic and probabilistic tractography results. This method allow to perform along-tract analysis of diffusion measures and map tract localisation. For this purpose I used the Laplacian spectral graph properties, in particular I evaluated the Fiedler vector (Ψ) that corresponds to the smallest non-zero eigenvalue. Ψ can be used to establish an intrinsic coordinate system for elongated tubular structures, where the Ψ gradient follows the shape of the object and its maximum and minimum are at the two extremes of the elongated objects (Chung et al., 2011). I used this Ψ gradient property to perform along-tract analysis. First, tract surface was modelled using triangular meshes, and subsequently a connectivity matrix of mesh node localisation computed. Along-tract evaluation was restricted to the UF and AF bundle core, defined as the compact WM before branching towards GM terminations. For the AF bundle core definition, coordinates of the WM ROI proposed in Giorgio et al. (2010) were used (Figure 5.6 A); whereas for the UF, I used the tractography seed and target ROI (Figure 5.6 B).

Subsequently, the obtained mesh segmentation was projected to each tract voxel by a nearest neighbour association between mesh vertex and volume voxels. Ψ values were sorted and divided in different intervals to define along-tract segments. In particular, tract division number was defined in relation to tract volume, as the maximum number for which a unique association between mesh nodes and volume voxels was preserved for all subjects. The proposed along-tract algorithm was implemented in Matlab (R2017a).

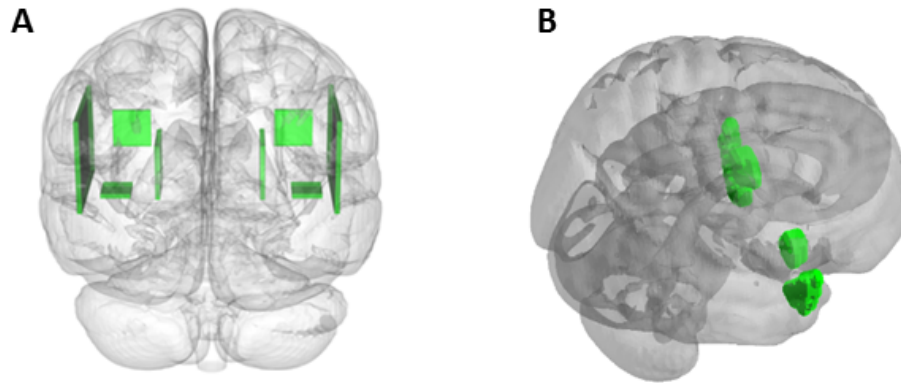


Figure 5.6: ROI for WM core definition for AF and UF.

The ROIs used in the definition of WM cores, compact part of WM bundle before branching towards GM terminations, are reported. The ROIs used for this definition are reported in green for the AF (panel A) and for the UF (panel B).

Results

The Laplacian along-tract algorithm was successfully applied in both the AF and UF tracts. In particular, tract division was defined as:

- fifteen along-tract segments for the AF;
- eight along-tract segments for the UF.

In Figure 5.7 median along-tract segmentation across subjects is reported of the AF, considering different tractography methods, whereas in Figure 5.8 the along-tract analysis for the UF tract.

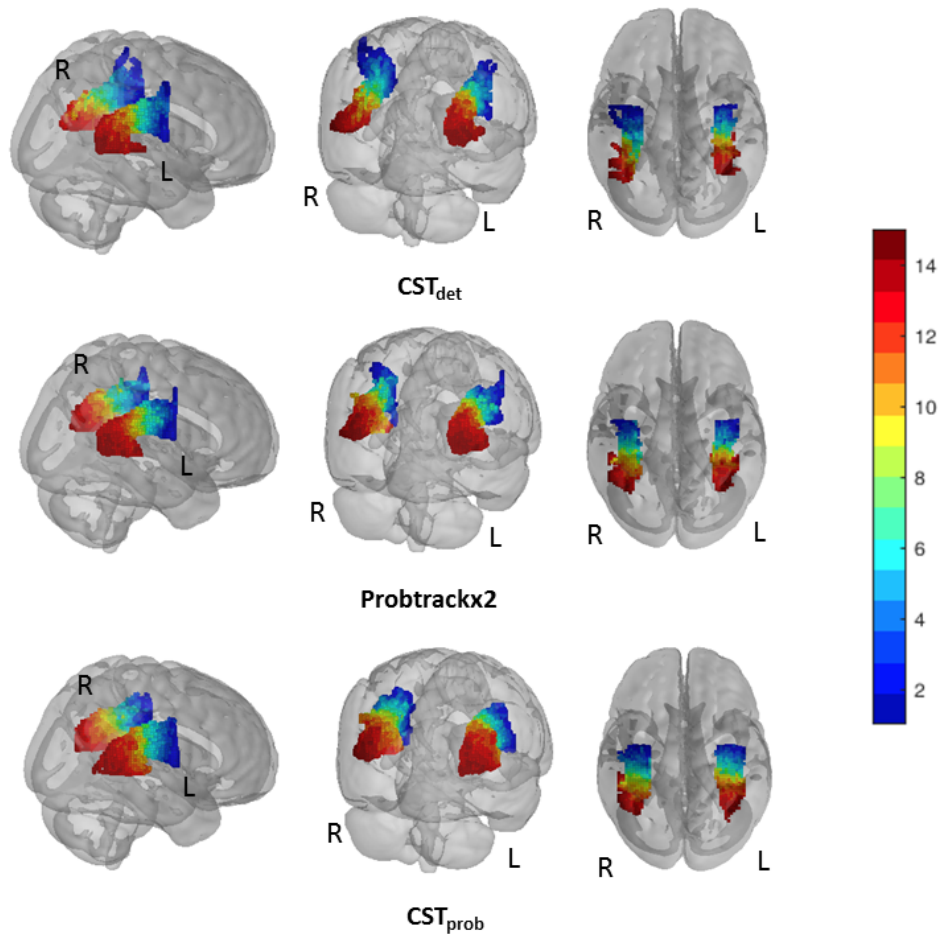


Figure 5.7: Along-AF Laplacian modelling.

3-dimensional rendering of the mean Laplacian AF along-tract modelling across subjects, for each tractography method, dividing the AF into 15 segments (blue= 1^{st} frontal segment, red= 15^{th} temporal segment), projected onto the MNI-152 brain.

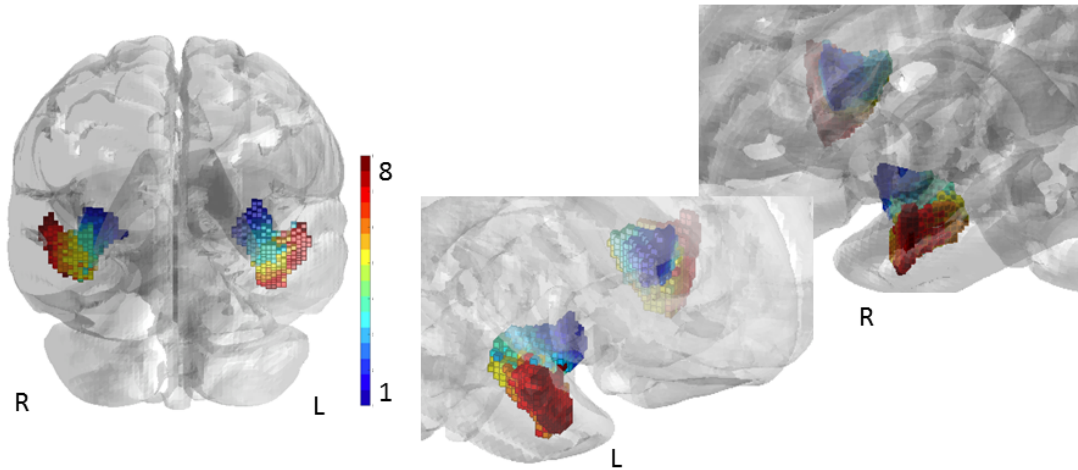


Figure 5.8: Along-UF Laplacian modelling.

3-dimensional rendering of the mean Laplacian UF along-tract modelling across subjects, dividing the UF into eighth segments (blue=1st frontal segment, red=15th temporal segment), projected onto the MNI-152 brain.

5.4 HEMISPHERIC ASYMMETRIES

Statistical methods

Along-tract volume was evaluated and centroid coordinates of along-tract segments reported in the MNI space coordinate system. Segment coordinates were plotted and used to evaluate curvature mapping. Moreover, DTI metrics (FA, MD, λ_1 , λ_2 and λ_3) in the defined WM core and along-tract were evaluated. Statistical analyses were conducted with MATLAB R2016a. The Kolmogorov-Smirnov test was performed to test whether diffusion metrics were normally distributed. The median and interquartile values of tract volume and diffusion parameters were calculated. Subsequently, the non-parametric paired Wilcoxon signed-rank test, was used for left-right comparisons, with a significant level set at $p < 0.05$ and corrected by the FDR (False Discovery Rate) method for multiple comparisons across

along-tract segments.

Arcuate

The AF volume was higher using the probabilistic tractography methods than the deterministic one, especially with CSTprob. The tract volume was significantly bigger in the left AF with Probtrackx2, while there were no significant differences in tract volume between hemispheres with the CST algorithms (table 5.3).

FA differed between the hemispheres only in the CSTprob, showing a lower median value of the left FA and correspondingly λ_1 was significantly higher in the right and λ_2 in the left hemisphere. With the CSTdet we measured higher λ_2 on the left and higher λ_3 on the right; with Probtrackx2 we measured an higher λ_1 and λ_3 on the right, and higher λ_2 on the left. Right and left MD values were not significantly different for any of the three tractography algorithms (table 5.3).

Evaluating along-AF volume asymmetries, with CSTdet and CSTprob we measured significant volume differences only in isolated segments, whereas with Probtrackx2 the tract volume was bigger on the left in the temporal region of tract (Figure 5.9). For along-AF asymmetries in DTI metrics and tract curvature, all the results are reported in appendix B as in the original published paper (Talozzi et al., 2018c).

Table 5.3: Wilcoxon signed rank test results comparing the right and left AF tractography results for the three proposed algorithms (CSTdet, Probtrack2, CSTprob). In table, median and interquartile (IR) values of the tract volume and diffusion parameters are shown for the right and left AF. Associated p-values are reported: * < 0.05, ** < 0.01, *** < 0.001.

Hemispheric AF asymmetries WM core

CSTdet

	Right AF	Left AF	p-value
Volume (mm ³ x 10 ³)	1.7 (1.1)	2.0 (1.4)	n.s.
FA	0.41 (0.04)	0.43 (0.06)	n.s.
MD (mm ² /s x 10 ⁻³)	0.73 (0.03)	0.73 (0.03)	n.s.
λ_1 (mm ² /s x 10 ⁻³)	1.10 (0.09)	1.10 (0.08)	n.s.
λ_2 (mm ² /s x 10 ⁻³)	0.65 (0.05)	0.68 (0.05)	*
λ_3 (mm ² /s x 10 ⁻³)	0.46 (0.04)	0.42 (0.05)	**

Probtrack2

	Right AF	Left AF	p-value
Volume (mm ³ x 10 ³)	2.7 (0.7)	3.5 (0.9)	**
FA	0.43 (0.06)	0.43 (0.04)	n.s.
MD (mm ² /s x 10 ⁻³)	0.73 (0.03)	0.74 (0.03)	n.s.
λ_1 (mm ² /s x 10 ⁻³)	1.11 (0.08)	1.09 (0.03)	*
λ_2 (mm ² /s x 10 ⁻³)	0.66 (0.04)	0.68(0.06)	***
λ_3 (mm ² /s x 10 ⁻³)	0.45 (0.04)	0.42 (0.04)	*

CSTprob

	Right AF	Left AF	p-value
Volume (mm ³ x 10 ³)	6.3 (1.3)	6.9 (1.5)	n.s.
FA	0.41 (0.04)	0.39 (0.04)	***
MD (mm ² /s x 10 ⁻³)	0.74 (0.03)	0.74 (0.02)	n.s.
λ_1 (mm ² /s x 10 ⁻³)	1.10 (0.05)	1.05 (0.04)	***
λ_2 (mm ² /s x 10 ⁻³)	0.67 (0.04)	0.70 (0.04)	***
λ_3 (mm ² /s x 10 ⁻³)	0.46 (0.04)	0.46 (0.03)	n.s.

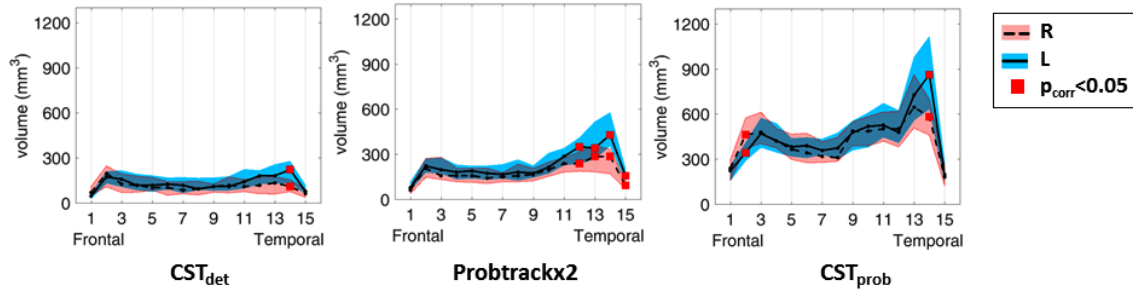


Figure 5.9: Along-AF segment volumes for different tractography methods.

Along-AF volume comparison between the right (dashed line) and left (continuous line) AF tractography results, for the three algorithms employed (CSTdet, Protrackx2, CSTprob). In the plots median volumes are displayed along with interquartile range (shaded area: red for the right, blue for the left). The red squares mark significant left-right differences with p-value < 0.05 after FDR correction.

Uncinate

At the whole-UF core level, we found significant left-right differences only in the FA measure, with a left hemisphere values being higher (table 5.4).

At the along-UF level, we found a greater volume at right compared to left ($R > L$) in the medial part of the UF core, and the opposite ($L > R$) in temporal segments (Figure 5.10).

Along the UF an FA $L > R$ was measured, corresponding with: an $R > L$ MD in one medial segment, an $L > R$ λ_1 in some temporal segments and an $R > L$ λ_3 along the UF (Figure 5.11). With regard to UF curvature mapping (Figure 5.12), the left UF segments were located more medially with respect to the right (lower $|x|$); frontal UF segments were more superiorly located (higher z), whereas temporal segments of the left UF were more posteriorly (lower y) and inferiorly (lower z) located with respect to the right.

Table 5.4: Wilcoxon signed rank test results comparing the right and left UF tractography results. In table, median and interquartile (IR) values of the tract volume and diffusion parameters are shown for the right and left AF.

Hemispheric UF asymmetries WM core

	Right UF	Left UF	p-value
Volume ($\text{mm}^3 \times 10^3$)	2.2 (0.7)	2.4 (0.5)	n.s.
FA	0.30 (0.05)	0.33 (0.04)	0.4*
MD ($\text{mm}^2/\text{s} \times 10^{-3}$)	0.84 (0.04)	0.84 (0.03)	n.s.
λ_1 ($\text{mm}^2/\text{s} \times 10^{-3}$)	1.16 (0.05)	1.17 (0.04)	n.s.
λ_2 ($\text{mm}^2/\text{s} \times 10^{-3}$)	0.79 (0.04)	0.78 (0.04)	n.s.
λ_3 ($\text{mm}^2/\text{s} \times 10^{-3}$)	0.6 (0.05)	0.59 (0.04)	n.s.

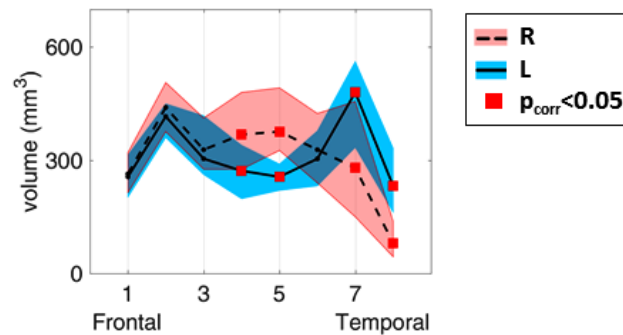


Figure 5.10: Along-UF segment volume asymmetries.

Along-UF segment volumes comparison between the right (dashed line) and left (continuous line) UF tractography results. In the plots the median volumes are displayed along with the interquartile range (shaded area: red for the right, blue for the left). The red squares mark significant left-right differences with $p\text{-value} < 0.05$ after FDR correction.

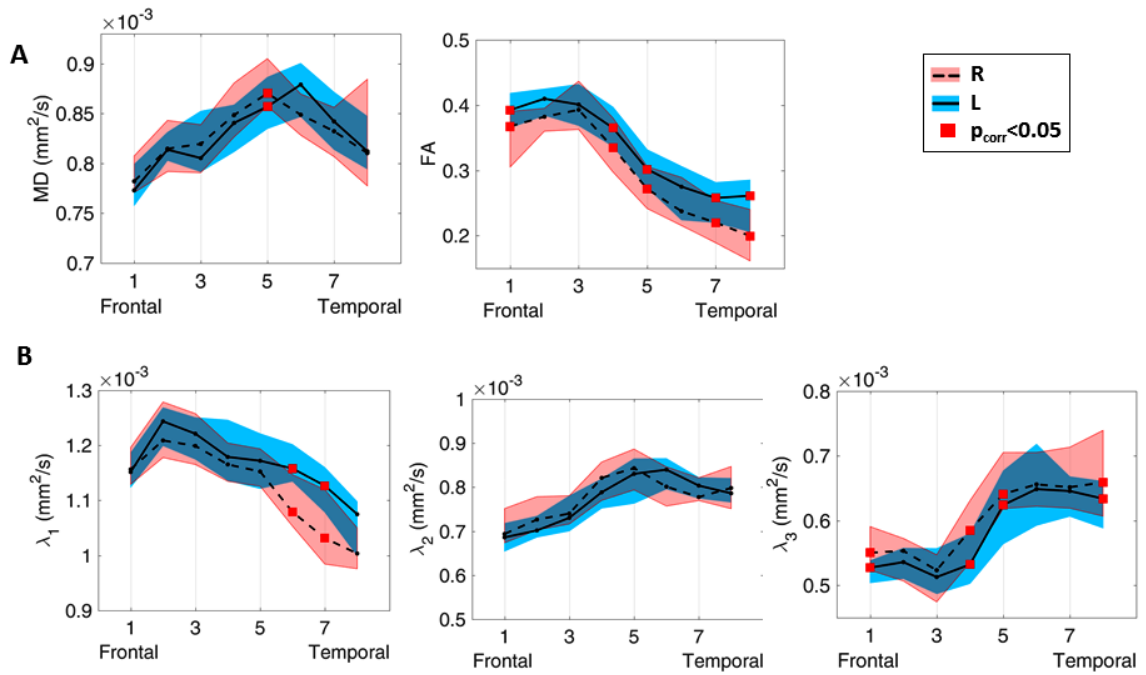


Figure 5.11: Along-UF DTI asymmetries.

Along-tract comparison between the right (dashed line) and left (continuous line) UF tractography results, evaluated with the CST-prob algorithm. Median DTI metrics are displayed along with the interquartile range (shaded area: red for the right, blue for the left). The red squares mark significant left-right differences with p -value < 0.05 after FDR correction.

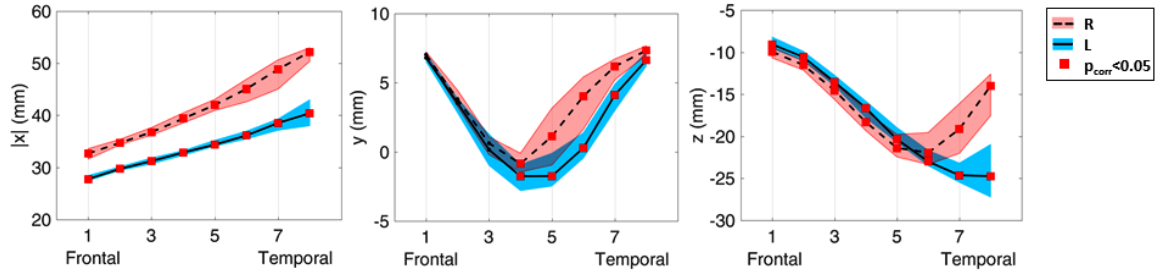


Figure 5.12: Asymmetries in UF curvature.

Centroid coordinates of along-UF segments were reported in the MNI-152 standard space. Right (dashed line) and left (continuous line) tractography results were compared. Median coordinate values were displayed along with the interquartile range (shaded area). The red squares marked significant left-right differences with p-value < 0.05 corrected with FDR for multiple comparisons.

CHAPTER 6

Tractography-driven cortical clustering - HCP dataset

Cortical brain regions can be characterised by common morphometric and connectivity properties (Eickhoff et al., 2018). In this work, I applied a connectivity-based cortical characterisation based on tractography results of healthy controls recruited in Human Connectome Project (HCP). Preliminary results of this study were presented at national Talozzi et al. (2019b) and international Talozzi et al. (2019a) congresses, and I was awarded by the Guarantors of Brain travelling grant to attend the 25th OHBM meeting, Rome 9-13/06/2019.

The aim of the study was the development of a novel method based on PCA of advanced diffusion tractography (Dell'Acqua et al., 2015) to define cortical regions that share a similar connectivity pattern within the left hemisphere. Nevertheless, PCA-based connectivity clustering was previously proposed to parcellate the occipital and frontal lobe in healthy controls by Thiebaut de Schotten et al. (2014, 2016).

MATERIAL AND METHODS

Pre-processed $b=2000s/mm^2$ diffusion MRI data of 50 right-handed males were obtained from the Human Connectome Project (HCP) S900 release, see Table 6.1 for the acquisition parameters. Tractography and DTI metrics were evaluated in [StarTrack](#) software: Euler tracking algorithm, 0.5 mm step size, 30° angle threshold and 0.2 FA threshold.

Whole brain tractograms were non-linearly registered to MNI space and concatenated into a group tractogram (n=50) using MegaTrack (Dell'Acqua et al., 2015). Subsequently, tractograms were filtered to select association streamlines running within the left hemisphere, excluding commissural and projection fibres (Figure 6.1 A).

[Freesurfer 5](#) software was run on the MNI-152 1mm brain and using a Matlab script I randomly parcelled the grey matter to form a fine parcelization of 0.3 cm^3 clusters (Figure 6.1 B). This analysis generated 1002 ROIs that were extended to the underlying white matter using a nearest neighbour algorithm (median ROI volume 0.5 cm^3).

Pairwise ROIs connectivity was evaluated, obtaining a 1002x1002 connectivity matrix whose weights were defined as:

$$w_{ij} = \frac{\text{n. of streamlines}}{Volume_{ROI_i} + Volume_{ROI_j}}$$

thresholded to include a minimum of 10% of subjects (Figure 6.1 C). The connectivity matrix was z-transformed and used for PCA analysis in [Orange3](#). PCA components were plotted according to matrix eigenvalues and fitted with a power law curve. PCA weights were normalised and associated to the cortical ROIs.

Table 6.1: Acquisition parameters DTI - HCP

Static field strength =	3 T
Scanner model =	Siemen Connectome Skyra
Sequence =	Spin-echo EPI
b-value =	2000 s/mm ²
Time of echo =	89.5 ms
Time of relaxation =	5520 s
Flip angle =	78°
Voxel dim =	1.25 x 1.25 x 1.25 mm ³
In-plane acquisition matrix =	168x144
n. of diffusion gradient directions =	90
n. of null b-valued =	6
<u>Release:</u> Human Connectome Project S900.	

Virtual dissection of tracts ending in selected cortical ROIs was performed using [trackvis](#).

RESULTS

The PCA eigenvalue plot shows at least 20 significant PCA components, even if there was no clear cut-off (Figure 6.2 A). The cortical hubs of the first five principal components (Figure 6.2 B) identified by the PCA weights (negative and positive) indicate regions that are connected by well known large association pathways (Figure 6.3) (Catani, 2017). Positive weights of PCA 1 define areas typically connected by the arcuate fasciculus, whereas the negative weights identify medial limbic areas connected by the dorsal and ventral cingulum. The medial limbic areas were also identified by positive weights in the PCA 2, PCA 3 and to less extent PCA 4. Other cortical regions included areas connected by shorter association pathways, such as the superior and middle posterior temporal regions connected by the vertical temporal tract (PCA 3, positive), the superior temporal and supramarginal

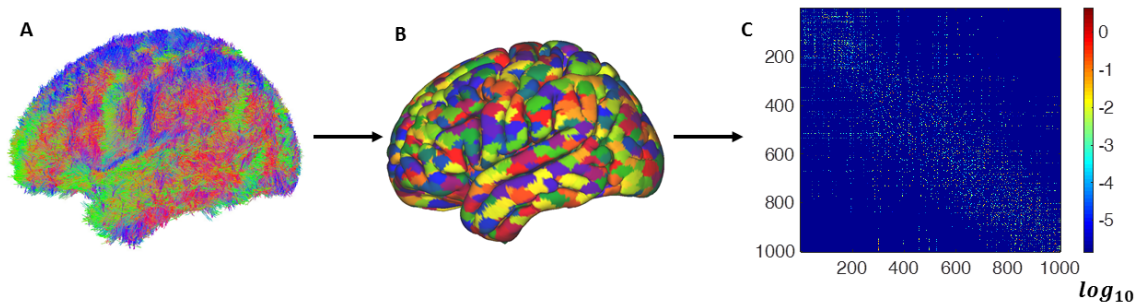


Figure 6.1: Structural connectome extraction for the HCP dataset.

Extraction scheme of the left hemisphere connectivity matrix. **Panel A:** group tractogram of 50 HCP volunteers, obtained selecting only association pathways. **Panel B:** random fine parcelization of MNI grey matter of 0.3 cm^3 (0.5 cm^3 including white matter) clusters, forming 1002 ROIs. **Panel C:** connectivity matrix representation (w_{ij}) thresholded to include at least the 10% of subjects.

gyrus connected by the posterior segment of the arcuate fasciculus (PCA 5, negative), the lateral occipital areas connected by the vertical occipital tract (PCA 5, positive) and the postcentral and inferior parietal lobule areas connected by the intralobar parietal fibers (PCA 4, positive).

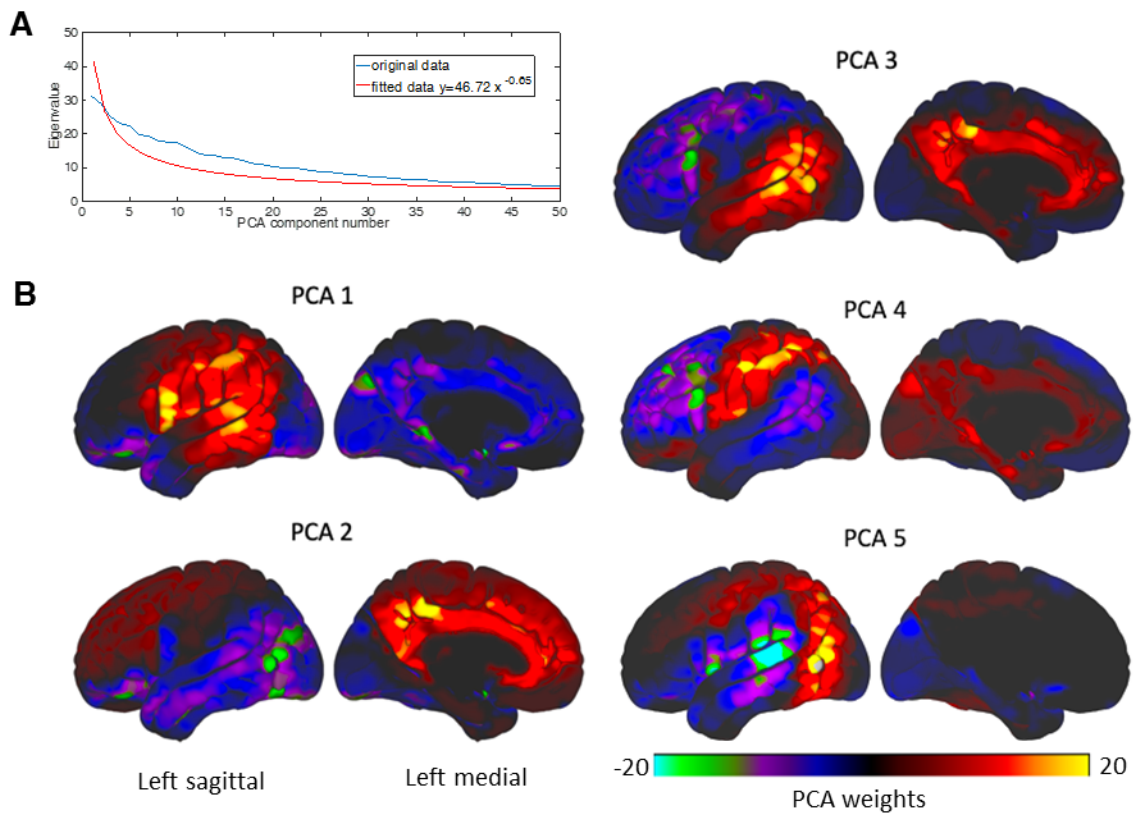


Figure 6.2: Cortical projections of connectome principal component.

Panel A: eigenvalues of the connectivity matrix covariance associated to PCA components (blue) and the corresponding power law-fitting curve (red). **Panel B:** left lateral and medial surface projections of PCA weights obtained from the first five PCA components: positive weights are associated to red-yellow color-coding, negative weights to blue-green. PCA 1 identifies positive perisylvian language areas on the lateral aspect and negative limbic projections in the medial aspect.

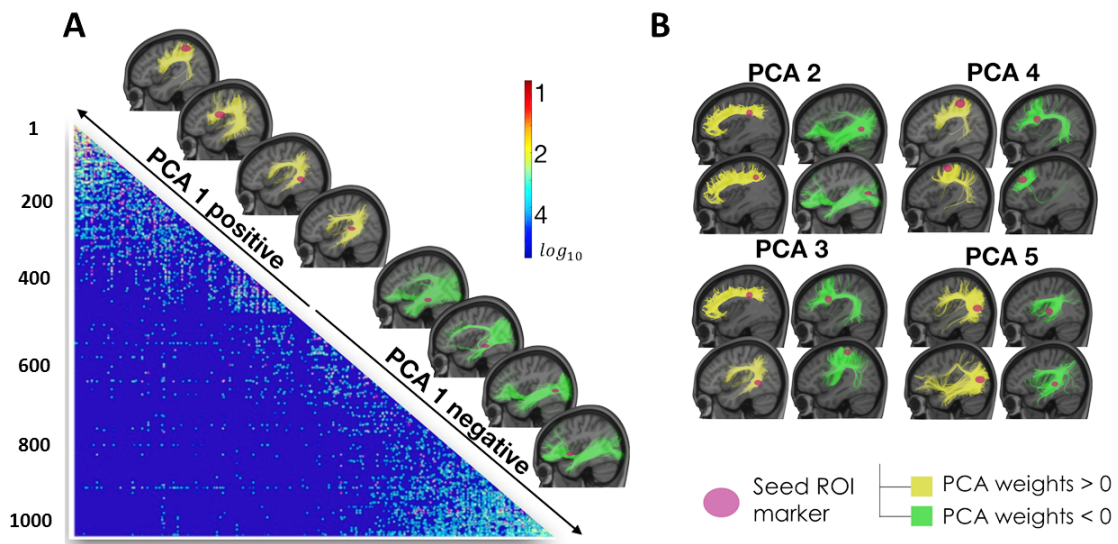


Figure 6.3: Principal components related to cortical seed tractography.

Streamlines ending in cortical ROIs localised with red circles. These ROIs are associated to the highest PCA positive values (in yellow) and to the lowest PCA negative values (in green). **Panel A:** connectivity matrix sorted with respect to positive and negative weights, associative white matter tracts terminating in/close to these respective cortical regions. **Panel B:** with respect to PCA 2,3,4 and 5 tracts that end in cortical ROIs associated to positive and negative PCA weights are shown.

CHAPTER 7

Discussion

7.1 LANGUAGE FUNCTION NEURODEGENERATION

The language network can be studied from different MRI modality prospective. Seeley et al. (2009) demonstrated that a direct link between intrinsic functional connectivity and grey matter structures is present, and in neurodegenerative diseases the corticotrophic fate can be defined by the synchronous baseline activity. Qi et al. (2019) studied developmental changes in language both evaluating cortical thickness measures and white matter connectivity of the arcuate fasciculus. They demonstrated the agreement of these two measures, but also the different findings in the description of the language network development.

In my PhD project, the differential diagnosis of AD and PPA was addressed evaluating cortical thickness measures, and in PPA patients longitudinal variations of DTI metrics in WM language tracts were evaluated.

Regarding cortical thickness measures, the results reported in Paragraph 2.1 showed a different pattern of cortical thickness reduction in AD and PPA compared to HC. These findings were in agreement with Ridgway et al. (2012), who explored pattern of reduced cortical thickness in early-onset variant of AD (n=25 Posterior Cortex Atrophy, n=15 lPPA, n=14 AD and n=30 HC), finding disease-specific reduction in each patient group compared to HC, and common areas of cortical thinning in the temporal-parietal regions. However, they supported the hypothesis that AD variants (including lPPA) have a phenotypic continuum spectrum of cortical thinning, rather than distinct subtypes.

In my analysis, comparing PPA and AD, significant results did not survive for multiple comparison corrections (Figure 2.2). Thus, I performed a multivariate approach, a discriminant function analysis (Paragraph 2.1), which showed good results in PPA and AD discrimination (86.1%).

These findings confirmed the results of Kim et al. (2019), who used discriminant function analysis combined with machine learning to classify a cohort of frontotemporal dementia patients (n=140 FTD, n=50 AD and n=146 HC). In this study the overall classification accuracy was 75.8%, and in particular the left frontal lobe discriminated non fluent PPA vs sPPA, and bilateral anterior temporal regions discriminated the sPPA variant.

Moreover, significant correlations (p-value ≤ 0.01) were measured between left temporal and para-hippocampal regions and performances in the *category world fluency test* (Paragraph 2.2), suggesting that cortical thickness can be used as an *in vivo* morphological biomarker for language neurodegeneration.

Rogalski et al. (2011) analysed cortical volume measures of 2-years follow-up PPA patients, recruited in the same centre of the PPA cohort analysed in Chapter 3. At the baseline, the cortical atrophy was localised in specific areas according to PPA clinical variants, whereas at 2-years follow-up the atrophy was widespread, involving the inferior frontal gyrus, the temporo-parietal junction and lateral temporal cortex in all clinical variants. Our DTI findings were in agreement with the diffuse language network degeneration in the 2-years follow-up previously measured with volumetric analysis (Rogalski et al., 2011). At baseline (Table 3.5), DTI metrics alterations with respect to controls had different patterns considering PPA clinical variants. On the contrary, at the follow-up DTI metrics alterations were coherent in all PPA variants and spread in all AF segments, especially in AF posterior, and in the UF (Table 3.6).

Regarding to significant differences in DTI measure, both at baseline and at follow-up, a decreased FA and increased MD and RD measures were measured in PPA with respect to HC, with the exception of FAT FA, which at baseline was signifi-

cantly higher in sPPA and lPPA with respect to controls (Table 3.5 and Figure A.3). The measured FAT FA values were comparable with the PPA study by Catani et al. (2013), and this increasing diffusion anisotropy could be a compensatory mechanism of contiguous WM degeneration.

The measured DTI longitudinal variations were in agreement with other PPA longitudinal studies (Tetzloff et al., 2017; Elahi et al., 2017) that investigated DTI metrics using an atlas based approach ([JHU atlas](#)) (Mori et al., 2005). In particular, we measured the most significant WM abnormalities, compared to controls, in DTI metrics (FA, MD and RD) of the AF posterior segment and UF in all the PPA variants (Table 3.6).

These tracts were also the ones that significantly correlated with language assessment scores. Respectively the AF posterior MD and RD measures correlated with the WAB-Rep scores at the baseline, whereas the UF DTI metrics correlated at the baseline with the PPVT and BNT scores, and at the follow-up with PPVT and PPT scores (Table 3.8).

No correlations were found for the WAB-AQ, since it is a general measure of aphasia severity and to evaluate the language functions more specific assessments are required. The WAB score in repetition of sentence was evaluated showing significant correlations.

Interestingly, we found a significant correlation between the PPT longitudinal variation correlated and UF MD measure, suggesting that semantic association of images is a language dysfunction presenting later in PPA (Table 3.4 and Figure A.2), and probably due to a disconnection syndrome of the UF. In particular, the UF DTI metrics were significantly different only in the follow-up and considering the variation of UF Δ FA, in sPPA with respect to aPPA and lPPA (Table A.2 and Figure

A.4).

Clinical studies suggest that sPPA can have a disease progression with a closer association with bvFTD (Rosen et al., 2006), whereas aPPA can be associated with corticobasal degeneration (Kertesz et al., 2000). In addition, from a neuropathologic prospective, the 60–70 % of PPA patients who show brain alterations consistent with frontotemporal lobar degeneration, characterised by tauopathy, microtubule associated protein in neurofilaments and glial filaments, or TDP-43 proteinopathy (TAR DNA-binding protein 43 encoded by TARDBP), present in neurons. Tau pathology is usually observed in aPPA, whereas sPPA is more often connected with TDP-43 accumulation; whereas bvFTD can present both pathology phenotype. On the contrary the 30–40 % of PPA patients present AD pathology, especially lPPA (Rogalski & Mesulam, 2009; Staffaroni et al., 2019).

These neuropathologic differences across PPA variants, cause specific microstructures alterations, and thus influence DTI measures. This could be both a confounding aspect in PPA group analysis or a specific characterisation of PPA clinical variants.

An atlas based approach was used for DTI analyses to ensure an automatic and standardised procedure, longitudinally both in patients and controls. The adopted ANTs registration software (Paragraph 3.2) allowed an optimal WM tract ROI registration to the single subject anatomy. The ANTs volume-based registration approach provided good scan-rescan repeatability (Avants et al., 2011) for cortical thickness measurements, and even higher predictive performance of age and gender in comparison to the most widely used Freesurfer surface-based software (Tustison et al., 2014).

More recently, in the longitudinal PPA study by Tetzloff et al. (2017), the annualised

rate of atrophy progression was evaluated whole-brain by using the annualised log Jacobian values computed from each ANTs deformation field.

However, a possible drawback would be a partial volume effect due to the adopted atlas ROI approach. Thus, future outlines will be the evaluation of specific tract atrophy by computing tractography analysis for each participant, and evaluating along-tract measure such as volume, or also evaluating bilaterally atrophy progression by new explorative approaches (Tetzloff et al., 2017). Even if tract volume is highly dependent on the adopted tractography algorithm (Talozzi et al., 2018c), it has been shown that the number of streamlines in the uncinatus fasciculus correlated with BNT performance in PPA (Catani & de Schotten, 2012).

In the current study, only DTI metrics were evaluated, as a first investigation of the neurodegeneration progression in PPA. However, it must be specified that even if widely used and sensitive to microstructural alterations, they lack in specificity for the underlying pathological substrate. DTI limitations are due to metrics dependency on fibre configurations and free water contamination. To overcome these issues, multi-compartment models has been proposed, such as the Neurite Orientation Dispersion and Density Imaging (NODDI) (Zhang et al., 2012). In particular, the neurite density estimation requires an optimised two-shell protocol, nowadays possible also in clinical settings (e.g. on multiple sclerosis patients (Spanò et al., 2018)). To date, NODDI has not been apply to PPA investigation, whereas it has for other neurodegenerative disease (Huntington, Alzheimer and young Alzheimer onset) (Zhang, 2019). Additionally to NODDI, other diffusion metrics are possible, Mito et al. (2018) investigated tract specific analysis evaluating intra-axonal fibre distribution (density, cross-section area) to assess neurodegenerative WM distribution in AD (n=49), mild cognitive impairment (n=33) and HC (n=95).

It must be specified that my analyses were performed retrospectively on different dataset and for future perspectives, a unified investigation of cortical thickness and white matter structures should be preferred. Moreover, the analysed DTI data were acquired with a single-shell protocol (Paragraph 3.3) not suitable for neurite density estimation.

7.2 LANGUAGE RECOVERY AFTER STROKE: MR BIOMARKERS

Stroke lesion-symptom mapping related to aphasia has been previously investigated using MRI. Bates et al. (2003) proposed as first the voxel-based lesion-symptoms mapping (VLSM) approach, demonstrating in a large cohort of patients (n=101) that the insula and deep parietal white matter most correlated with language fluency, whereas the middle temporal gyrus with auditory comprehension. Fridriksson et al. (2016) using the VLSM approach for left-hemisphere stroke patients (n=165) discriminated a dorso-parietal stream related to motor-phonological dysfunctions, and a ventral temporal-frontal stream, which is correlated to lexical-semantic speech functions. Findings were also confirmed by a developed connectome lesion symptom mapping in the left hemisphere (Fridriksson et al., 2018).

The study of patient with stroke "*Offer a unique window into understanding human brain function*" (Forkel & Catani, 2018), in particular language.

Moreover, Forkel et al. (2014) by a bilateral reconstruction of the arcuate fasciculus in left-hemisphere stroke patients (n=16), designed a hierarchical model identifying in the right hemisphere the arcuate volume and age as predictors of aphasia recovery, whereas lesion size only as predictor in the left hemisphere.

In my study, CBF of stroke patients was bilaterally investigated (Chapter 4). In

particular, I quantified perfusion in the different vascular cerebral artery territories (anterior, middle and posterior) and in Broca's areas (Brodmann area 44 and 45). First, CBF was studied in a group of healthy controls, measuring a significant correlation between CBF ROI quantification with participant age (Table 4.6). On the contrary, this correlation was not present using CBF laterality index (LI) (Equation 4.1), which evaluates perfusion asymmetry in homologous ROIs. This suggested the LI as a normalised measure within subjects, taking into account CBF variability factors.

Stroke patients' age was not considered in this analysis, since there was not a clear dependence with CBF values. In fact, other factors could influence perfusion variability in the evaluated patient group: the different ethnicity, medical treatments (e.g. tissue-type plasminogen activator) (Table 4.1), and stroke lesion size.

In the evaluation of possible correlations between CBF measures and aphasia severity significant correlations were found only for the LI of the middle cerebral artery. This result confirms the LI as a useful metric and also highlights the main role of the middle cerebral artery territory in aphasia symptoms.

In particular, the significant correlations suggested that the LI, evaluated at 6-months follow-up, correlates with language recovery, where an increased perfusion asymmetry towards the right hemisphere corresponds to an higher recovery quantified with the WAB-R AQ (Table 4.7 and Figure 4.11). In addition, MCA LI at follow-up significantly correlated with AQ at baseline, showing an agreement between aphasia severity in acute and MCA perfusion reorganisation, shifting towards the right hemisphere.

Moreover, this MCA perfusion reorganisation was also described by the a significant correlation, at the baseline, between MCA LI and MRI timing post stroke

onset (Figure 4.10). Additionally, at the follow-up the MCA LI significantly correlate with patient education, indicating a possible cognitive reserve mechanism involving the right hemisphere for language.

As underlined in the recent review by Kiran & Thompson (2019), during clinical assessment the impact of neuroplasticity of language network can be addressed with vascular physiology analysis to monitor perfusion changes, detectable also in chronic phase. In fact, using ASL Thompson et al. (2017) measured an increased CBF on the right hemisphere with respect to controls in chronic stroke patients (n=35), but in the absence of correlations with language scores. In this study only the hypoperfusion of perilesional tissue correlated to language impairment (Thompson et al., 2017).

In agreement, Robson et al. (2017) evaluating CBF in the Wernicke's area, in patients with chronic Wernicke's aphasia (n=12), showed that the hypoperfusion surrounding stroke structural lesion, correlated with language scores, suggesting that post-stroke impairments are related to a wider neuronal disruption with respect to the observable T1w lesion.

Recruitment of right language areas for stroke recovery was also measured by Saur et al. (2006) using task-based fMRI. Administering an auditory comprehension task, they longitudinally studied stroke patients (n=14) and matched healthy controls (n=14). In the acute phase (1.8 days after stroke on average) only a limited early activation of non-infarcted left language areas was measured, whereas in the sub-acute phase (12.1 days) a large activation of right language homologous areas, right Broca and supplementary motor area, was observed, showing a strong correlation with language improvement. Afterwards, in the chronic phase (321 days, almost 10 months) they measured a re-shift of activation on the left in correlation

with language improvement.

Thus, it seems that chronic perfusion changes play a key role in neuronal plasticity and ASL can open new perspective in stroke lesion analysis.

However, this observation has to be confirmed by lesion definition and comparison with DTI measures, as future study investigation. Future outlines of the proposed stroke study will be the automatic segmentation of stroke lesion.

In particular, I am currently exploring the approach proposed by Seghier et al. (2008), which by an iterative clustering procedure defines an atypical tissue class, in grey and white matter, to segment brain lesions with different size, locations, and textures. In fact, in particular in chronic phase, stroke lesions may have different characteristics and it is challenging to apply an automatic and unified lesion detection strategy.

7.3 ALONG-TRACT ANALYSIS AND TRACTOGRAPHY DRIVEN CORTICAL MAPPING IN HEALTHY CONTROLS

At the Functional MR unit of the Department of Biomedical and Neuromotor Sciences, Bologna, we evaluated first along-tract analysis in the cortical spinal tract (Testa et al., 2017). Afterwards, evaluating the arcuate fasciculus several issues occurred, in fact, considering that the AF is a curving bundle and tract modelling along anatomical axes was not optimal (Huang et al., 2012). Thus, the necessity of developing a new along-tract algorithm. Revising the literature, several methods were proposed (O'Donnell et al., 2009; Colby et al., 2012; Yeatman et al., 2012), but all for them required as input streamlines file (e.g. *.trk*). However, at first I was interested in analysing probabilistic tractography (Probtrackx2, Paragraph

5.1) (Talozzi, 2016; Talozzi et al., 2016a), whose output is connectivity probability maps. Thus, I tried to develop an algorithm suitable for volume rendering, and suitable for all types of tractography methods (Talozzi et al., 2018c).

The Laplacian operator, Ψ , is commonly used in graph theory to evaluate clustering properties (Andreotti et al., 2018), but also spectral mesh processing (Zhang et al., 2010) and imaging applications (Chung et al., 2011; Kim et al., 2014). In my PhD project, it was successfully applied for along-tract analysis with different tractography algorithms (probtrackx2, CSTdet and CSTprob) and bilaterally for the AF and UF (Paragraph 5.3).

One of the still open question in tractography is "*Which algorithm should I use? Which is the best?*" (Maier-Hein et al., 2017), no answer yet, but it has been shown that different tractography methods lead to different results (Bain et al., 2019): deterministic methods can lead to false negative fibre reconstruction, whereas probabilistic to false positive.

Focusing on the right AF, tractography really depend on the chosen tractography method, probably due to crossing fibres (Chen et al., 2015b). Thus, I applied high order tractography models for bilater AF reconstruction: the ball and sticks (Behrens et al., 2007) and constrained spherical deconvolution (Tournier et al., 2010).

In a sizeable sample of healthy subjects (n=29) I was able to tract the AF in both hemispheres, with the exception of one case, on the right using the deterministic method (CSTdet). These results are in agreement with *post mortem* AF dissection findings (Martino et al., 2013), and previous *in vivo* tractography studies using Probtrackx (Chen et al., 2015b) or CSTprob (Mormina et al., 2015).

Moreover, analysing hemispheric asymmetries, a greater superior temporal gyrus

connectivity was found on the left (Figures 5.2 and 5.3). This result was previously observed in the study of Glasser & Rilling (2008), proposing a two-segment model of the AF with respect to projections towards the middle and superior temporal gyri. In this model, the superior temporal gyrus is thought to be involved in the auditory interface for language, whereas the middle temporal gyrus, in particular its posterior portion, is connected to visual input and is a sound-meaning interface for lexical-semantic functions (Hickok & Poeppel, 2004). Our results were consistent with the proposed two-segment model (Glasser & Rilling, 2008), and with Geschwind & Levitsky (1968), who analysing 100 *post mortem* human brains found that there was a larger superior temporal gyrus area on the left.

Moreover, with respect to the frontal lobe AF connectivity, the precentral operculum has found to have a primary importance during early language acquisition and integration of auditory-motor stimuli (Friederici, 2011; Bernal & Ardila, 2009), while the inferior frontal gyrus connections arise much later in human brain development and are functionally related to semantic and syntactic language processing (Hickok & Poeppel, 2004). Evaluating the AF connectivity asymmetries, I found a greater precentral operculum connectivity on the left (Figure 5.2 and 5.3), consistent with leftwards language dominance.

Moreover, the hemispheric along-AF asymmetries has been discussed in article (Talozzi et al., 2018c), recently published during my PhD course and reported in Appendix B. In particular, the AF curvature mapping supported the different bilateral AF cortical projection asymmetries. A greater AF volume on the left was measured only with the Probtrackx2 tractography method, and a greater FA on the right with the CSTprob (Table 5.3). Thus, these findings did not show a clear left lateralisation in volume and DTI metrics (Catani et al., 2007). Moreover, as sug-

gested by Bain et al. (2019) and discussed in my study's limitation (Talozzi et al., 2018c), these findings need to be confirmed by future applications in a larger group and improving DTI acquisition parameters.

With respect to the UF connectivity, as concluded in the review by Von Der Heide et al. (2013) possible UF hemispheric differences remained an open question. Thus, it is interesting to investigate asymmetries which could be related to functional specialisation.

In my PhD project, I was able to bilaterally reconstruct the UF using an automatic procedure and a probabilistic tractography method, CSTprob (Tournier et al., 2010). Moreover, using the developed Laplacian along-tract algorithm (Paragraph 5.3) it was possible to investigate along-UF DTI metrics, segment volumes and tract curvature. In particular, volume UF asymmetries were found only along-tract, with a right volume greater with respect to left in medial segments, whereas a left lateralisation in temporal segments (Figure 5.8).

Bilaterally the FA profile was higher in UF frontal segments, since in the region under the sub-insular structures, the UF fibres are highly packed (Rodrigo et al., 2007; Yeatman et al., 2012). In addition, we measured an FA value greater on the left at whole tract level (p -value=0.04) (Table 5.4), also confirmed along-tract (Figure 5.11). In literature, there is not a consensus about UF FA asymmetries (Rodrigo et al., 2007; Highley et al., 2002), our findings support the hypothesis of a stronger route in the left hemisphere, often dominant in language processing.

The UF curvature was significantly different between the hemispheres (Figure 5.12), and this asymmetry reflects different cortical projections (Figure 5.5): the UF terminations were more dorsal in the frontal left hemisphere, whereas the right UF curved more sharply towards a more superior and anterior portion of the an-

terior temporal lobe.

A two-component model for the left UF has been previously described both *in-vivo* (Catani et al., 2002) and *ex-vivo* (Kier et al., 2004), identifying a ventral and a dorsal component. In our bilateral UF evaluation we found that the dorsal component towards the frontal lobe was most present on the left, in agreement with Hau et al. (2017).

One limitation of the proposed along-tract analysis of the AF and UF are the DTI acquisition parameters (Paragraph 5.2): the intensity of the static magnetic field (1.5 T), the non-isotropic DTI voxel and the relatively low b-value. Spherical deconvolution has been shown to have optimal results at high b-values (e.g. 3000 s/mm^2), even if there is the signal to noise attenuation (Tournier et al., 2004). However, the adopted non-negativity constrained super-resolved spherical deconvolution (Paragraph 5.1) can be apply to relatively low b-values ($\sim 1000s/mm^2$) (Tournier et al., 2007). In particular, in our study negative regions in the FOD were not considered, since physically impossible and due to the noise presence, and the FOD angular resolution was super-resolved by the estimation of more FOD parameters than the actually measured (Tournier et al., 2007).

WM routes are likely related to cortical projections, and as discussed for PPA (Paragraph 7.1), both cortical and WM structures underlying language functions. To better investigate the interaction between grey and white matter organisation, I performed a study in a group of HC, focusing on the left hemisphere, dominant for language processing.

For this purpose, DTI data from the HCP dataset of young healthy right-handed males (n=50) were evaluated. HCP acquisitions were performed using the Connectome scanner, which can achieve imaging resolution and data quality higher

than conventional clinical scanner (Table 6.1).

Moreover, I analysed tractography data using a new group approach, MegaTrack (Dell'Acqua et al., 2015), which allows to merge white matter fibres reconstructed from different subjects.

These methodologies and a mathematical, bio-informatics approach, using PCA for tractography clustering, allowed the identification of brain areas shown to be involved in language processing (Parker et al., 2005): pars opercularis, middle and superior temporal gyri and supramarginal gyrus (PCA 1, Figure 6.2). The same regions has been previously identified using other atlasing techniques: histology-based cytoarchitecture evaluation or MRI-based myelin content measures (Eickhoff et al., 2018).

Thus, the proposed PCA analysis offers a valid approach to discriminate left hemisphere cortical areas sharing a similar connectivity pattern and suggests that clusters within the same PCA are mutually interlinked by well known association pathways.

These findings are in agreement with Fan et al. (2016), who proposed a cortical atlas based on probabilistic tractography clustering.

Interestingly, Thiebaut de Schotten et al. (2014) compared PCA tractography-based parcellation with resting state functional networks for the occipital lobe, showing a poor overlap between the two clusterization approaches. Moreover, they showed that fMRI results neither respect the myelo and cytoarchitectonic boundaries of *post-mortem* studies. Thus, there is a not clear agreement between different multi-modal clustering approach.

In our study, PCA 1 identified eloquent areas within the left hemisphere. However, this should be proved both using resting state fMRI connectivity or task-based

paradigms (Black et al., 2017).

These results need to be confirmed after anatomical vetting of the produced trac-tograms before the approach can be reliably applied to larger dataset to reveal characteristic patterns of left-right organisation, or to study differences between sexes and changes across the lifespan.

APPENDIX A

Language assessment and DTI metrics across PPA variants

Language assessment differences across PPA clinical variants

The Kruskal-Wallis test ([SPSS v25](#)) was used to evaluate differences in language assessment scores (Paragraph 3.1), across PPA variants at baseline, at follow-up and evaluating the Δ of variation (Paragraph 3.3 and Equation 3.1).

Significant group differences were found for all the language tests, at baseline and at follow-up, with the exception of the WAB-AQ score (Table A.1). Only for the PPVT and PPT tests, the longitudinal variation rate was significantly different across PPA variants.

Significant *post-hoc* comparisons, correcting for Bonferroni across groups, were found between: sPPA vs aPPA and sPPA vs IPPA (Table A.1).

Corresponding boxplots are reported: in Figure A.1 for the WAB-Rep and BNT tests, and in Figure A.2 for the PPVT and PPT tests.

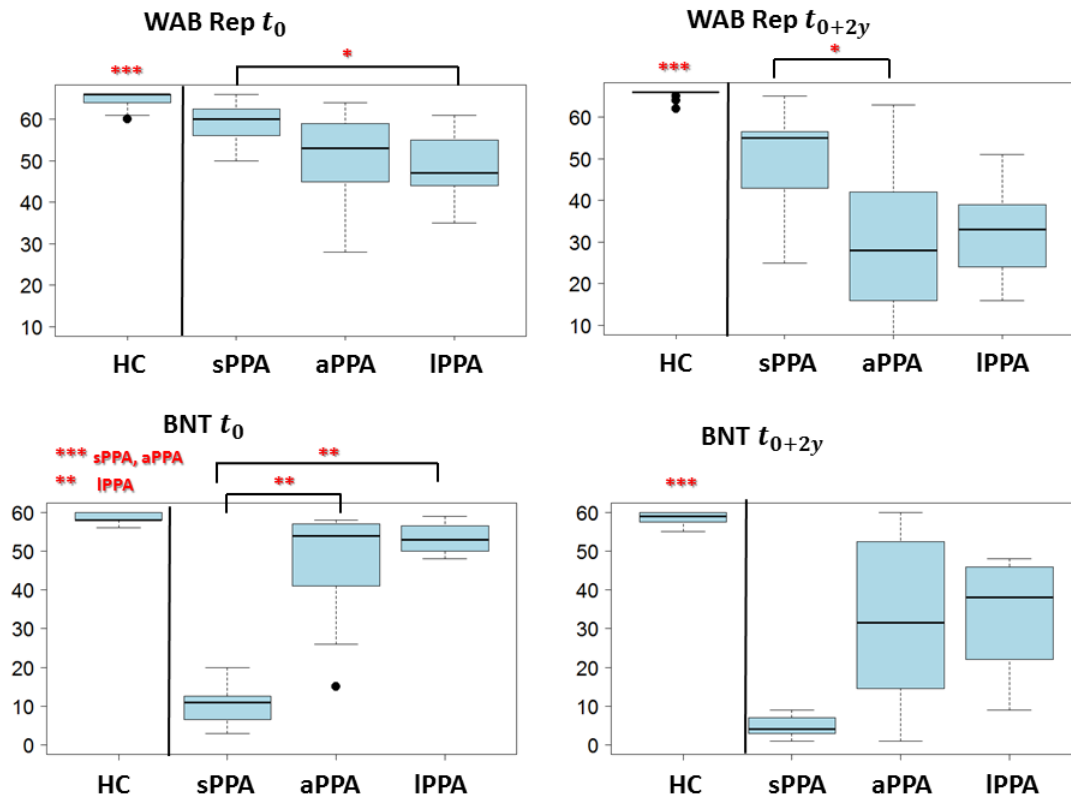


Figure A.1: Boxplots of significantly different WAB Rep and BNT scores across PPA variants at baseline (t_0) and at follow-up (t_{0+2y}). Corresponding p-value are signed with asterisks: * < 0.05 , ** < 0.01 , *** < 0.001 . The vertical line indicates that HC significantly different with indicated p-value to all PPA groups.

HC=Healthy Controls, PPA=Primary Progressive Aphasia, sPPA= semantic PPA, aPPA= agrammatic PPA, IPPA= logopenic PPA, WAB=Western Aphasia Battery, BNT=Boston Naming Test.

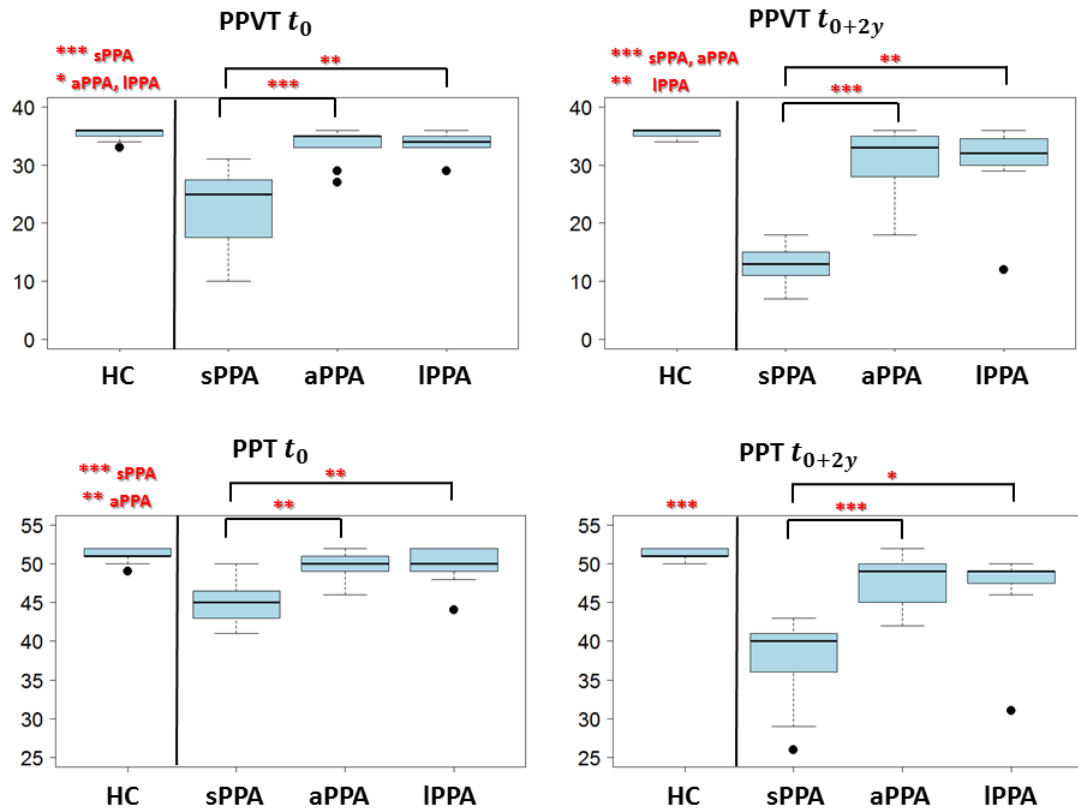


Figure A.2: Boxplots of PPVT and PVT scores for HC and PPA variants at baseline (t_0) and at follow-up (t_{0+2y}). Corresponding p-value are signed with asterisks: * < 0.05 , ** < 0.01 , *** < 0.001 . The vertical line, when reported, indicates that HC significantly different to all PPA groups.

HC=Healthy Controls, PPA=Primary Progressive Aphasia, sPPA= semantic PPA, aPPA= agrammatic PPA, IPPA= logopenic PPA, WAB=Western Aphasia Battery, PPVT=Peabody Picture Vocabulary Test, PPT=Pyramids and Palm Trees.

Table A.1: Kruskal-Wallis test significant differences for language assessment across PPA clinical variants.

	Difference across PPA variants		
	sPPA vs aPPA	sPPA vs IPPA	
WAB-Rep t_0	*		*
WAB-Rep t_{0+2y}	*	*	
PPVT t_0	***	***	**
PPVT t_{0+2y}	***	***	**
Δ PPVT	***		
BNT t_0	***	**	**
BNT t_{0+2y}	**		
PPT t_0	**	**	**
PPT t_{0+2y}	***	***	*
Δ PPT	**		

Only significant results are shown: at the baseline t_0 , at 2-years follow-up $t_0 + 2y$ and evaluating the longitudinal variation rate Δ (Equation 3.1). The reported asterisks correspond to p-values: * < 0.05, ** < 0.01, *** < 0.001.

PPA=Primary Progressive Aphasia, sPPA= semantic PPA, aPPA= agrammatic PPA, IPPA= logopenic PPA, WAB=Western Aphasia Battery, PPVT=Peabody Picture Vocabulary Test, BNT=Boston Naming Test.

DTI metric differences across PPA clinical variants

The Kruskal-Wallis test ([SPSS v25](#)) was used to evaluate DTI measure differences in language tracts (Paragraph 3.2), across PPA variants, at baseline, at follow-up and evaluating the Δ of variation (Paragraph 3.3 and Equation 3.2).

Significant group differences are reported in Table A.2. At the follow up and evaluating the longitudinal variation rate, only the UF was significantly different across clinical variants.

Significant *post-hoc* comparisons, correcting for Bonferroni across groups, were found between: sPPA vs aPPA and sPPA vs IPPA (Table A.2). Boxplots, corresponding to significant differences, are reported at baseline for the AF anterior, FAT and ILF (Figure A.3), and at the UF follow-up and longitudinal variation (Fig-

ure A.4).

Table A.2: Kruskal-Wallis test significant differences for language tract DTI measures (FA, MD, RD) across PPA clinical.

	Difference across PPA variants	sPPA vs aPPA	sPPA vs IPPA
AF MD t_0 (mm^2/s)	*	*	
FAT FA t_0	*	*	
ILF MD t_0 (mm^2/s)	*		*
UF FA t_0	*		
UF MD t_0 (mm^2/s)	*		
UF RD t_0 (mm^2/s)	*		
UF FA t_{0+2y}	**	**	*
UF MD t_{0+2y} (mm^2/s)	*	*	*
UF RD t_{0+2y} (mm^2/s)	**	*	*
Δ UF FA	*	*	*
Δ UF RD	*		

Only significant results are shown: at baseline t_0 , at 2-years follow-up $t_0 + 2y$ and evaluating the longitudinal variation rate Δ (Equation 3.2). The reported asterisks correspond to p-values: * < 0.05, ** < 0.01, *** < 0.001.

FA=Fractional anisotropy, MD=Mean Diffusivity, RD=Radial Diffusivity, PPA=Primary Progressive Aphasia, sPPA=semantic PPA, aPPA=agrammatic PPA, IPPA=logopenic PPA, AF=Arcuate Fasciculus, FAT=Frontal Aslant Tract, ILF=Inferior Longitudinal Fasciculus, UF=Uncinate Fasciculus.

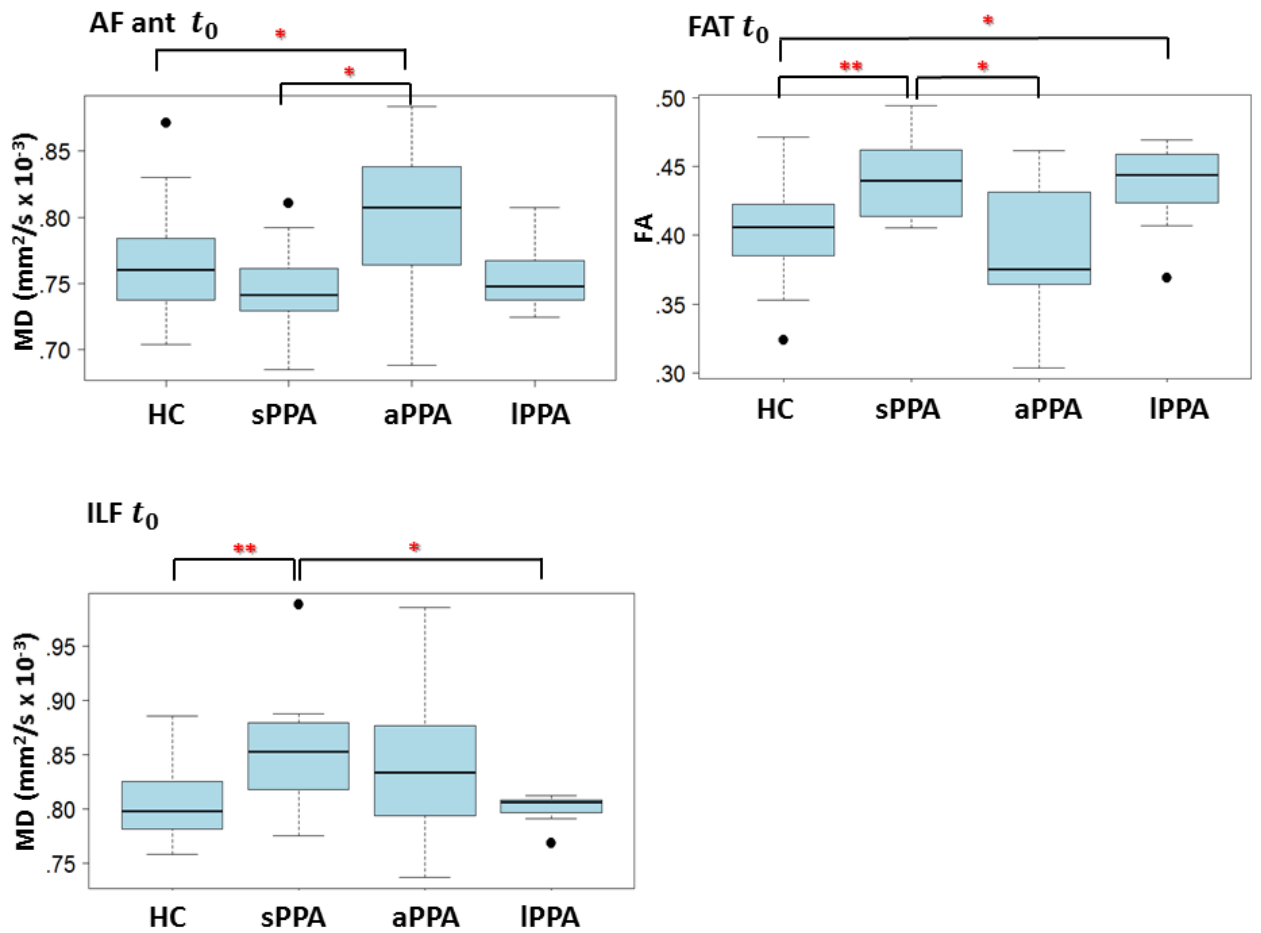


Figure A.3: Boxplots of significantly different DTI metrics across PPA variants at baseline, t_0 . Corresponding p-values are signed with asterisks: * < 0.05, ** < 0.01, *** < 0.001.

FA=Fractional anisotropy, MD=Mean Diffusivity, HC=Healthy Controls, PPA=Primary Progressive Aphasia, sPPA= semantic PPA, aPPA= agrammatic PPA, IPPA= logopenic PPA, AF ant=Arcuate Fasciculus Anterior segment, FAT=Frontal Aslant Tract, ILF=Inferior Longitudinal Fasciculus.

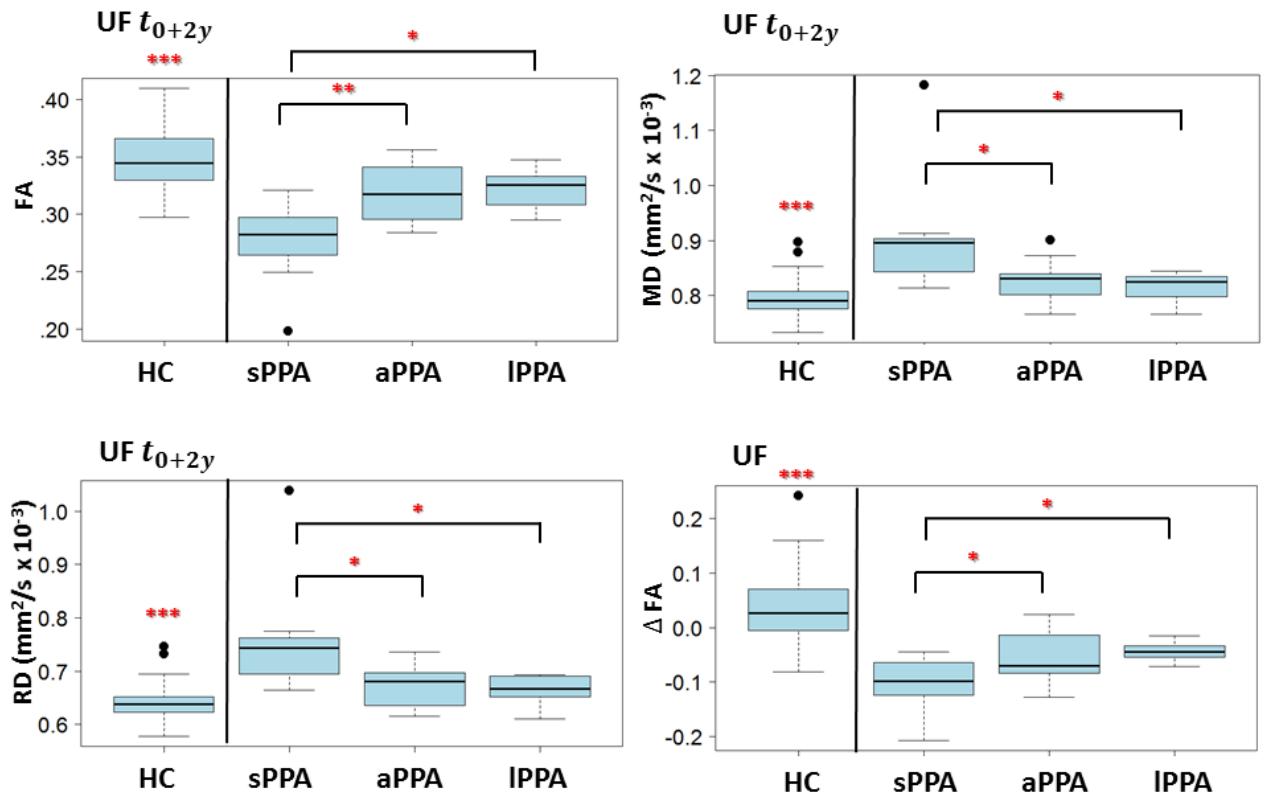


Figure A.4: Boxplots of significantly different DTI metrics across PPA variants at baseline, follow-up t_{0+2y} and longitudinal variation rate Δ , are reported. Corresponding p-value are signed with asterisks: * < 0.05, ** < 0.01. The vertical line indicates that HC significantly different with p-value < 0.001 with all the PPA variants

FA=Fractional anisotropy, MD=Mean Diffusivity, RD=Radial Diffusivity, HC=Healthy Controls, PPA=Primary Progressive Aphasia, sPPA= semantic PPA, aPPA= agrammatic PPA, IPPA= logopenic PPA, UF=Uncinate Fasciculus.

APPENDIX B

**Along-tract analysis of the arcuate fasciculus using the Laplacian operator to
evaluate different tractography methods**



Original contribution

Along-tract analysis of the arcuate fasciculus using the Laplacian operator to evaluate different tractography methods

Lia Talozzi^{a,1}, Claudia Testa^{a,1}, Stefania Evangelisti^a, Lorenzo Cirignotta^a, Claudio Bianchini^a, Stefano Ratti^b, Paola Fantazzini^c, Caterina Tonon^{a,d,*}, David Neil Manners^a, Raffaele Lodi^{a,d}

^a Department of Biomedical and NeuroMotor Sciences, Functional MR Unit, University of Bologna, Bologna, Italia

^b Department of Biomedical and NeuroMotor Sciences, Cellular Signalling Laboratory, University of Bologna, Bologna, Italia

^c Department of Physics and Astronomy, University of Bologna, Bologna, Italy, and Centro Enrico Fermi, Roma, Italia

^d IRCCS Istituto delle Scienze Neurologiche di Bologna, Diagnostica Funzionale Neuroradiologica, Bologna, Italia

ARTICLE INFO

Keywords:

Arcuate fasciculus
Laplacian
Tract curvature
Constrained spherical deconvolution
Ball-and-sticks model
Hemispheric asymmetries

ABSTRACT

Purpose: We propose a new along-tract algorithm to compare different tractography algorithms in tract curvature mapping and along-tract analysis of the arcuate fasciculus (AF). In particular, we quantified along-tract diffusion parameters and AF spatial distribution evaluating hemispheric asymmetries in a group of healthy subjects.

Methods: The AF was bilaterally reconstructed in a group of 29 healthy subjects using the probabilistic ball-and-sticks model, and both deterministic and probabilistic constrained spherical deconvolution. We chose cortical ROIs as tractography targets and the developed along-tract algorithm used the Laplacian operator to parameterize the volume of the tract, allowing along-tract analysis and tract curvature mapping independent of the tractography algorithm used.

Results: The Laplacian parameterization successfully described the tract geometry underlying hemispheric asymmetries in the AF curvature. Using the probabilistic tractography methods, we found more tracts branching towards cortical terminations in the left hemisphere. This influenced the left AF curvature and its diffusion parameters, which were significantly different with respect to the right. In particular, we detected projections towards the middle temporal and inferior frontal gyri bilaterally, and towards the superior temporal and precentral gyri in the left hemisphere, with a significantly increased volume and connectivity.

Conclusions: The approach we propose is useful to evaluate brain asymmetries, assessing the volume, the diffusion properties and the quantitative spatial localization of the AF.

1. Introduction

The arcuate fasciculus (AF) is an associative white matter (WM) tract involved in language functions. The AF was classically considered to connect two areas: the Broca expressive language area (inferior part of the precentral gyrus and posterior part of the middle and inferior frontal gyri), and the Wernicke language receptive area (posterior part of the superior and middle temporal gyri). Based on seminal post-mortem studies in healthy subjects and in patients with language disorders such as conduction aphasia [1,2], language processing was assigned mainly to the left hemisphere. Nowadays, the language network can be studied by *in vivo* noninvasive methods, such as tractography

[2–5] and fMRI [6]. Left hemispheric dominance for language functions, especially those supporting syntactic processes, has been confirmed in fMRI studies, but semantic and phonemic processes are now known to be less left-lateralized, while prosodic information is processed in the right hemisphere [6–9].

Tractography uses Diffusion Weighted (DW) MR images to reconstruct the pathways of WM fibres [10,11]. Catani et al. [3] studied the AF connectivity by deterministic tensor tractography [12] and found that in most subjects the right AF could not be tracked [4]. Subsequent studies have demonstrated a significant variability in the detection of AF [13,14] or other WM tracts [15] depending on the tractography algorithm employed.

* Corresponding author at: Department of Biomedical and NeuroMotor Sciences, Functional MR Unit, University of Bologna; Istituto delle Scienze Neurologiche di Bologna, Diagnostica Funzionale Neuroradiologica, Bologna, Italia.

E-mail address: caterina.tonon@unibo.it (C. Tonon).

¹ Contributed equally.

Chen et al. [14] were able to detect the AF in both the hemispheres with the probabilistic ball-and-sticks tractography [13], but not with deterministic tensor based tractography. This could be related to the proportionally greater presence of crossing fibres in the right hemisphere [16,17]. Additional information on WM tracts may be gleaned from tractography by performing an along-tract analysis for quantitative investigation of local diffusion parameters. Tract variation may be studied along a preferential anatomical axis [18], but this approach is inadequate in the case of AF curving fibres trajectories that arch around the Sylvian fissure and project laterally towards grey matter (GM) terminations. Several methods for AF along-tract parameterization have been proposed, commonly based on streamline parameterization [16,19,20], and hence inapplicable to connectivity maps. However, the AF can be studied by dividing it in two segments, a more anterior horizontal and a more posterior vertical one, while also evaluating their curvature in this sub-segmental division [21–23].

The question of which GM areas are connected by the AF remains open [24], given limitations in fibre tracking and great inter-subject variability. The study of the distribution of GM terminations of the AF is of considerable interest in the monitoring of language development in the human brain [25,26] or in comparative studies on primates [27].

The aim of this study was to compare different tractography methods using an along-tract parameterization to quantitatively evaluate arcuate fasciculus asymmetries across hemispheres, to assess possible volumetric, geometric and diffusion metrics asymmetries. We estimated AF connectivity in the right and left hemispheres of a group of 29 healthy subjects using three different methods, all achieving a good crossing-fibre resolution. We performed AF tractography by the probabilistic ball-and-sticks, deterministic and probabilistic spherical deconvolution tractography methods, allowing the AF to reach the GM terminations using a cortical ROI approach which can be extended to analyze larger study data. Furthermore, we have developed an along-tract parameterization algorithm to quantitatively compare diffusion measures, tract localization and curvature in each hemisphere, for each tractography method considered. To our knowledge, this is the first study which quantitatively compares the localization of right and left AF and which introduces an along-tract parameterization method for AF volumetric tractography data.

2. Material and methods

2.1. Subjects and MRI acquisition

Twenty-nine healthy adult subjects (15 males and 14 females), with a mean age of 38 years, standard deviation 18 years (range: 23–69 years), were recruited by the Functional MR Unit, Department of Biomedical and Neuromotor Sciences of the University of Bologna, among Hospital and University workers and their relatives. Twenty-four were right-handed while five were atypically-handed [28]. A current or past history of neurological or psychiatric disorders and major brain injuries was excluded in all participants by a neurologist (CaT) and signal and/or morphology alterations on brain images were excluded by a neuroradiologist (RL).

Participants underwent a standardized brain MRI protocol including T_1 -weighted and DW imaging. MRI scans were acquired on a 1.5 T General Electric scanner with a birdcage head coil. The T_1 -weighted images were obtained by using the FSPGR (Fast Spoiled Gradient echo) sequence (TI = 600 ms, TE = 5.1 ms, TR = 12.5 ms; FOV = 25.6 × 25.6 cm; 1 mm isotropic voxels). DW-imaging was based on single-shot SE-EPI sequence (TE = 87 ms, TR = 10 s, FOV = 32 × 32 cm, slice thickness = 3.0 mm, in-plane resolution = 1.25 × 1.25 mm²). Diffusion gradients were applied in 64 directions with b-value 900 s/mm² and 7 volumes with null b-value were acquired. The DWI acquisition time was 11 min and 40 s.

For the control of DWI data quality, we performed a detailed visual inspection slice by slice, automatic slice intensity dropout evaluation

and interpolation correction.

The protocol was approved by the local Ethics Committee and written informed consent was obtained from all participants.

2.2. Preprocessing

Eddy-current correction and local fitting of the diffusion tensor parameters was performed using the FDT (FMRIB's Diffusion Toolbox) software library tools (<http://www.fmrib.ox.ac.uk/fsl/fdt/index.html>). For both T_1 -weighted and DW data the Brain Extraction Tool was used to exclude all the non-brain tissue [29]. For each subject, T_1 -weighted and DW images were non-linearly registered by the 3dwarper tool from the Automatic Registration Tool library [30,31].

2.3. Region of interest definition

ROIs were defined in a common standard space (MNI 152 standard template, voxel size 2.0 × 2.0 × 2.0 mm³), to which participants' T_1 -weighted images, previously registered on DW images, were aligned using linear and non-linear registration [32]. We defined:

- The seed mask located in the WM of the AF just anterior to the point where the tract begins to arc towards temporal GM [33] (in green in Fig. 1A).
- Target masks located in the GM of the frontal and temporal lobes, according to the Harvard-Oxford probabilistic atlas which was thresholded at 25% of subjects (in blue in Fig. 1A), adapting the procedure of Galantucci et al. [34].

2.4. Fibre tracking

The tractography of the AF was performed using three different approaches:

- probabilistic tractography based on the ball-and-sticks model - Probtrackx2;
- deterministic tractography with constrained spherical deconvolution - CST_{det};
- probabilistic tractography with constrained spherical deconvolution - CST_{prob}.

The ball-and-stick method estimates anisotropic tensors (sticks) with isotropic background (ball), explicitly modeling local fibre orientation and separating it from isotropic partial volumes. It utilizes a Bayesian estimation of diffusion parameters implemented in FSL (Bedpostx) [35]. Fibre tracking (Probtrackx2) result is an intensity map of probabilistic connections evaluated within each voxel.

CST_{det} was performed using the software package Mrtrix3 (<http://www.mrtrix.org>). It provides an estimate of the FOD (Fibre Orientation Density) function by deconvolving the diffusion signal using non-negatively constrained spherical deconvolution [36], from a response function estimated with the “Tournier” algorithm [37], setting the maximum harmonic degree at $l_{\max} = 8$. Mrtrix3 provides several fibre tracking algorithms, in our study the deterministic SD_Stream algorithm was used for CST_{det} and probabilistic iFOD2 for CST_{prob}. Deterministic streamlines were evaluated by stepping along the local fibre orientation and performing a peak-finding procedure on the FOD once per point [38]; probabilistic streamlines were obtained by iFOD2, via random sampling of the FOD, using the 2nd order integration over fibre orientation distribution [39].

The tracts were delineated starting from the WM seed mask, requiring the streamlines to traverse both frontal and temporal GM targets. Tractography results were thresholded at 10% with respect to the maximum of connectivity within each voxel.

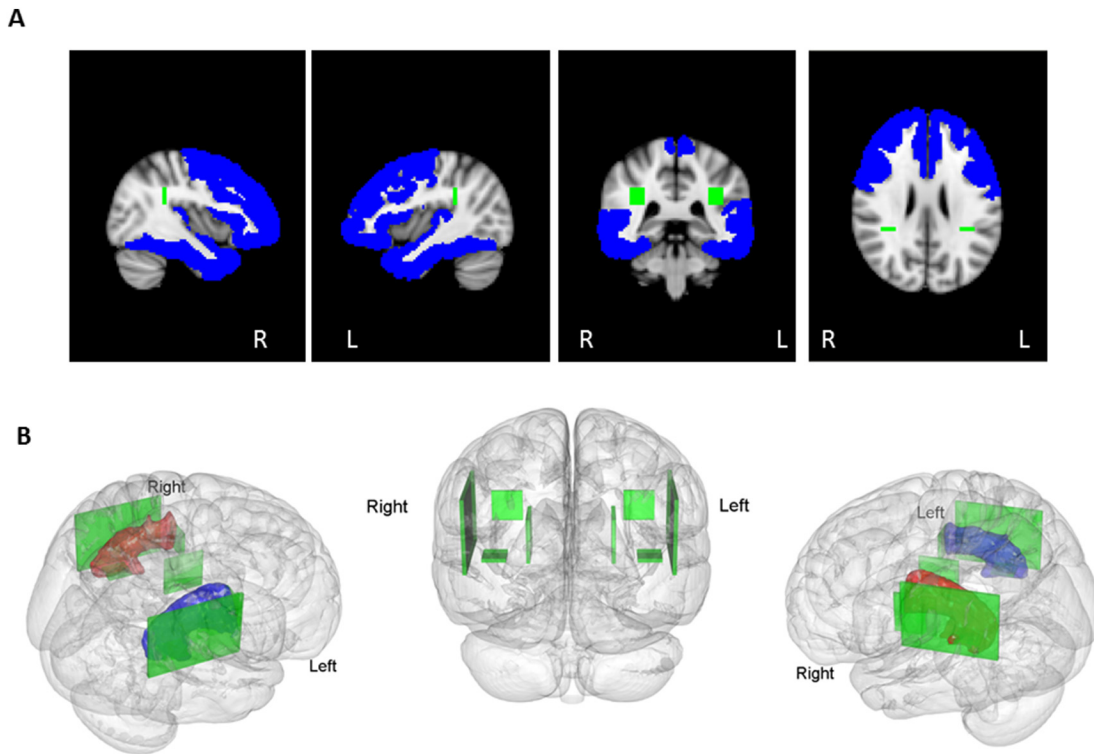


Fig. 1. A Sagittal (R, right and L, left), coronal and axial views of the ROIs used for the AF tractography, drawn on the MNI-152 template. The seed ROI (green) is defined in the WM underlying the angular gyrus; target ROIs (blue) were defined in the frontal and temporal GM according to the Harvard-Oxford probabilistic atlas, thresholded at 25% of subjects.

B 3-dimensional rendering of the left (blue) and right (red) AF core of the group variability maps obtained by CST_{prob} and thresholded at 10% of subjects, isolated by ROIs (green) whose coordinates are given by Giorgio et al. (2010). The central posterior view omits the right and left AF to visualize the localization of ROIs more clearly. (For interpretation of the references to colour in this figure legend, the reader is referred to the web version of this article)

2.5. Tractography analysis

Once the AF was defined, volume and diffusion properties of the tract, estimated as tensor parameters, were evaluated to allow comparison with previous findings in the literature. Eigen-values (λ_1 , λ_2 , λ_3) of the diagonalized diffusion tensor and the invariant indices associated with them, such as fractional anisotropy (FA) and mean diffusivity (MD), were calculated.

Along-tract evaluation of the diffusion parameters was performed in MNI-152 standard template space and restricted to the compact part of the AF bundle, named AF core [16] before its branching towards GM terminations. The AF core was defined by restricting the tract volume within the MNI coordinates using the ROIs defined by Giorgio et al. [33] to restrict the AF WM core tractography (Fig. 1B).

In addition, GM terminations were evaluated with group-variability (GV) maps in MNI-152 space. Inter-subject variability of the AF GM terminations was evaluated using group variability maps thresholded at 10% of subjects. Three-dimensional rendering was performed using the brainR package of the R statistical software [40]. Moreover, to quantitatively evaluate hemispheric asymmetries in AF cortical terminations, we measured tract volume and tractography output in cortical regions, selected from the Harvard-Oxford atlas (see Supplementary Materials – Methods).

2.6. Laplacian parameterization

We developed a parameterization method which can be applied to both deterministic and probabilistic tractography results, to perform along-tract analysis of the diffusion measures and map tract localization.

For this purpose we used the Laplacian spectral graph properties, in particular we evaluated the Fielder vector (ψ) that corresponds to the smallest non-zero eigenvalue. Ψ in graph theory is commonly used to evaluate clustering properties, but its properties can also be used in spectral mesh processing [41]. Several applications for Laplacian spectral properties have also recently been found in neuroimaging [42].

In particular, we used the Laplacian to parameterize the along-tract evolution of the AF. First, we parameterized the AF by modeling its surface in 3-dimensional space. We described the tract surface as triangular meshes and built a connectivity matrix of edges between vertices. The discrete Laplacian operator was calculated on this matrix and its spectrum was evaluated. In particular, ψ can be used to establish an intrinsic coordinate system for elongated tubular structures, where the ψ gradient follows the shape of the object and its maximum and minimum are at the two extremes of the elongated objects [43,44]. We used this property of the ψ gradient to parameterize the AF. First, we evaluated ψ values for each mesh node, and then we sorted ψ values and divided the ψ gradient obtained into fifteen intervals.

Subsequently, the mesh parameterization was projected back to the voxels forming the AF tract volume and each voxel was associated with the nearest mesh vertex of the tract surface. We chose to divide the AF into fifteen segments since it was the maximum number for which a unique association between mesh nodes and voxels within the volume was always preserved for all subjects. This parameterization method (defined as Laplacian parameterization) was applied to the AF core in each hemisphere for all participants. The sorting of the fifteen segments progresses from the frontal to the temporal extremes. We implemented this procedure in Matlab (R2016a).

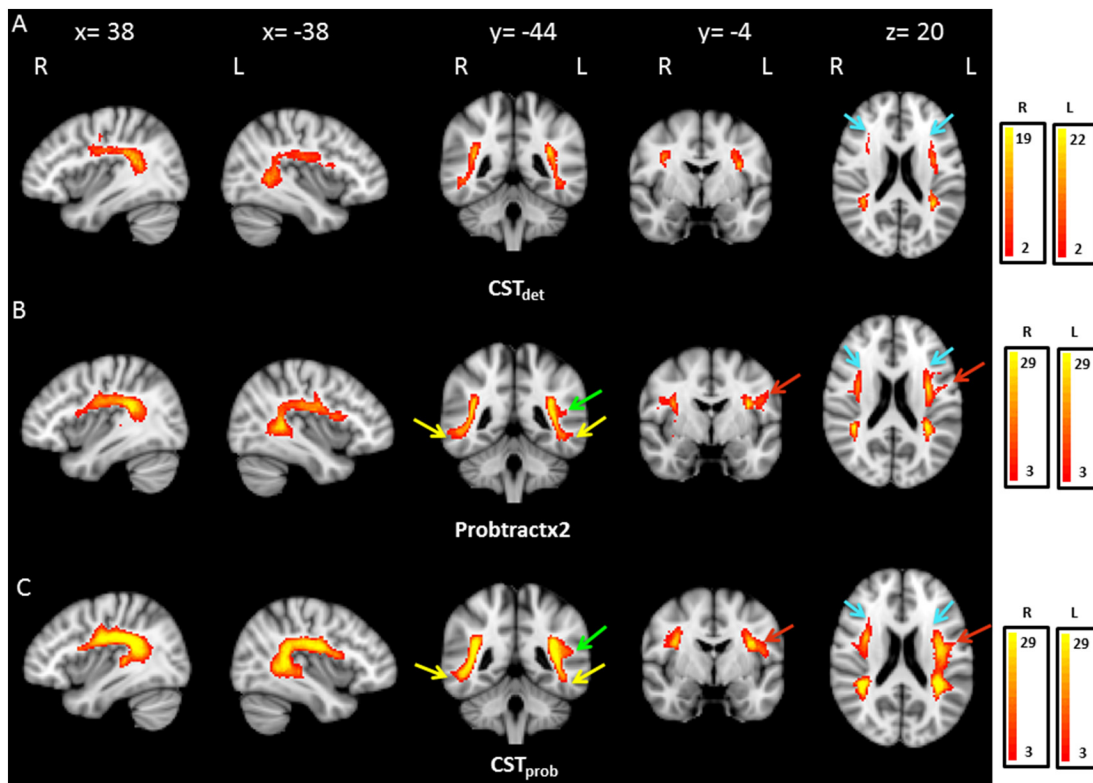


Fig. 2. Sagittal, coronal and axial views of the Group Variability (GV) maps, thresholded at the 10% of subjects, for the different tractography algorithms: CST_{det} (A), Protractx2 (B), CST_{prob} (C). The intensity scales of the maps are associated to the minimum and maximum of the subjects represented by the GV maps. Coordinates of the shown projections are reported in mm in the MNI space. The arrows indicate with different colors characteristic GM terminations of the AF: STG (green), MTG (yellow), PrCG (red) and IFG (turquoise). (For interpretation of the references to colour in this figure legend, the reader is referred to the web version of this article)

2.7. Coordinate system for tract localization

After AF Laplacian parameterization, we evaluated the centroids of each AF segment, obtaining a map of tract coordinates.

- the x-coordinate increases from the midsagittal plane laterally towards either the left and right hemisphere;
- the y-coordinate increases along the postero-anterior direction;
- the z-coordinate increases along the infero-superior direction.

2.8. Statistical analysis

Statistical analyses were conducted with MATLAB R2016a. The Kolmogorov-Smirnov test was performed to test whether diffusion metrics were normally distributed. The median and interquartile values of tract volume and diffusion parameters (FA, MD, λ_1 , λ_2 and λ_3) were calculated, since distributions were non-Gaussian. The analysis has been evaluated in the whole AF core and along the tract in both hemispheres of every subject and for each of the three tractography methods. Right and left AF results of the 29 subjects were compared, using the Wilcoxon signed-rank non-parametric paired test, with a significance level set at $p < 0.05$ corrected by the FDR (False Discovery Rate) method for multiple (segments) comparisons.

Tract curvature was mapped calculating centroids of each Laplacian parametrization segment. Right and left hemisphere tract coordinates of centroids were compared using the Wilcoxon signed-rank test, with the significance level set at $p < 0.05$ corrected by the FDR as above.

3. Results

All DWI volumes images were characterized as being of high quality. We were able to track the AF in both the right and left

hemispheres in all subjects with all the three tractography methods, except for one subject for whom the CST_{det} was not successful in detecting the right AF (male, right handed).

3.1. Group variability maps and cortical projections

Fig. 2 shows GV maps thresholded at the 10% of subjects. With CST_{det} , GV maximum corresponded to 19 subjects in the right and 22 subjects in the left hemisphere. Otherwise, the GV maxima were 29 subjects in both hemispheres for both Protractx2 and CST_{prob} (Fig. 2). The GV maps obtained with both the probabilistic methods had greater volume with respect to GV maps obtained with CST_{det} and while CST_{prob} produced a greater volume compared to Protractx2.

The upper parts of both Fig. 3A and B show the 3D volume rendering of GV maps. The bottom parts of both Fig. 3A and B show sagittal projections of the GV maps to show frontal and temporal GM termination of the AF.

We found GM projections of the AF both in the middle temporal gyrus (MTG) and in the superior temporal gyrus (STG) for both the probabilistic methods (Fig. 2, green arrow STG, yellow arrow MTG), with an increase of the STG connectivity on the left, most evident with the CST_{prob} (Fig. 3B lower).

All the tractography methods, and especially the two probabilistic methods, showed in both hemispheres AF projections towards the inferior frontal gyrus (IFG) (Fig. 2, turquoise arrow IFG), and showed additional projections in the left precentral gyrus (PrCG) (Fig. 2, red arrow PrCG); see also the 3-dimensional rendering of GV maps of the left AF (Fig. 3B upper).

These observations based on GV maps, were also confirmed by quantitative measures of volume and tractography results evaluated in atlas-based cortical regions (see Supplementary Materials – Results).

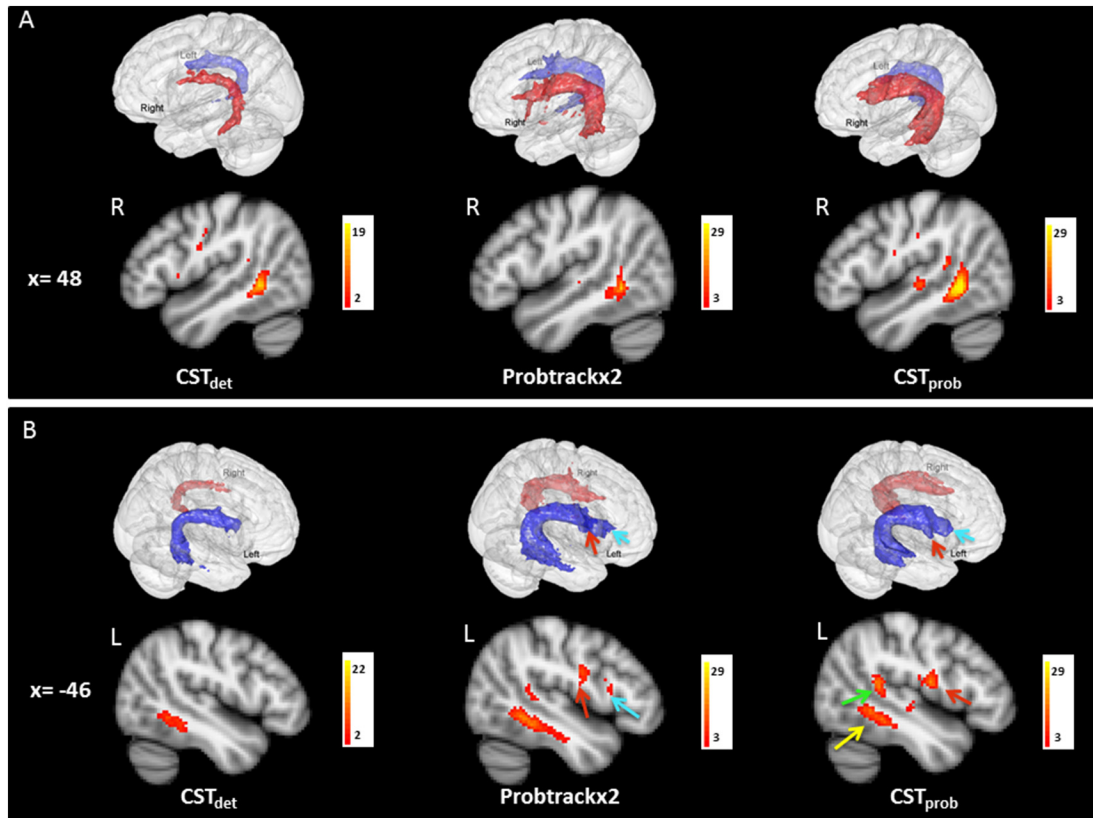


Fig. 3. For both A and B, **upper:** 3-dimensional rendering of GV maps volume for the three tractography algorithms, left AF (blue) and right AF (red); **lower:** GV map of GM projections of the AF, on the MNI-152 brain. **A upper:** right lateral view. **A lower:** right sagittal section. **B upper:** left lateral view. **B lower:** left sagittal section. The angle of view of the 3-dimensional rendering is set individually for each algorithm to better visualize GM projections. The coordinates of the GV projections shown are reported in mm in the MNI space. The colored arrows indicate characteristic GM terminations of the AF: STG (green), MTG (yellow), PrCG (red) and IFG (turquoise). (For interpretation of the references to colour in this figure legend, the reader is referred to the web version of this article)

3.2. Hemispheric asymmetries in the AF core

Evaluating right and left AF differences in the whole tract we included all the subjects for the probabilistic methods whereas for CST_{det} we included 25 subjects because in one case the right AF was absent and in three cases the AF was discontinuous and with more than one bundle making the Laplacian parameterization incompatible with that achieved for other subjects'. The results of the whole core analysis are shown in Table 1.

The AF volume was higher using the probabilistic tractography methods than the deterministic one, especially with CST_{prob} . The tract

volume was significantly bigger in the left AF with Probtrackx2, while there were no significant differences in tract volume between hemispheres with the CST algorithms.

FA differed between the hemispheres only in the CST_{prob} , showing a lower median value of the left FA and correspondingly λ_1 was significantly higher in the right and λ_2 in the left hemisphere. With the CST_{det} we measured higher λ_2 on the left and higher λ_3 on the right; with Probtrackx2 we measured an higher λ_1 and λ_3 on the right, and higher λ_2 on the left. Right and left MD values were not significantly different for any of the three tractography algorithms.

Table 1
Hemispheric asymmetries in the AF core.

Wilcoxon signed rank test results comparing the right and left AF tractography results for the three proposed algorithms (CST_{det} , Probtrackx2, CST_{prob}). In the table, median and interquartile (IR) values of the tract volume and diffusion parameters are shown for the right and left AF. Associated *p*-values are reported as: n.s. not significant, **p*-value < 0.05, ***p*-value < 0.01, ****p*-value < 0.001.

	CST_{det}		Probtrackx2		CST_{prob}				
	Median (IR) right AF	Median (IR) left AF	Median (IR) right AF	Median (IR) left AF	Median (IR) right AF	Median (IR) left AF			
Volume ($mm^3 \times 10^3$)	1.7 (1.1)	2.0 (1.4)	n.s.	2.7 (0.7)	3.5 (0.9)	**	6.3 (1.3)	6.9 (1.5)	n.s.
FA	0.41 (0.04)	0.43 (0.06)	n.s.	0.43 (0.06)	0.43 (0.04)	n.s.	0.41 (0.04)	0.39 (0.04)	***
MD ($mm^2/s \times 10^{-3}$)	0.73 (0.03)	0.73 (0.03)	n.s.	0.73 (0.03)	0.74 (0.03)	n.s.	0.74 (0.03)	0.74 (0.02)	n.s.
λ_1 ($mm^2/s \times 10^{-3}$)	1.10 (0.09)	1.10 (0.08)	n.s.	1.11 (0.08)	1.09 (0.03)	*	1.10 (0.05)	1.05 (0.04)	***
λ_2 ($mm^2/s \times 10^{-3}$)	0.65 (0.05)	0.68 (0.05)	*	0.66 (0.04)	0.68 (0.06)	***	0.67 (0.04)	0.70 (0.04)	***
λ_3 ($mm^2/s \times 10^{-3}$)	0.46 (0.04)	0.42 (0.05)	**	0.45 (0.04)	0.42 (0.04)	*	0.46 (0.04)	0.46 (0.03)	n.s.

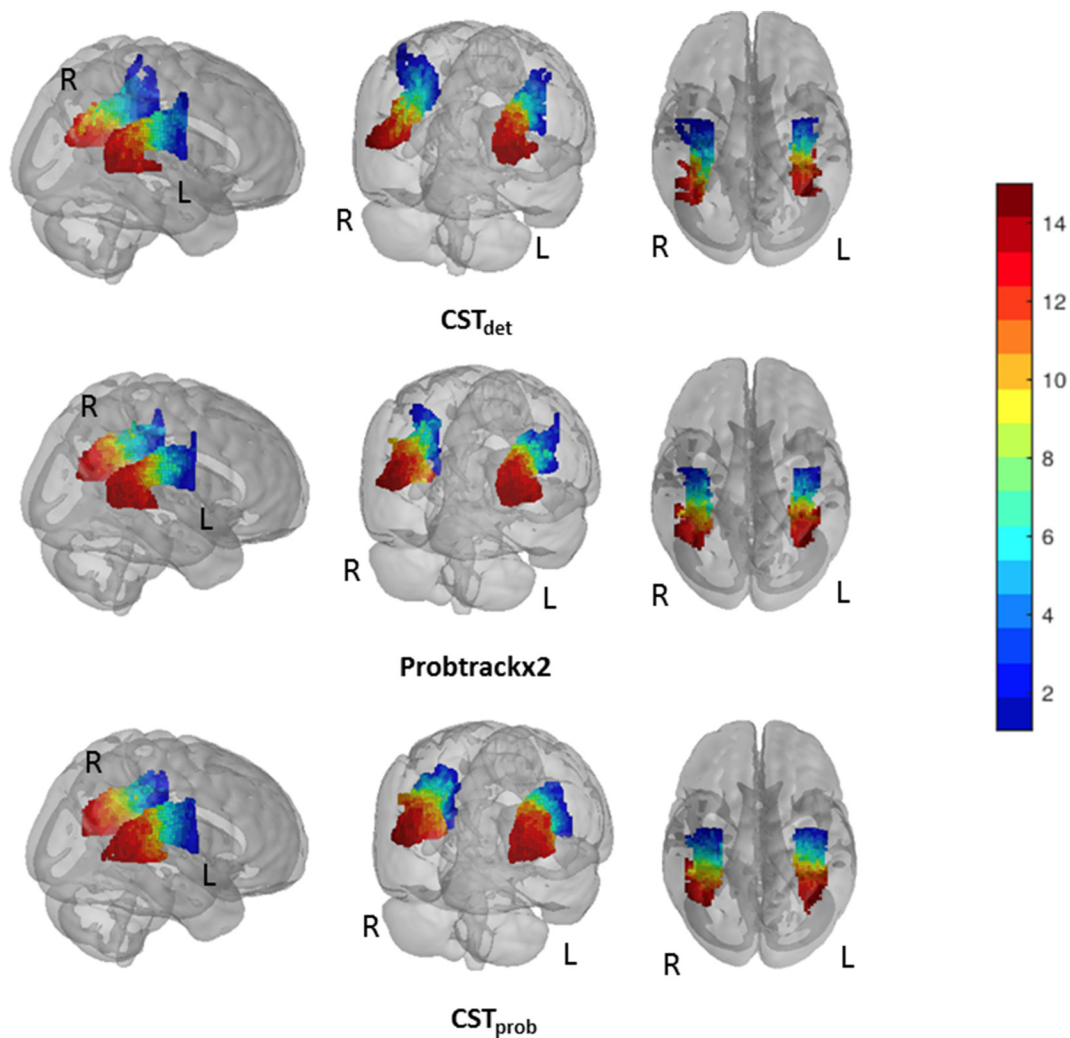


Fig. 4. 3-dimensional rendering of the mean Laplacian parameterization across all the subjects, for each tractography method, dividing the AF into 15 segments (blue = 1st frontal segment, red = 15th temporal segment), projected onto the MNI-152 brain. (For interpretation of the references to colour in this figure legend, the reader is referred to the web version of this article)

3.3. Hemispheric asymmetries in along-tract volume and diffusion measures

Fig. 4 shows the Laplacian parametrization results for the tractography methods. The AF appears to present more isolated branches with the CST_{det} method. For simplicity, we can divide AF segments in three regions: frontal from segments 1 to 7, parietal from 8 to 11 and temporal regions from 12 to 15. Evaluating along-tract volume asymmetries, with CST_{det} and CST_{prob} we measured significant volume differences only in isolated segments, whereas with Probtrackx2 the tract volume was bigger on the left in the temporal region of tract (**Fig. 5**). **Figs. 6–8** show hemispheric asymmetries in the diffusion parameters values calculated for the AF, calculated from each of the three tractography methods.

For CST_{det} (**Fig. 6**), FA was higher on the left in one parietal-temporal segment, MD was higher on the right in parietal-temporal segments and on the left in two temporal segments. No significant differences were found for λ_1 ; λ_2 was higher on the left in one frontal segment, λ_3 was higher on the right in one frontal and some temporal segments.

For Probtrackx2 (**Fig. 7**), FA was higher on the right in some parietal segments, MD was higher on the left in one frontal and one temporal segments, and on the right in two temporal segments. λ_1 was higher on the right in some parietal segments and on the left in one frontal and in

one temporal segments, λ_2 was higher on the left in frontal and parietal segments, λ_3 was higher on the left in one parietal segment and on the right in two temporal segments.

CST_{prob} (**Fig. 8**), FA was higher on the right in frontal and parietal segments, MD was higher on the left in one frontal and in one temporal segments and on the right in some temporal segments. λ_1 was higher on the right in frontal and parietal-temporal segments, and on the left in one temporal segment, λ_2 was higher on the left in some frontal and parietal segments, λ_3 was higher on the right in one frontal segment and on the left in some parietal segments.

3.4. Hemispheric asymmetries in tract localization and curvature

Right and left centroid coordinates presented analogous differences in the three tractography algorithms (**Fig. 9**). The x-coordinate along-tract variations showed an AF midsagittal-lateral curvature which was higher on the left in some frontal segments and on the right in temporal segments. The y-coordinate values decreased from frontal to temporal segments and most of the left segments were located more anteriorly with respect to the right. Finally, the z-coordinate describes the axial tract localization, which was more superior on the right in frontal segments and on the left in some temporal segments.

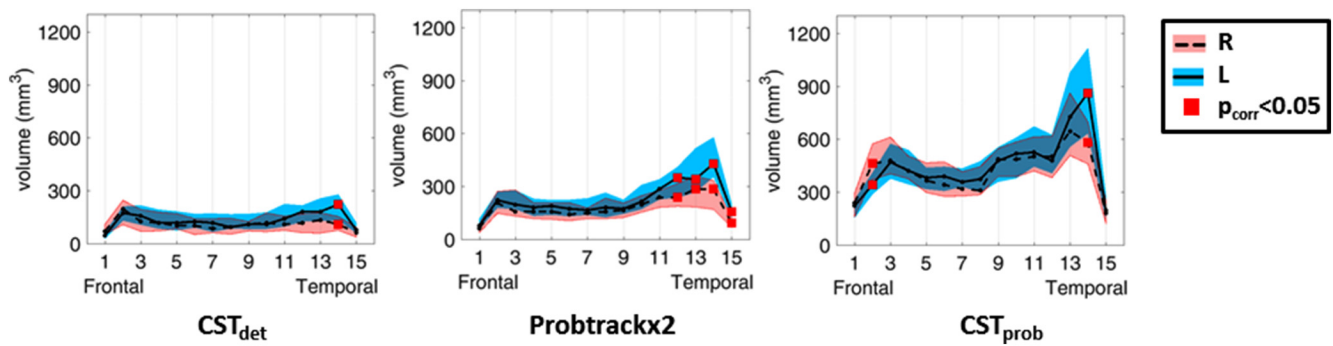


Fig. 5. Along-tract volume comparison between the right (dashed line) and left (continuous line) AF tractography results, for the three algorithms employed (CST_{det} , Probtrackx2, CST_{prob}). In the plot the median volumes are displayed along with the interquartile range (shaded area: red for the right, blue for the left). The red squares mark significant left-right differences with p value < 0.05 after FDR correction. (For interpretation of the references to colour in this figure legend, the reader is referred to the web version of this article)

4. Discussion

In the present study probabilistic tractography methods (Probtrackx2 and CST_{prob}) and deterministic tractography (CST_{det}) were able to tract the AF in both hemispheres (with the exception of one case) in a sizeable sample of healthy subjects. These results are in agreement with recent *post mortem* dissections studies [45] and previous *in vivo* tractography studies using Probtrackx [14] or CST_{prob} [46], whereas the first deterministic tensor tractography studies failed to track the right AF [4,8]. The reason for this discrepancy with the previous deterministic studies could be due to the fact that CST_{det} approach is based on a “higher-order” model that allows the estimation of crossing-fibres [47], a step that is not possible using tensor-based tractography, and probably generates false negative results in the identification of the right AF.

In our study we defined GM target ROIs using the Harvard-Oxford probabilistic atlas to allow for intrinsic hemispheric variability. Seed and targets ROIs were suitable for all the three tractography methods.

Moreover, this procedure limits operator dependence and can be employed in studies with large number of subjects.

Increased STG connectivity on the left was previously observed by Glasser and Rilling [8], who proposed a two-segment model of the AF differentiating the MTG and STG temporal terminations. The STG is thought to be involved in the auditory interface for language, whereas the MTG, in particular its posterior portion, is connected with visual input and is a sound-meaning interface for lexical-semantic functions [48]. We were able to explore whether our data were consistent with the two-segment model, qualitatively using the GV maps, and quantitatively by evaluating the AF intersection with the STG, MTG, PrCG and IFG cortical ROIs (Supplementary Materials). We observed a more left-lateralized STG connectivity, and a balanced bilateral connectivity with the MTG, which is in agreement with fMRI data showing bilateral activation during phonemic tasks [8]. Regarding the IFG and PrCG connections, PrCG has primary importance during early language acquisition and integrates auditory-motor stimuli while IFG connections arise much later in human brain development and are functionally related to

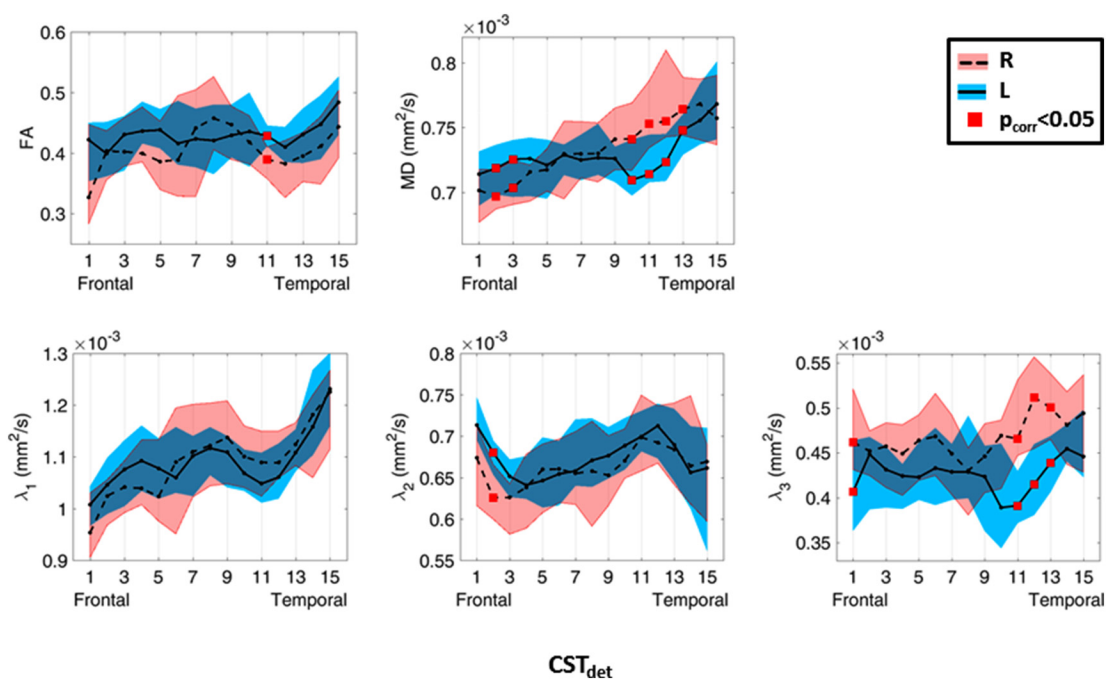


Fig. 6. Along-tract comparison between the right (dashed line) and left (continuous line) AF tractography results, evaluated with the CST_{det} algorithm. Median diffusion parameter values are displayed along with the interquartile range (shaded area: red for the right, blue for the left). The red squares mark significant left-right differences with p value < 0.05 after FDR correction. (For interpretation of the references to colour in this figure legend, the reader is referred to the web version of this article)

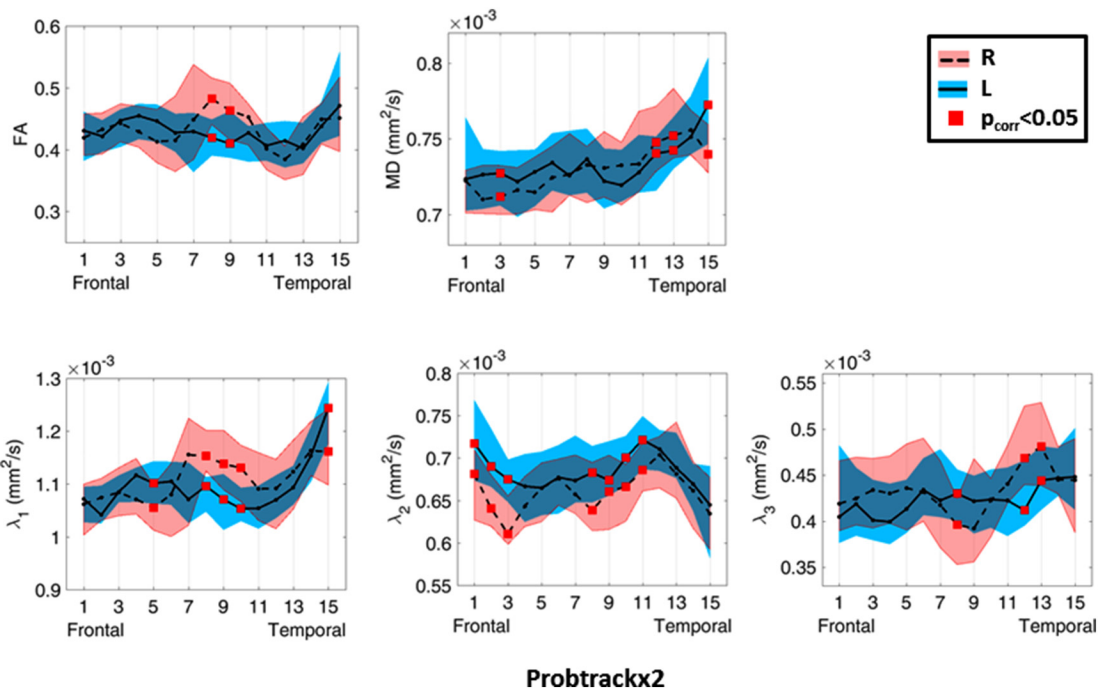


Fig. 7. Along-tract comparison between the right (dashed line) and left (continuous line) AF tractography results, evaluated with the Probtrackx2 algorithm. Median diffusion parameter values are displayed along with the interquartile range (shaded area: red for the right, blue for the left). The red squares mark significant left-right differences with p value < 0.05 after FDR correction. (For interpretation of the references to colour in this figure legend, the reader is referred to the web version of this article)

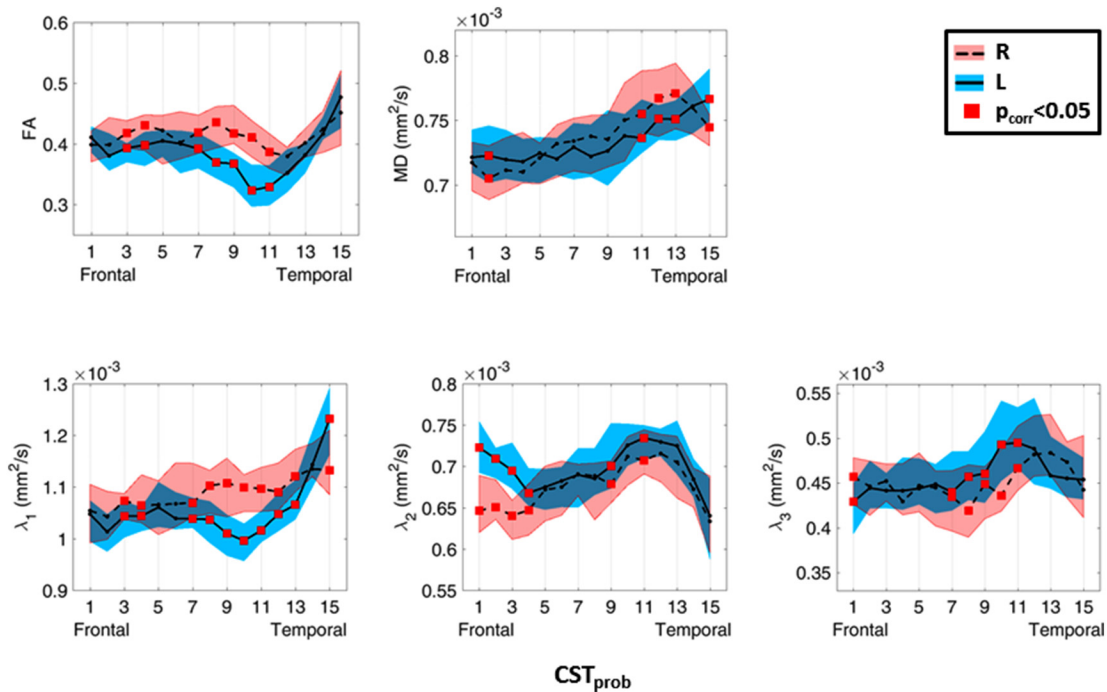


Fig. 8. Along-tract comparison between the right (dashed line) and left (continuous line) AF tractography results, evaluated with the CST_{prob} algorithm. Median diffusion parameter values are displayed along with the interquartile range (shaded area: red for the right, blue for the left). The red squares mark significant left-right differences with p value < 0.05 after FDR correction. (For interpretation of the references to colour in this figure legend, the reader is referred to the web version of this article)

semantic and syntactic language processing [25,26]. Thus, our results are in keeping with the division of the AF into two main routes: STG-PrCG, more evident in the left hemisphere, and MTG-IFG present bilaterally [6,8]. The STG-PrCG stream was detected more robustly by probabilistic tractography methods, Probtrackx2 and CST_{prob} .

The Laplacian parameterization was found to be well-adapted to the geometry of the AF, giving comparable results for different tractographic algorithms (Fig. 4); thus it can be used with different tractography methods, without limitation on fibre-tracking outputs. In general, the Laplacian spectral properties describe invariant geometric

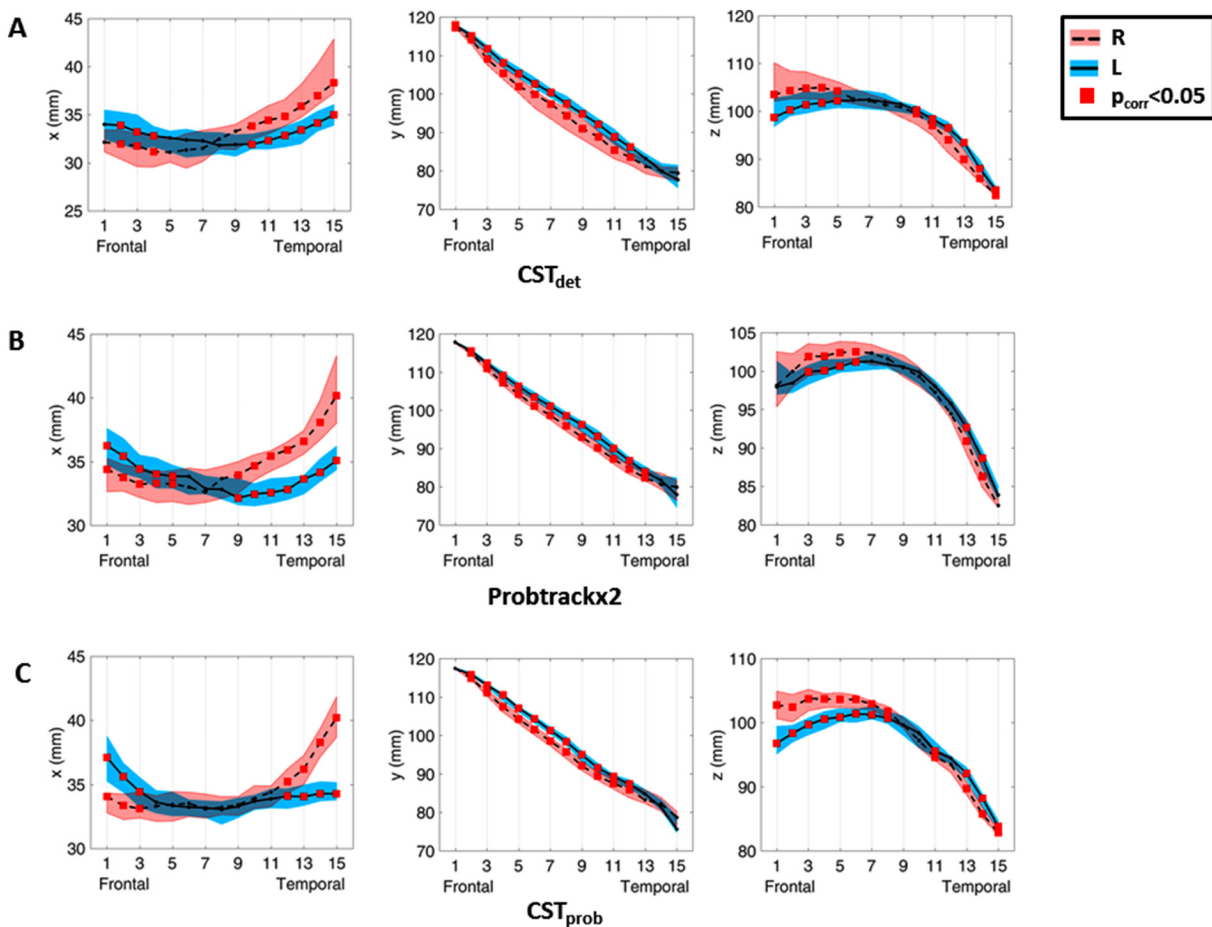


Fig. 9. Centroid coordinates of along-tract segments: the x-coordinate increases symmetrically from the midsagittal plane laterally towards the right and left hemispheres respectively, the y-coordinate increases along the postero-anterior direction and the z-coordinate increases along the infero-superior direction. Right (dashed line) and left (continuous line) tractography results are compared, for the three proposed algorithms: CST_{det} (A), Probtrackx2 (B), CST_{prob} (C). Median coordinate values are displayed along with the interquartile range (shaded area: red for the right, blue for the left). The red squares mark significant left-right differences with p value < 0.05 corrected with FDR for multiple comparisons. (For interpretation of the references to colour in this figure legend, the reader is referred to the web version of this article)

features of objects [41]. In our study the Laplacian parameterization facilitated an along-tract analysis of the AF based on intrinsic and invariant properties due to the elongated and curving geometry of the AF.

The hemispheric comparisons in the whole AF core showed that the different tractography algorithms did not always detect the same differences (Table 1), although they were mostly in agreement in measuring differences of diffusion parameters: higher λ_1 and λ_3 values in the right and higher λ_2 in the left hemisphere.

The Laplacian parameterization allowed localized tract hemispheric asymmetries to be detected. In particular, the left AF core volume was higher mainly in temporal segments with Probtrackx2 (Fig. 5). With the CST_{det} and Probtrackx2 methods we measured an higher λ_3 value on the right in some parietal-temporal segments (Figs. 6, 7). This higher λ_3 measure on the right was also observed in previous along-tract analysis on the AF, performed with the deterministic tensor tractography [16,19]. This finding was associated with the presence of more numerous crossing fibres on the right, complicating the identification of the right AF. With CST_{prob} tractography this difference in the λ_3 diffusivity was not detected, although we measured higher MD values on the right in the same AF segments (Fig. 8). Especially with probabilistic methods we measured a higher λ_2 diffusivity on the left in the most frontal segments of the AF core and in the parietal-temporal segments, where the AF arches through the Sylvian fissure. These differences should be considered in relation to the fact that the left AF showed different GM terminations and the fibres that reach these terminations

could have different orientations, causing an increase in the second axis, λ_2 , of the diffusion tensor. Moreover, the hemispheric differences in λ_2 might be associated with more than one factor, for example the presence of crossing fibres, or a lower fibre density in areas of more divergent AF connectivity to cortical terminations, in the left AF with respect to the right, as observed in particular in the frontal lobe (see PrCG volume - Supplementary Materials). Probably for the same reason, the λ_1 measure was higher on the right in some fronto-parietal segments with Probtrackx2 and CST_{prob} (Figs. 7–8).

Differences between tractography methods in measured diffusion metrics and AF volumes are likely related to the different models behind each implementation. There is a fundamental methodological difference between probtrackx2 and CST methods; in the CST the number of possible fibre populations is estimated directly from the data, while in the ball-and-sticks model, used for probtrackx2, the maximum number of fibres per voxel is predefined. Regarding the two CST variants analyzed, probabilistic methods have been considered more informative than the deterministic tensor-based tractography, particularly in tracking the AF in pathological conditions such as tumor or edema [17]; however for the evaluation of the CST_{det} approach further investigations are necessary. On the other hand, many probabilistic methods have been proposed, and there is no consensus on which could be the best approach [49].

However, a definitive comparison between deterministic and probabilistic methods is only possible when tractography results are

compared with a gold standard. Candidates for a gold standard include *post mortem* axonal tracing, available for primate studies, and *post mortem* studies on humans. Primate *post mortem* axonal tracing studies might be used to define an anatomical reference for humans, but studies have demonstrated important differences between species at the level of AF connectivity [50]. Similarly, a study employing only AF tractography, in chimpanzees and macaques *post mortem* compared with humans *in vivo*, likewise found that AF had different temporal projections [27]. Thus, primate AF anatomy is not the best gold standard for human tractography. Considering *post mortem* studies on humans, Martino et al. [45] were able to detect the AF in both left and right hemispheres, confirming our tractography results, while Geschwind and Levitsky [51], investigating hemispheric asymmetries in the STG, a cortical region connected by the AF, in 100 *post mortem* human brains, found that there was a larger STG area on the left, a result that seems to confirm our findings on asymmetries in AF cortical terminations.

The influence of sex and handedness on brain structural organization is known. Catani et al. [4] reported preliminary findings that females are more likely to have symmetrical pattern of AF connections. Hagmann et al. [52] showed that language processing relies predominantly on the left hemisphere, more in men than in woman, and in right- versus left-handers. In contrast, Allendorfer et al. [53] demonstrated in a group of 240 subjects that there was no association between handedness or sex and AF hemispheric differences. All these works used deterministic tensor tractography. Although the use of probabilistic tractography methods would certainly will give new perspectives in the assessment of these correlations, we did not explore the relationship between the AF asymmetries with sex or handedness because for a robust investigation we need a larger study sample. A larger cohort would also be necessary to explore age covariance in the AF hemispheric asymmetries. Nevertheless, the study of Allendorfer et al. [53] demonstrated that in subjects between the ages of 18 and 76 years there was not a significant correlation of age with possible AF lateralization, although a significant reduction of FA in the arcuate fasciculus had previously been found by Voineskos et al. [54].

To our knowledge, this is the first study which quantitatively assesses spatial localization of the AF, based on the centroid coordinates obtained with the Laplacian parametrization, allowing comparison of the curvature between hemispheres regardless of the choice of tractography algorithm. The left AF showed a lower lateral curvature (x-coordinate), a more dorsal localization (z-coordinate) in the temporal segments, and a higher curvature around the Sylvian fissure towards the STG, while on the right more lateral curvature was observed towards the MTG (Fig. 3). Otherwise, in the frontal segments the AF has a higher lateral curvature (x-coordinate) and a more ventral localization (z-coordinate) on the left (Fig. 9). In fact, the left AF in addition to the IFG termination, also projects laterally and inferiorly towards the PrCG (Fig. 9). For all the tractography methods tried, the y-coordinate showed a more anterior localization for the left compared to the right tract.

4.1. Limitations

Some limitations of the present study should be pointed out, including the non-isotropic voxel of the DW images, the intensity of the static magnetic field (1.5 T) and the relatively low b-value used. On the other hand, the quality of the AF tract reconstructions achieved in our study was optimal, as previously demonstrated with similar acquisition parameters at 1.5 T [13,33,36] and the atlas-based cortical ROI approach allows future applications in larger group including both healthy controls and pathological conditions.

5. Conclusion

In summary, tractography of the AF was successful in both hemispheres using all three fibre-tracking methods tested (CST_{det},

Probtrackx2 and CST_{prob}) at 1.5 T. Several properties of the AF were assessed in detail using an along-tract analysis starting from each of these methods. In each case, bilateral MTG and IFG connectivity was detected, STG and PrCG connectivity being stronger in the left hemisphere using the probabilistic methods. These hemispheric asymmetries in GM terminations caused differences in tract curvature, and the presence of fibres with different orientations resulted in a lower main directionality in the diffusion measures of the left AF.

We quantitatively mapped the geometry of the AF tract using along-tract statistics. To our knowledge this is the first time such a comparison has been made for different fibre-tracking outputs, including Probtrackx2 connectivity maps, thanks to the use of the Laplacian parameterization, suitable for the detection of intrinsic and invariant geometric properties.

This study provides a methodological basis for tract analysis for pre- and post- surgical evaluation in brain tumors, vascular lesions [46] and epilepsy [55] and robust biomarkers for degenerative diseases such as primary progressive aphasia variants both as diagnostic, prognostic and surrogate biomarkers of rehabilitative interventions efficacy [56,57]. Moreover, our approach proved to be accurate in the detection of the hemispheric asymmetries of AF tract geometry and asymmetries that are crucial for language lateralization processes [58].

Funding

The authors declare that they have no sources of funding.

Conflicts of interest

The authors declare that they have no conflict of interest.

Ethical approval

The protocol was approved by the local Ethics Committee and all procedures performed in studies involving human participants were in accordance with the ethical standards of the institutional and/or national research committee and with the 1964 Helsinki declaration and its later amendments or comparable ethical standards.

Informed consent

Informed consent was obtained from all individual participants included in the study.

Appendix A. Supplementary data

Supplementary data to this article can be found online at <https://doi.org/10.1016/j.mri.2018.08.013>.

References

- [1] Geschwind N. Disconnexion syndromes in animals and man. *Brain* 1965;88(2):237–94.
- [2] Catani M, Ffytche DH. The rises and falls of disconnection syndromes. *Brain* 2005;128(Pt 10):2224–39.
- [3] Catani M, Jones DK, Ffytche DH. Perisylvian language networks of the human brain. *Ann Neurol* 2005;57(1):8–16.
- [4] Catani M, Allin MP, Husain M, Pugliese L, Mesulam MM, Murray RM, et al. Symmetries in human brain language pathways correlate with verbal recall. *Proc Natl Acad Sci U S A* 2007;104(43):17163–8.
- [5] Bernal B, Ardila A. The role of the arcuate fasciculus in conduction aphasia. *Brain* 2009;132(Pt 9):2309–16.
- [6] Price CJ. The anatomy of language: contributions from functional neuroimaging. *J Anat* 2000;197(Pt 3):335–59.
- [7] Dick AS, Tremblay P. Beyond the arcuate fasciculus: consensus and controversy in the connective anatomy of language. *Brain* 2012;135(Pt 12):3529–50.
- [8] Glasser MF, Rilling JK. DTI tractography of the human brain's language pathways. *Cereb Cortex* 2008;18(11):2471–82.
- [9] Parker GJ, Luzzi S, Alexander DC, Wheeler-Kingshott CA, Ciccarelli O, Lambon Ralph MA. Lateralization of ventral and dorsal auditory-language pathways in the

- human brain. *NeuroImage* 2005;24(3):656–66.
- [10] Mori S, Crain BJ, Chacko VP, van Zijl PC. Three-dimensional tracking of axonal projections in the brain by magnetic resonance imaging. *Ann Neurol* 1999;45(2):265–9.
- [11] Conturo TE, Lori NF, Cull TS, Akbudak E, Snyder AZ, Shimony JS, et al. Tracking neuronal fiber pathways in the living human brain. *Proc Natl Acad Sci U S A* 1999;96(18):10422–7.
- [12] Basser PJ, Mattiello J, LeBihan D. MR diffusion tensor spectroscopy and imaging. *Biophys J* 1994;66(1):259–67.
- [13] Behrens TE, Berg HJ, Jbabdi S, Rushworth MF, Woolrich MW. Probabilistic diffusion tractography with multiple fibre orientations: what can we gain? *NeuroImage* 2007;4(1):144–55.
- [14] Chen JL, Kumar S, Williamson VJ, Scholz J, Griffiths TD, Stewart L. Detection of the arcuate fasciculus in congenital amusia depends on the tractography algorithm. *Front Psychol* 2015;6:9.
- [15] Chen DQ, Zhong J, Hayes DJ, Behan B, Walker M, Hung PS, et al. Merged group tractography evaluation with selective automated group integrated tractography. *Front Neuroanat* 2016;10:96.
- [16] Yeatman JD, Dougherty RF, Rykhlevskaia E, Sherbondy AJ, Deutsch GK, Wandell BA, et al. Anatomical properties of the arcuate fasciculus predict phonological and reading skills in children. *J Cogn Neurosci* 2011;23(11):3304–17.
- [17] Li Z, Peck KK, Brennan NP, Jenabi M, Hsu M, Zhang Z, et al. Diffusion tensor tractography of the arcuate fasciculus in patients with brain tumors: comparison between deterministic and probabilistic models. *J Biomed Sci Eng* 2013;6(2):192–200.
- [18] Testa C, Evangelisti S, Popeo M, Zanigni S, Gramegna LL, Fantazzini P, et al. The effect of diffusion gradient direction number on corticospinal tractography in the human brain: an along-tract analysis. *MAGMA* 2016;30(3):265–80.
- [19] O'Donnell LJ, Westin CF, Golby AJ. Tract-based morphometry for white matter group analysis. *NeuroImage* 2009;15–45(3):832–44.
- [20] Colby JB, Soderberg L, Lebel C, Dinov ID, Thompson PM, Sowell ER. Long-tract statistics allow for enhanced tractography analysis. *NeuroImage* 2012;59(4):3227–42.
- [21] Hong JH, Kim SH, Ahn SH, Jang SH. The anatomical location of the arcuate fasciculus in the human brain: a diffusion tensor tractography study. *Brain Res Bull* 2009;80(1–2):52–5.
- [22] Huang H, Gundapaneedi T, Rao U. White matter disruptions in adolescents exposed to childhood maltreatment and vulnerability to psychopathology. *Neuropsychopharmacology* 2012;37(12):2693–701.
- [23] Lee DH, Hong CP, Kwon YH, Hwang YT, Kim JH, Park JW. Curvature range measurements of the arcuate fasciculus using diffusion tensor tractography. *Neural Regen Res* 2013;8(3):244–50.
- [24] Dick AS, Bernal B, Tremblay P. The language connectome: new pathways, new concepts. *Neuroscientist* 2014;20(5):453–67.
- [25] Brauer J, Anwander A, Perani D, Friederici AD. Dorsal and ventral pathways in language development. *Brain Lang* 2013;127(2):289–95.
- [26] Friederici AD. The brain basis of language processing: from structure to function. *Physiol Rev* 2011;91(4):1357–92.
- [27] Rilling JK, Glasser MF, Preuss TM, Ma X, Zhao T, Hu X, et al. The evolution of the arcuate fasciculus revealed with comparative DTI. *Nat Neurosci* 2008;11(4):426–8.
- [28] Oldfield RC. The assessment and analysis of handedness: the Edinburgh inventory. *Neuropsychologia* 1971;9(1):97–113.
- [29] Smith SM. Fast robust automated brain extraction. *Hum Brain Mapp* 2002;17(3):143–55.
- [30] Ardekani BA, Braun M, Hutton BF, Kanno I, Iida H. A fully automatic multimodality image registration algorithm. *J Comput Assist Tomogr* 1995;19(4):615–23.
- [31] Manners DN, Testa C, Evangelisti S, Zanigni S, Tonon C, Lodi R. Rapid registration of EPI to high-resolution structural images. Proceedings of the 25th annual meeting of ISMRM. 2017. p. 1452.
- [32] Jenkinson M, Smith S. A global optimization method for robust affine registration of brain images. *Med Image Anal* 2001;5(2):143–56.
- [33] Giorgio A, Watkins KE, Chadwick M, James S, Winmill L, Douaud G, et al. Longitudinal changes in grey and white matter during adolescence. *NeuroImage* 2010;49(1):94–103.
- [34] Galantucci S, Tartaglia MC, Wilson SM, Henry ML, Filippi M, Agosta F, et al. White matter damage in primary progressive aphasia: a diffusion tensor tractography study. *Brain* 2011;134(Pt 10):3011–29.
- [35] Behrens TE, Woolrich MW, Jenkinson M, Johansen-Berg H, Nunes RG, Clare S, et al. Characterization and propagation of uncertainty in diffusion-weighted MR imaging. *Magn Reson Med* 2003;50(5):1077–88.
- [36] Tournier JD, Calamante F, Connelly A. Robust determination of the fibre orientation distribution in diffusion MRI: non-negativity constrained super-resolved spherical deconvolution. *NeuroImage* 2007;35(4):1459–72.
- [37] Tournier JD, Calamante F, Connelly A. Determination of the appropriate b value and number of gradient directions for high-angular-resolution diffusion-weighted imaging. *NMR Biomed* 2013;26(12):1775–86.
- [38] Tournier JD, Calamante F, Connelly A. MRtrix: diffusion tractography in crossing fiber regions. *Int J Imaging Syst Technol* 2012;22(1):53–66.
- [39] Tournier JD, Calamante F, Connelly A. Improved probabilistic streamlines tractography by 2nd order integration over fibre orientation distributions. Proceedings of 18th annual meeting of ISMRM. 2010. 1670.
- [40] Muschelli J, Sweeney E, Crainiceanu C. Brain R: interactive 3 and 4D images of high resolution neuroimage data. *R J* 2014;6(1):41–8.
- [41] Zhang H, Van Kaick O, Dyer R. Spectral mesh processing. *Computer graphics forum Blackwell Publishing Ltd.* 2010;29(6).
- [42] Kim SG, Stelzer J, Bazin PL, Viehweger A, Knösche T. Group-wise analysis on myelination profiles of cerebral cortex using the second eigenvector of Laplace-Beltrami operator. Proceedings of IEEE 11th international symposium on biomedical imaging (ISBI). 2014. p. 1007–10.
- [43] Chung MK, Seo S, Adluru N, Vorperian HK. Hot spots conjecture and its application to modeling tubular structures. *Mach Learn Med Imaging* 2011;7009:225–32.
- [44] Seo S, Chung MK, Whyms BJ, Vorperian HK. Mandible shape modeling using the second eigenfunction of the Laplace-Beltrami operator. *Medical Imaging* 2011;7962:79620Zhttps://doi.org/10.1117/12.877537.
- [45] Martino J, De Witt Hamer PC, Berger MS, Lawton MT, Arnold CM, de Lucas EM, et al. Analysis of the subcomponents and cortical terminations of the perisylvian superior longitudinal fasciculus: a fiber dissection and DTI tractography study. *Brain Struct Funct* 2013;218(1):105–21.
- [46] Mormina E, Longo M, Arrigo A, Alafaci C, Tomasello F, Calamuneri A, et al. MRI Tractography of corticospinal tract and arcuate fasciculus in high-grade gliomas performed by constrained spherical deconvolution: qualitative and quantitative analysis. *AJNR Am J Neuroradiol* 2015;36(10):1853–8.
- [47] Jeurissen B, Descoteaux M, Mori S, Leemans A. Diffusion MRI fiber tractography of the brain. *NMR Biomed* 2017 Sep 25. https://doi.org/10.1002/nbm.3785. (Epub ahead of print).
- [48] Hickok G, Poeppel D. Dorsal and ventral streams: a framework for understanding aspects of the functional anatomy of language. *Cognition* 2004;92(1–2):67–99.
- [49] Maier-Hein KH, Neher PF, Houde JC, Côté MA, Garyfallidis E, Zhong J, et al. The challenge of mapping the human connectome based on diffusion tractography. *Nat Commun* 2017;8(1):1349.
- [50] Thiebaut de Schotten M, Dell'Acqua F, Valabregue R, Catani M. Monkey to human comparative anatomy of the frontal lobe association tracts. *Cortex* 2012;48(1):82–96.
- [51] Geschwind N, Levisky W. Human brain: left-right asymmetries in temporal speech region. *Science* 1968;161(3837):186–7.
- [52] Hagmann P, Cammoun L, Martuzzi R, Maeder P, Clarke S, Thiran JP, et al. Hand preference and sex shape the architecture of language networks. *Hum Brain Mapp* 2006(10):828–35.
- [53] Allendorfer JB, Hernando KA, Hossain S, Nenert R, Holland SK, Szafarski JP. Arcuate fasciculus asymmetry has a hand in language function but not handedness. *Hum Brain Mapp* 2016;37(9):3297–309.
- [54] Voineskos AN, Rajji TK, Lobaugh NJ, Miranda D, Shenton ME, Kennedy JL, et al. Age-related decline in white matter tract integrity and cognitive performance: a DTI tractography and structural equation modeling study. *Neurobiol Aging* 2012;33(1):21–34.
- [55] Takaya S, Liu H, Greve DN, Tanaka N, Leveroni C, Cole AJ, et al. Altered anterior-posterior connectivity through the arcuate fasciculus in temporal lobe epilepsy. *Hum Brain Mapp* 2016;37(12):4425–38.
- [56] Agosta F, Galantucci S, Canu E, Cappa SF, Magnani G, Franceschi M, et al. Disruption of structural connectivity along the dorsal and ventral language pathways in patients with nonfluent and semantic variant primary progressive aphasia: a DT MRI study and a literature review. *Brain Lang* 2013;127(2):157–66.
- [57] Ciccarelli O, Catani M, Johansen-Berg H, Clark C, Thompson A. Diffusion-based tractography in neurological disorders: concepts, applications, and future developments. *Lancet Neurol* 2008;7(8):715–27.
- [58] Forkel SJ, Thiebaut de Schotten M, Dell'Acqua F, Kalra L, Murphy DG, Williams SC, et al. Anatomical predictors of aphasia recovery: a tractography study of bilateral perisylvian language networks. *Brain* 2014;137(Pt 7):2027–39.

Supplementary Materials – Methods

We quantitatively investigated GM terminations by evaluating tract intersection with cortical ROIs from the Harvard-Oxford atlas. In particular, we considered four cortical regions of the atlas (Fig. S1):

- the superior temporal gyrus posterior division (STG);
- the middle temporal gyrus posterior division (MTG);
- the central operculum cortex, under the precentral gyrus (PrCG);
- the frontal operculum cortex as representative of the inferior frontal gyrus (IFG).

Within each cortical region, we measured the AF volume and tractography output normalized by the maximum of connectivity in the whole tract. We evaluated hemispheric asymmetries using the Wilcoxon signed-rank test.

Supplementary Materials – Results

In Table S1, we reported the results of the AF volume and normalized connectivity within cortical ROIs. In STG and PrCG, we measured a significant increase of AF volume and connectivity on the left for all the tractography algorithms. On the contrary, in the MTG terminations we measured an increased AF volume on the right using CST_{prob} , and in the IFG an increased AF volume on the left using CST_{det} .

Fig. S1

We reported cortical regions according to the Harvard-Oxford atlas onto the MNI atlas: STG posterior division (green), MTG posterior division (yellow), central operculum (red) and frontal operculum (light blue).

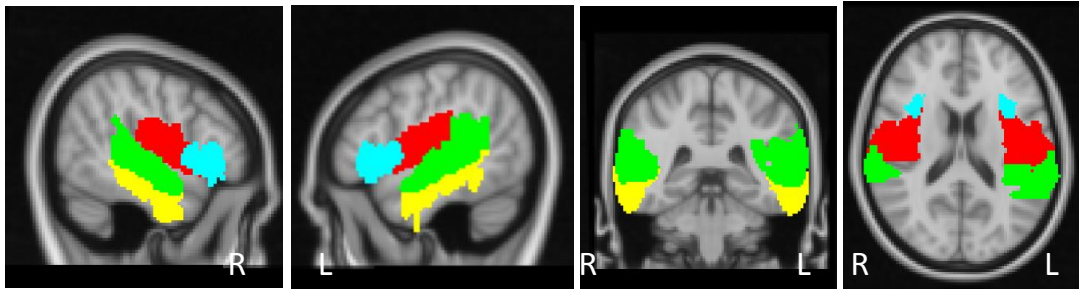


Table S1

Wilcoxon signed rank test results comparing the right and left AF tractography results for the three proposed algorithms (CST_{det} , Probtrackx2 and CST_{prob}). In the table, we show median and interquartile (IR) values of the tract volume and normalized connectivity in different cortical regions (STG posterior, MTG tempo-occipital, medial and frontal operculum), for the right and left AF. Associated p-values are reported as: n.s. not significant, * p-value < 0.05, ** p-value < 0.01, *** p-value < 0.001.

	CST_{det}			Probtrackx2			CST_{prob}		
	Median (IR) right AF	Median (IR) left AF		Median (IR) right AF	Median (IR) left AF		Median (IR) right AF	Median (IR) left AF	
STG volume (mm ³)	0 (24)	336 (336)	***	96 (242)	976 (470)	***	456 (796)	1960 (898)	***
STG connectivity (%)	0 (15)	22 (8)	***	14 (4)	22 (3)	***	14 (2)	22 (5)	***
MTG volume (mm ³)	16 (178)	48 (150)	n.s.	424 (406)	432 (278)	n.s.	552 (430)	280 (212)	***
MTG connectivity (%)	12 (18)	14 (6)	n.s.	15 (3)	15 (3)	n.s.	14 (2)	13 (2)	n.s.
PrCG volume (mm ³)	24 (96)	504 (546)	***	816 (804)	1744 (1004)	***	1040 (794)	2696 (1126)	***
PrCG connectivity (%)	12 (26)	20 (7)	*	19 (6)	23 (4)	*	17 (3)	21 (4)	***
IFG volume (mm ³)	0 (30)	48 (160)	**	272 (622)	448 (582)	n.s.	144 (266)	168 (536)	n.s.
IFG connectivity (%)	0 (15)	14 (19)	n.s.	14 (5)	16 (6)	n.s.	13 (6)	13 (3)	n.s.

LIST OF TABLES

1.1	Mesulam (2003) Primary Progressive Aphasia diagnosis criteria. . . .	10
1.2	Non-fluent or agrammatical PPA variant diagnosis (Gorno-Tempini et al., 2011).	12
1.3	Semantic PPA variant diagnosis (Gorno-Tempini et al., 2011).	13
1.4	Logopenic PPA variant diagnosis (Gorno-Tempini et al., 2011).	14
1.5	Ardila (2010) aphasia syndrome classification.	16
2.1	Demographics features of cortical thickness study participants. . . .	36
2.2	Acquisition parameters T1w - cortical thickness study.	37
2.3	AD vs HC, cortical thickness measures.	41
2.4	PPA vs HC, cortical thickness measures.	42
2.5	PPA vs AD, cortical thickness measures.D	43
2.6	Discriminant function analysis to classify PPA and AD patients. . . .	44
2.7	PPA <i>category world fluency test</i> scores	46
2.8	Cortical thickness and <i>category world fluency test</i> correlations.	46
3.1	Demographic and clinical features of PPA patients - DTI longitudinal study.	50
3.2	Demographic features of HC - DTI longitudinal study.	51
3.3	Acquisition parameters DTI - baseline and 2-years follow-up.	57
3.4	PPA vs HC, language assessment score comparison.	63
3.5	PPA vs HC, DTI measures at baseline.	65
3.6	PPA vs HC, DTI measures at follow-up.	66

3.7	PPA vs HC, DTI measures at longitudinal variation rate.	67
3.8	Mapping language disconnections in PPA.	69
4.1	Stroke patient study: demographic and clinical features.	73
4.2	HC who underwent ASL imaging: demographic features.	74
4.3	Stroke patients WAB-R Aphasic Quotient (AQ).	75
4.4	Acquisition parameters of T1w and ASL imaging.	76
4.5	MRI time post onset (TPO) from stroke.	77
4.6	Correlation of CBF statistics with age in controls.	86
4.7	Significant correlations CBF measures and AQ scale.	91
5.1	HC recruited in the DTI study: demographic features.	94
5.2	Acquisition parameters of DTI	95
5.3	Hemispheric AF asymmetries WM core - volume and DTI metrics . .	107
5.4	Hemispheric UF asymmetries WM core - volume and DTI metrics . .	109
6.1	Acquisition parameters DTI - HCP	114
A.1	Differences for language assessment scores across PPA clinical vari- ants	137
A.2	Differences in DTI metrics across PPA clinical variants	138

LIST OF FIGURES

1.1	Cytoarchitectonic Brodmann areas.	7
1.2	<i>"Anatomie des centres nerveux"</i> white matter fibre representation.	8
1.3	Broca-Wernicke-Geschwind language model.	9
1.4	Cerebral vascular artery territories.	15
1.5	Cortical thickness measure extraction.	20
1.6	Stejskal and Tanner sequence for measuring the diffusion coefficient in MRI.	23
1.7	Schematics for the diffusion ellipsoid eigenvalues.	24
1.8	First diffusion anisotropy index for brain white matter.	25
1.9	Cerebral blood flow quantification using ASL.	26
1.10	Schematics for the language network tracts.	28
1.11	Single and multiple fibre modelling.	31
1.12	Ball and sticks multi-compartment diffusion modelling.	31
1.13	Arcuate <i>post-mortem</i> dissection.	32
1.14	Uncinate <i>post-mortem</i> dissection.	33
2.1	Desikan-Killiany atlas cortical parcelization.	38
2.2	Surface projections of group comparison p-values.	40
2.3	Correlation plots of <i>category world fluency test</i> scores and cortical thickness measures.	47
3.1	Peabody Picture Vocabulary Test items.	55
3.2	Boston Naming Test items.	55

3.3	Pyramids and Palm Trees Test items.	56
3.4	Northwestern Anagram Verbs and Sentence items.	56
3.5	White matter atlas for language network evaluation.	60
3.6	FA-based registration of language tracts.	60
3.7	Arcuate ROI to evaluate DTI measures.	61
3.8	Correlation scatter plots of DTI measures and language assessment.	70
4.1	ASL registration pipeline to MNI space.	79
4.2	T1w and CBF maps of healthy controls.	80
4.3	T1w and CBF maps, at baseline and follow-up, of stroke patients.	81
4.4	T1w and CBF maps, single time point, of stroke patients.	82
4.5	Cerebral vascular artery territory ROIs.	83
4.6	Broca area, Brodmann area 44 and 45	84
4.7	CBF median and standard deviation across healthy controls.	85
4.8	Bilateral CBF ROI statistics in healthy controls.	85
4.9	CBF LI ROI statistics in healthy controls.	86
4.10	Scatter plot of LI MCA and Time Post Onset (TPO) MRI correlation.	87
4.11	Scatter plot LI MCA and AQ recovery.	89
4.12	CBF quantification and LI of the MCA at 6-months follow-up.	90
4.13	LI quantification in CBF ROI at 6-months follow-up.	91
5.1	Tractography ROIs for the AF	97
5.2	Bilateral AF group variability maps.	98
5.3	Bilateral AF 3D-rendering and group variability maps.	99
5.4	Tractography ROIs for the UF.	100
5.5	Bilateral UF group variability maps.	101

5.6	ROI for WM core definition for AF and UF.	103
5.7	Along-AF Laplacian modelling.	104
5.8	Along-UF Laplacian modelling.	105
5.9	Along-AF segment volumes for different tractography methods.	108
5.10	Along-UF segment volume asymmetries.	109
5.11	Along-UF DTI asymmetries.	110
5.12	Asymmetries in UF curvature.	111
6.1	Structural connectome extraction for the HCP dataset.	115
6.2	Cortical projections of connectome principal component.	116
6.3	Principal components related to cortical seed tractography.	117
A.1	Boxplots for WAB Rep and BNT score in HC and PPA variants	135
A.2	Boxplots for PPVT and PVT score in HC and PPA variants	136
A.3	Boxplots for significantly different DTI metrics across PPA variants at the baseline	139
A.4	Boxplots for significantly different DTI metrics across PPA variants at the follow-up and longitudinal variation rate	140

LIST OF ABBREVIATIONS AND ACRONYMS

ACA	Anterior Cerebral Artery
AD	Alzheimer's Disease
AF	Arcuate Fasciculus
AF ant	Arcuate Fasciculus Anterior
AF post	Arcuate Fasciculus Posterior
aPPA	Agrammatic Primary Progressive Aphasia
AQ	Aphasic Quotient
ASL	Arterial Spin Labelling
BNT	Boston Naming Test
CST	Constrained Spherical Deconvolution
DTI	Diffusion Tensor Imaging
DWI	Diffusion Weighted Imaging
FAT	Frontal Aslant Tract
fd _r	False Discovery Rate
fMRI	Functional Magnetic Resonance Imaging
FOD	Fibre Orientation Distribution
FTLD	Fronto Temporal Lobar Degeneration
GM	Grey Matter
HC	Healthy Controls
HCP	Human Connectome Project
ILF	Inferior Longitudinal Fasciculus
IRCCS	Istituti di Ricerca a Carattere Scientifico

IPPA	Logopenic Primary Progressive Aphasia
MCA	Middle Cerebral Artery
MRI	Magnetic Resonance Imaging
LI	Laterality Index
PCA	Posterior Cerebral Artery
PCA	Principal Component Analysis
PPA	Primary Progressive Aphasia
PPT	Pyramids and Palm Trees
PPVT	Peabody Picture Vocabulary Test
ROI	Regions Of Interest
sPPA	Semantic Primary Progressive Aphasia
UF	Uncinate Fasciculus
WAB	Western Aphasia Battery
WAB-Rep	Western Aphasia Battery Repetition
WM	White Matter

BIBLIOGRAPHY

- Abad, V. M., García-Polo, P., O'Daly, O., Hernández-Tamames, J. A., & Zelaya, F. (2016). Asap (automatic software for asl processing): a toolbox for processing arterial spin labeling images. *Magnetic resonance imaging*, 34(3), 334–344.
- Alsop, D. C., Detre, J. A., Golay, X., Günther, M., Hendrikse, J., Hernandez-Garcia, L., Lu, H., MacIntosh, B. J., Parkes, L. M., Smits, M., et al. (2015). Recommended implementation of arterial spin-labeled perfusion mri for clinical applications: a consensus of the ismrm perfusion study group and the european consortium for asl in dementia. *Magnetic resonance in medicine*, 73(1), 102–116.
- Amunts, K., Schleicher, A., Bürgel, U., Mohlberg, H., Uylings, H. B., & Zilles, K. (1999). Broca's region revisited: cytoarchitecture and intersubject variability. *Journal of Comparative Neurology*, 412(2), 319–341.
- Anderson, A. W. (2005). Measurement of fiber orientation distributions using high angular resolution diffusion imaging. *Magnetic Resonance in Medicine: An Official Journal of the International Society for Magnetic Resonance in Medicine*, 54(5), 1194–1206.
- Andreotti, E., Remondini, D., Servizi, G., & Bazzani, A. (2018). On the multiplicity of laplacian eigenvalues and fiedler partitions. *Linear Algebra and its Applications*, 544, 206–222.
- Ardila, A. (2010). A proposed reinterpretation and reclassification of aphasic syndromes. *Aphasiology*, 24(3), 363–394.
- Avants, B. B., Tustison, N. J., Song, G., Cook, P. A., Klein, A., & Gee, J. C. (2011). A reproducible evaluation of ants similarity metric performance in brain image registration. *Neuroimage*, 54(3), 2033–2044.
- Bain, J. S., Yeatman, J. D., Schurr, R., Rokem, A., & Mezer, A. A. (2019). Evaluating arcuate fasciculus laterality measurements across dataset and tractography pipelines. *Human brain mapping*.
- Basser, P. J., Mattiello, J., & LeBihan, D. (1994). Mr diffusion tensor spectroscopy and imaging. *Biophysical journal*, 66(1), 259–267.
- Bates, E., Wilson, S. M., Saygin, A. P., Dick, F., Sereno, M. I., Knight, R. T., & Dronkers, N. F. (2003). Voxel-based lesion-symptom mapping. *Nature neuroscience*, 6(5), 448.

- Behrens, T. E., Berg, H. J., Jbabdi, S., Rushworth, M. F., & Woolrich, M. W. (2007). Probabilistic diffusion tractography with multiple fibre orientations: What can we gain? *Neuroimage*, *34*(1), 144–155.
- Behrens, T. E., Woolrich, M. W., Jenkinson, M., Johansen-Berg, H., Nunes, R. G., Clare, S., Matthews, P. M., Brady, J. M., & Smith, S. M. (2003). Characterization and propagation of uncertainty in diffusion-weighted mr imaging. *Magnetic Resonance in Medicine: An Official Journal of the International Society for Magnetic Resonance in Medicine*, *50*(5), 1077–1088.
- Benjamini, Y., & Hochberg, Y. (1995). Controlling the false discovery rate: a practical and powerful approach to multiple testing. *Journal of the Royal statistical society: series B (Methodological)*, *57*(1), 289–300.
- Bernal, B., & Ardila, A. (2009). The role of the arcuate fasciculus in conduction aphasia. *Brain*, *132*(9), 2309–2316.
- Berthier, M. L. (2005). Poststroke aphasia. *Drugs & aging*, *22*(2), 163–182.
- Black, D., Vachha, B., Mian, A., Faro, S., Maheshwari, M., Sair, H., Petrella, J., Pillai, J., & Welker, K. (2017). American society of functional neuroradiology–recommended fmri paradigm algorithms for presurgical language assessment. *American Journal of Neuroradiology*, *38*(10), E65–E73.
- Castellano, A., Cirillo, S., Bello, L., Riva, M., & Falini, A. (2017). Functional mri for surgery of gliomas. *Current treatment options in neurology*, *19*(10), 34.
- Catani, M. (2017). A little man of some importance. *Brain*, *140*(11), 3055–3061.
- Catani, M., Allin, M. P., Husain, M., Pugliese, L., Mesulam, M. M., Murray, R. M., & Jones, D. K. (2007). Symmetries in human brain language pathways correlate with verbal recall. *Proceedings of the National Academy of Sciences*, *104*(43), 17163–17168.
- Catani, M., & Dawson, M. (2017). Language processing, development and evolution. In *Conn's Translational Neuroscience*, (pp. 679–692). Elsevier.
- Catani, M., & de Schotten, M. T. (2012). *Atlas of human brain connections*. Oxford University Press.
- Catani, M., DellAcqua, F., Vergani, F., Malik, F., Hodge, H., Roy, P., Valabregue, R., & De Schotten, M. T. (2012). Short frontal lobe connections of the human brain. *cortex*, *48*(2), 273–291.

- Catani, M., Howard, R. J., Pajevic, S., & Jones, D. K. (2002). Virtual in vivo interactive dissection of white matter fasciculi in the human brain. *Neuroimage*, *17*(1), 77–94.
- Catani, M., Jones, D. K., & Ffytche, D. H. (2005). Perisylvian language networks of the human brain. *Annals of Neurology: Official Journal of the American Neurological Association and the Child Neurology Society*, *57*(1), 8–16.
- Catani, M., Mesulam, M. M., Jakobsen, E., Malik, F., Martersteck, A., Wieneke, C., Thompson, C. K., Thiebaut de Schotten, M., DellAcqua, F., Weintraub, S., et al. (2013). A novel frontal pathway underlies verbal fluency in primary progressive aphasia. *Brain*, *136*(8), 2619–2628.
- Chappell, M., MacIntosh, B., & Okell, T. (2018). *Introduction to Perfusion Quantification Using Arterial Spin Labelling*. Oxford University Press.
- Chen, J. J., Jann, K., & Wang, D. J. (2015a). Characterizing resting-state brain function using arterial spin labeling. *Brain connectivity*, *5*(9), 527–542.
- Chen, J. L., Kumar, S., Williamson, V. J., Scholz, J., Griffiths, T. D., & Stewart, L. (2015b). Detection of the arcuate fasciculus in congenital amusia depends on the tractography algorithm. *Frontiers in psychology*, *6*, 9.
- Cho-Reyes, S., & Thompson, C. K. (2012). Verb and sentence production and comprehension in aphasia: Northwestern assessment of verbs and sentences (navs). *Aphasiology*, *26*(10), 1250–1277.
- Chung, M. K., Seo, S., Adluru, N., & Vorperian, H. K. (2011). Hot spots conjecture and its application to modeling tubular structures. In *International Workshop on Machine Learning in Medical Imaging*, (pp. 225–232). Springer.
- Colby, J. B., Soderberg, L., Lebel, C., Dinov, I. D., Thompson, P. M., & Sowell, E. R. (2012). Along-tract statistics allow for enhanced tractography analysis. *Neuroimage*, *59*(4), 3227–3242.
- Conturo, T. E., Lori, N. F., Cull, T. S., Akbudak, E., Snyder, A. Z., Shimony, J. S., McKinstry, R. C., Burton, H., & Raichle, M. E. (1999). Tracking neuronal fiber pathways in the living human brain. *Proceedings of the National Academy of Sciences*, *96*(18), 10422–10427.
- De Benedictis, A., Duffau, H., Paradiso, B., Grandi, E., Balbi, S., Granieri, E., Colarusso, E., Chioffi, F., Marras, C. E., & Sarubbo, S. (2014). Anatomic-functional study of the temporo-parieto-occipital region: dissection, tractographic and brain mapping evidence from a neurosurgical perspective. *Journal of anatomy*, *225*(2), 132–151.

- Dejerine, J., & Dejerine-Klumpke, A. (1895). *Anatomie des centres nerveux: Méthodes générales d'étude-embryologie-histogénèse et histologie. Anatomie du cerveau*, vol. 1. Rueff.
- Dell'Acqua, F., Lacerda, L., Barrett, R., D'Anna, L., Tsermentseli, S., Goldstein, L., & Catani, M. (2015). Megatrack: A fast and effective strategy for group comparison and supervised analysis of large-scale tractography datasets. *ISMRM 23th annual meeting, Toronto, Canada, abstract 2843*.
- Dell'Acqua, F., Rizzo, G., Scifo, P., Clarke, R. A., Scotti, G., & Fazio, F. (2007). A model-based deconvolution approach to solve fiber crossing in diffusion-weighted mr imaging. *IEEE Transactions on Biomedical Engineering*, 54(3), 462–472.
- Dell'Acqua, F., & Tournier, J.-D. (2019). Modelling white matter with spherical deconvolution: How and why? *NMR in Biomedicine*, 32(4), e3945.
- Desikan, R. S., Ségonne, F., Fischl, B., Quinn, B. T., Dickerson, B. C., Blacker, D., Buckner, R. L., Dale, A. M., Maguire, R. P., Hyman, B. T., et al. (2006). An automated labeling system for subdividing the human cerebral cortex on mri scans into gyral based regions of interest. *Neuroimage*, 31(3), 968–980.
- Dick, A. S., Bernal, B., & Tremblay, P. (2014). The language connectome: new pathways, new concepts. *The Neuroscientist*, 20(5), 453–467.
- Dick, A. S., & Tremblay, P. (2012). Beyond the arcuate fasciculus: consensus and controversy in the connectonal anatomy of language. *Brain*, 135(12), 3529–3550.
- Dubois, B., Feldman, H. H., Jacova, C., Hampel, H., Molinuevo, J. L., Blennow, K., DeKosky, S. T., Gauthier, S., Selkoe, D., Bateman, R., et al. (2014). Advancing research diagnostic criteria for alzheimer's disease: the iwg-2 criteria. *The Lancet Neurology*, 13(6), 614–629.
- Dunn, L. M., Dunn, D. M., & Lenhard, A. (2007). *Peabody picture vocabulary test: PPVT-4A*. NCS Pearson Minneapolis, MN.
- Eickhoff, S. B., Yeo, B. T., & Genon, S. (2018). Imaging-based parcellations of the human brain. *Nature Reviews Neuroscience*, (p. 1).
- Elahi, F. M., Marx, G., Cobigo, Y., Staffaroni, A. M., Kornak, J., Tosun, D., Boxer, A. L., Kramer, J. H., Miller, B. L., & Rosen, H. J. (2017). Longitudinal white matter change in frontotemporal dementia subtypes and sporadic late onset alzheimer's disease. *NeuroImage: Clinical*, 16, 595–603.

- Fan, L., Li, H., Zhuo, J., Zhang, Y., Wang, J., Chen, L., Yang, Z., Chu, C., Xie, S., Laird, A. R., et al. (2016). The human brainnetome atlas: a new brain atlas based on connectional architecture. *Cerebral cortex*, 26(8), 3508–3526.
- Fischl, B., & Dale, A. M. (2000). Measuring the thickness of the human cerebral cortex from magnetic resonance images. *Proceedings of the National Academy of Sciences*, 97(20), 11050–11055.
- Forkel, S. J., & Catani, M. (2018). Lesion mapping in acute stroke aphasia and its implications for recovery. *Neuropsychologia*, 115, 88–100.
- Forkel, S. J., & Catani, M. (2019). Diffusion imaging methods in language sciences. In *The Oxford Handbook of Neurolinguistics*.
- Forkel, S. J., Thiebaut de Schotten, M., DellAcqua, F., Kalra, L., Murphy, D. G., Williams, S. C., & Catani, M. (2014). Anatomical predictors of aphasia recovery: a tractography study of bilateral perisylvian language networks. *Brain*, 137(7), 2027–2039.
- Fridriksson, J., den Ouden, D.-B., Hillis, A. E., Hickok, G., Rorden, C., Basilakos, A., Yourganov, G., & Bonilha, L. (2018). Anatomy of aphasia revisited. *Brain*, 141(3), 848–862.
- Fridriksson, J., Yourganov, G., Bonilha, L., Basilakos, A., Den Ouden, D.-B., & Rorden, C. (2016). Revealing the dual streams of speech processing. *Proceedings of the National Academy of Sciences*, 113(52), 15108–15113.
- Friederici, A. D. (2011). The brain basis of language processing: from structure to function. *Physiological reviews*, 91(4), 1357–1392.
- Galantucci, S., Tartaglia, M. C., Wilson, S. M., Henry, M. L., Filippi, M., Agosta, F., Dronkers, N. F., Henry, R. G., Ogar, J. M., Miller, B. L., et al. (2011). White matter damage in primary progressive aphasias: a diffusion tensor tractography study. *Brain*, 134(10), 3011–3029.
- Geschwind, N., & Levitsky, W. (1968). Human brain: left-right asymmetries in temporal speech region. *Science*, 161(3837), 186–187.
- Giorgio, A., Watkins, K. E., Chadwick, M., James, S., Winmill, L., Douaud, G., De Stefano, N., Matthews, P. M., Smith, S. M., Johansen-Berg, H., et al. (2010). Longitudinal changes in grey and white matter during adolescence. *Neuroimage*, 49(1), 94–103.
- Glasser, M. F., Coalson, T. S., Robinson, E. C., Hacker, C. D., Harwell, J., Yacoub, E., Ugurbil, K., Andersson, J., Beckmann, C. F., Jenkinson, M., et al. (2016). A multi-modal parcellation of human cerebral cortex. *Nature*, 536(7615), 171.

- Glasser, M. F., & Rilling, J. K. (2008). Dti tractography of the human brain's language pathways. *Cerebral cortex*, *18*(11), 2471–2482.
- Goodglass, H., Kaplan, E., & Weintraub, S. (1983). *Boston naming test*. Lea & Febiger.
- Gorno-Tempini, M. L., Hillis, A. E., Weintraub, S., Kertesz, A., Mendez, M., Cappa, S. F., Ogar, J. M., Rohrer, J., Black, S., Boeve, B. F., et al. (2011). Classification of primary progressive aphasia and its variants. *Neurology*, *76*(11), 1006–1014.
- Hagmann, P., Kurant, M., Gigandet, X., Thiran, P., Wedeen, V. J., Meuli, R., & Thiran, J.-P. (2007). Mapping human whole-brain structural networks with diffusion mri. *PloS one*, *2*(7), e597.
- Hau, J., Sarubbo, S., Houde, J. C., Corsini, F., Girard, G., Deledalle, C., Crivello, F., Zago, L., Mellet, E., Jobard, G., et al. (2017). Revisiting the human uncinate fasciculus, its subcomponents and asymmetries with stem-based tractography and microdissection validation. *Brain Structure and Function*, *222*(4), 1645–1662.
- Heisel, K. A., Goto, J. J., Krishnan, V. V., et al. (2012). Nmr chromatography: molecular diffusion in the presence of pulsed field gradients in analytical chemistry applications.
- Hickok, G., & Poeppel, D. (2004). Dorsal and ventral streams: a framework for understanding aspects of the functional anatomy of language. *Cognition*, *92*(1-2), 67–99.
- Highley, J. R., Walker, M. A., Esiri, M. M., Crow, T. J., & Harrison, P. J. (2002). Asymmetry of the uncinate fasciculus: a post-mortem study of normal subjects and patients with schizophrenia. *Cerebral cortex*, *12*(11), 1218–1224.
- Holmes, C. J., Hoge, R., Collins, L., Woods, R., Toga, A. W., & Evans, A. C. (1998). Enhancement of mr images using registration for signal averaging. *Journal of computer assisted tomography*, *22*(2), 324–333.
- Howard, D., & Patterson, K. (1992). *The Pyramids and Palm Trees Test: A test of semantic access from words and pictures*. Thames Valley Test Company.
- Huang, H., Gundapuneedi, T., & Rao, U. (2012). White matter disruptions in adolescents exposed to childhood maltreatment and vulnerability to psychopathology. *Neuropsychopharmacology*, *37*(12), 2693.
- Huettel, S. A., Song, A. W., McCarthy, G., et al. (2004). *Functional magnetic resonance imaging*, vol. 1. Sinauer Associates Sunderland, MA.

- Johansen-Berg, H., & Behrens, T. E. (2013). *Diffusion MRI: from quantitative measurement to in vivo neuroanatomy*. Academic Press.
- Jones, D. K., Simmons, A., Williams, S. C., & Horsfield, M. A. (1999). Non-invasive assessment of axonal fiber connectivity in the human brain via diffusion tensor mri. *Magnetic Resonance in Medicine: An Official Journal of the International Society for Magnetic Resonance in Medicine*, 42(1), 37–41.
- Kaplan, E., Goodglass, H., & Weintraub, S. (2001). *Boston naming test*. Pro-ed.
- Kellner, E., Dhital, B., Kiselev, V. G., & Reiser, M. (2016). Gibbs-ringing artifact removal based on local subvoxel-shifts. *Magnetic resonance in medicine*, 76(5), 1574–1581.
- Kertesz, A. (2007). *Western aphasia battery: Revised*. Pearson.
- Kertesz, A., Martinez-Lage, P., Davidson, W., & Munoz, D. (2000). The corticobasal degeneration syndrome overlaps progressive aphasia and frontotemporal dementia. *Neurology*, 55(9), 1368–1375.
- Kier, E. L., Staib, L. H., Davis, L. M., & Bronen, R. A. (2004). Mr imaging of the temporal stem: anatomic dissection tractography of the uncinat fasciculus, inferior occipitofrontal fasciculus, and meyers loop of the optic radiation. *American Journal of Neuroradiology*, 25(5), 677–691.
- Kim, J. P., Kim, J., Park, Y. H., Park, S. B., San Lee, J., Yoo, S., Kim, E.-J., Kim, H. J., Na, D. L., Brown, J. A., et al. (2019). Machine learning based hierarchical classification of frontotemporal dementia and alzheimer's disease. *NeuroImage: Clinical*, 23, 101811.
- Kim, S.-G., Stelzer, J., Bazin, P.-L., Viehweger, A., & Knösche, T. (2014). Group-wise analysis on myelination profiles of cerebral cortex using the second eigenvector of laplace-beltrami operator. In *2014 IEEE 11th International Symposium on Biomedical Imaging (ISBI)*, (pp. 1007–1010). IEEE.
- Kiran, S., & Thompson, C. K. (2019). Neuroplasticity of language networks in aphasia: Advances, updates and future challenges. *Frontiers in neurology*, 10, 295.
- Maier-Hein, K. H., Neher, P. F., Houde, J.-C., Côté, M.-A., Garyfallidis, E., Zhong, J., Chamberland, M., Yeh, F.-C., Lin, Y.-C., Ji, Q., et al. (2017). The challenge of mapping the human connectome based on diffusion tractography. *Nature communications*, 8(1), 1349.

- Manners, D. N., Testa, C., Evangelisti, S., Zanigni, S., Tonon, C., & Lodi, R. (2017). Rapid registration of epi to high-resolution structural images. *Proceedings of the 25th annual meeting of ISMRM*, (p. 1452).
- Martino, J., Hamer, P. C. D. W., Berger, M. S., Lawton, M. T., Arnold, C. M., de Lucas, E. M., & Duffau, H. (2013). Analysis of the subcomponents and cortical terminations of the perisylvian superior longitudinal fasciculus: a fiber dissection and dti tractography study. *Brain Structure and Function*, *218*(1), 105–121.
- McKhann, G. M., Knopman, D. S., Chertkow, H., Hyman, B. T., Jack Jr, C. R., Kawas, C. H., Klunk, W. E., Koroshetz, W. J., Manly, J. J., Mayeux, R., et al. (2011). The diagnosis of dementia due to alzheimers disease: Recommendations from the national institute on aging-alzheimers association workgroups on diagnostic guidelines for alzheimer's disease. *Alzheimer's & dementia*, *7*(3), 263–269.
- Mesulam, M.-M. (1982). Slowly progressive aphasia without generalized dementia. *Annals of Neurology: Official Journal of the American Neurological Association and the Child Neurology Society*, *11*(6), 592–598.
- Mesulam, M.-M. (2001). Primary progressive aphasia. *Annals of neurology*, *49*(4), 425–432.
- Mesulam, M.-M. (2003). Primary progressive aphasiaa language-based dementia. *New England Journal of Medicine*, *349*(16), 1535–1542.
- Mesulam, M.-M., Thompson, C. K., Weintraub, S., & Rogalski, E. J. (2015). The wernicke conundrum and the anatomy of language comprehension in primary progressive aphasia. *Brain*, *138*(8), 2423–2437.
- Mito, R., Raffelt, D., Dhollander, T., Vaughan, D. N., Tournier, J.-D., Salvado, O., Brodtmann, A., Rowe, C. C., Villemagne, V. L., & Connelly, A. (2018). Fibre-specific white matter reductions in alzheimers disease and mild cognitive impairment. *Brain*, *141*(3), 888–902.
- Mori, S., Crain, B. J., Chacko, V. P., & Van Zijl, P. C. (1999). Three-dimensional tracking of axonal projections in the brain by magnetic resonance imaging. *Annals of Neurology: Official Journal of the American Neurological Association and the Child Neurology Society*, *45*(2), 265–269.
- Mori, S., Wakana, S., Van Zijl, P. C., & Nagae-Poetscher, L. (2005). *MRI atlas of human white matter*. Elsevier.
- Mormina, E., Longo, M., Arrigo, A., Alafaci, C., Tomasello, F., Calamuneri, A., Marino, S., Gaeta, M., Vinci, S., & Granata, F. (2015). Mri tractography of corticospinal tract and arcuate fasciculus in high-grade gliomas performed by con-

- strained spherical deconvolution: qualitative and quantitative analysis. *American Journal of Neuroradiology*, 36(10), 1853–1858.
- Netter, F. H. (2019). *Atlas d'anatomie humaine*. Elsevier Masson.
- Novelli, G., Papagno, C., Capitani, E., Laiacona, M., et al. (1986). Tre test clinici di ricerca e produzione lessicale. taratura su soggetti normali. *Archivio di psicologia, neurologia e psichiatria*.
- O'Donnell, L. J., Westin, C.-F., & Golby, A. J. (2009). Tract-based morphometry for white matter group analysis. *Neuroimage*, 45(3), 832–844.
- Oldfield, R. C. (1971). The assessment and analysis of handedness: the edinburgh inventory. *Neuropsychologia*, 9(1), 97–113.
- Parker, G. J., Luzzi, S., Alexander, D. C., Wheeler-Kingshott, C. A., Ciccarelli, O., & Ralph, M. A. L. (2005). Lateralization of ventral and dorsal auditory-language pathways in the human brain. *Neuroimage*, 24(3), 656–666.
- Pedersen, P. M., Vinter, K., & Olsen, T. S. (2004). Aphasia after stroke: type, severity and prognosis. *Cerebrovascular Diseases*, 17(1), 35–43.
- Pierpaoli, C., & Basser, P. J. (1996). Toward a quantitative assessment of diffusion anisotropy. *Magnetic resonance in Medicine*, 36(6), 893–906.
- Pierpaoli, C., Mattiello, J., Le Bihan, D., DiChiro, G., & Basser, P. (1994). Diffusion tensor imaging of brain white matter anisotropy. In *13th Annual Meeting of the Society of Magnetic Resonance in Medicine (SMRM)*, (p. 1038).
- Pierpaoli, C., Walker, L., Irfanoglu, M. O., Barnett, A., Basser, P., Chang, L. C., Koay, C., Pajevic, S., Rohde, G., Sarlls, J., & Wu, M. (2010). Tortoise: an integrated software package for processing of diffusion mri data. *ISMRM 18th annual meeting, Stockholm, Sweden, abstract 1597*.
- Qi, T., Schaadt, G., Cafiero, R., Brauer, J., Skeide, M. A., & Friederici, A. D. (2019). The emergence of long-range language network structural covariance and language abilities. *NeuroImage*, 191, 36–48.
- Ridgway, G. R., Lehmann, M., Barnes, J., Rohrer, J. D., Warren, J. D., Crutch, S. J., & Fox, N. C. (2012). Early-onset alzheimer disease clinical variants: multivariate analyses of cortical thickness. *Neurology*, 79(1), 80–84.
- Rilling, J. K., Glasser, M. F., Preuss, T. M., Ma, X., Zhao, T., Hu, X., & Behrens, T. E. (2008). The evolution of the arcuate fasciculus revealed with comparative dti. *Nature neuroscience*, 11(4), 426.

- Robson, H., Specht, K., Beaumont, H., Parkes, L. M., Sage, K., Ralph, M. A. L., & Zahn, R. (2017). Arterial spin labelling shows functional depression of non-lesion tissue in chronic wernicke's aphasia. *cortex*, 92, 249–260.
- Rodrigo, S., Naggara, O., Oppenheim, C., Golestani, N., Poupon, C., Cointepas, Y., Mangin, J., Le Bihan, D., & Meder, J. (2007). Human subinsular asymmetry studied by diffusion tensor imaging and fiber tracking. *American Journal of Neuroradiology*, 28(8), 1526–1531.
- Rogalski, E., Cobia, D., Harrison, T., Wieneke, C., Weintraub, S., & Mesulam, M.-M. (2011). Progression of language decline and cortical atrophy in subtypes of primary progressive aphasia. *Neurology*, 76(21), 1804–1810.
- Rogalski, E., & Mesulam, M. (2009). Clinical trajectories and biological features of primary progressive aphasia (ppa). *Current Alzheimer Research*, 6(4), 331–336.
- Rogalski, E., Rademaker, A., & Weintraub, S. (2007). Primary progressive aphasia: relationship between gender and severity of language impairment. *Cognitive and behavioral neurology: official journal of the Society for Behavioral and Cognitive Neurology*, 20(1), 38.
- Rosen, H., Allison, S., Ogar, J., Amici, S., Rose, K., Dronkers, N., Miller, B., & Gorno-Tempini, M. (2006). Behavioral features in semantic dementia vs other forms of progressive aphasia. *Neurology*, 67(10), 1752–1756.
- Saur, D., Lange, R., Baumgaertner, A., Schraknepper, V., Willmes, K., Rijntjes, M., & Weiller, C. (2006). Dynamics of language reorganization after stroke. *Brain*, 129(6), 1371–1384.
- Seeley, W. W., Crawford, R. K., Zhou, J., Miller, B. L., & Greicius, M. D. (2009). Neurodegenerative diseases target large-scale human brain networks. *Neuron*, 62(1), 42–52.
- Seghier, M. L. (2008). Laterality index in functional mri: methodological issues. *Magnetic resonance imaging*, 26(5), 594–601.
- Seghier, M. L., Ramlakhansingh, A., Crinion, J., Leff, A. P., & Price, C. J. (2008). Lesion identification using unified segmentation-normalisation models and fuzzy clustering. *Neuroimage*, 41(4), 1253–1266.
- Spanò, B., Giulietti, G., Pisani, V., Morreale, M., Tuzzi, E., Nocentini, U., Francia, A., Caltagirone, C., Bozzali, M., & Cercignani, M. (2018). Disruption of neurite morphology parallels ms progression. *Neurology-Neuroimmunology Neuroinflammation*, 5(6), e502.

- Sporns, O. (2010). *Networks of the Brain*. MIT press.
- Sporns, O., Tononi, G., & Kötter, R. (2005). The human connectome: a structural description of the human brain. *PLoS computational biology*, 1(4), e42.
- Staffaroni, A. M., Ljubenkova, P. A., Kornak, J., Cobigo, Y., Datta, S., Marx, G., Walters, S. M., Chiang, K., Olney, N., Elahi, F. M., et al. (2019). Longitudinal multimodal imaging and clinical endpoints for frontotemporal dementia clinical trials. *Brain*, 142(2), 443–459.
- Stejskal, E. O., & Tanner, J. E. (1965). Spin diffusion measurements: spin echoes in the presence of a time-dependent field gradient. *The journal of chemical physics*, 42(1), 288–292.
- Stones, R., Barrett, R., Dallyn, R., Beyh, A., Requejo, F. D. S., Cancemi, D., Leslie, A., Davison, C., Cramer, C., Catani, M., & Dell'Acqua, F. (2019). Megatrack atlas: An online tool for visualisation of large tractography datasets and lesion analysis. *OHBM annual meeting, June 9-13, Rome*.
- Talozzi, L. (2016). *The arcuate fasciculus: an along-tract analysis with white matter probabilistic tractography*. Master's thesis.
- Talozzi, L., Beyh, A., De Santiago Requejo, F., Forkel, J. S., Tonon, C., Testa, C., Dell'Acqua, F., & Catani, M. (2019a). Poster: Intrahemispheric cortical connectivity patterns defined by pca of advanced diffusion tractography. *OHBM annual meeting, June 9-13, Rome*.
- Talozzi, L., Beyh, A., De Santiago Requejo, F., Forkel, J. S., Tonon, C., Testa, C., Lodi, R., Dell'Acqua, F., & Catani, M. (2019b). Poster: Clusterization of cortical areas based on tractography-derived intrahemispheric structural connectivity. *X AIRMM congress, March 28-29, Milan*.
- Talozzi, L., Testa, C., Evangelisti, S., Bianchini, C., Cirignotta, L., Mitolo, M., Fantazzini, P., Tonon, C., Manners, D. N., & Lodi, R. (2018a). E-poster: The uncinate fasciculus: hemispheric asymmetries of dti metrics and curvature mapping. *Joint Annual Meeting ISMRM-ESMRMB, June 16-21, Paris (France)*.
- Talozzi, L., Testa, C., Evangelisti, S., Cirignotta, L., Bianchini, C., Mitolo, M., Brizi, L., Tonon, C., Manners, D. N., & Lodi, R. (2017a). Oral communication: Different tractography methods for bilateral reconstruction of the arcuate fasciculus towards gray matter projections. *VIII AIRMM congress, June 8-9, Gaeta*.
- Talozzi, L., Testa, C., Evangelisti, S., Cirignotta, L., Bianchini, C., Mitolo, M., Brizi, L., Tonon, C., Manners, D. N., & Lodi, R. (2018b). Poster: The uncinate fasciculus: hemispheric asymmetries of dti metrics and trajectory. *IX AIRMM congress, May 10-11, Padova*.

- Talozzi, L., Testa, C., Evangelisti, S., Cirignotta, L., Bianchini, C., Ratti, S., Fantazzini, P., Tonon, C., Manners, D. N., & Lodi, R. (2018c). Along-tract analysis of the arcuate fasciculus using the laplacian operator to evaluate different tractography methods. *Magnetic resonance imaging*, *54*, 183–193.
- Talozzi, L., Testa, C., Manners, N., David, Evangelisti, S., Gramegna, L. L., Bianchini, C., Catani, M., Liguori, R., Pantieri, R., Mitolo, M., Lodi, R., & Tonon, C. (2019c). Poster: Multivariate analysis of left hemisphere cortical thickness discriminates ppa, ad and healthy subjects. *X AIRMM congress, March 28-29, Milan*.
- Talozzi, L., Testa, C., Zanigni, S., Evangelisti, S., Gramegna, L. L., Bianchini, C., Fantazzini, P., Tonon, C., Manners, D. N., & Lodi, R. (2016a). Poster: The arcuate fasciculus: an along-tract analysis with white matter probabilistic tractography. *VII AIRMM congress, February 4-5, Bologna*.
- Talozzi, L., Testa, C., Zanigni, S., Evangelisti, S., Gramegna, L. L., Bianchini, C., Fantazzini, P., Tonon, C., Manners, D. N., & Lodi, R. (2016b). Poster: The arcuate fasciculus: hemispheric asymmetries and gray matter projections evaluation with along-tract and shape dwi based tractography methods. *X BrainModes Meeting, December 1-2, Brussels (Belgium)*.
- Talozzi, L., Testa, C., Zanigni, S., Evangelisti, S., Gramegna, L. L., Bianchini, C., Fantazzini, P., Tonon, C., Manners, D. N., & Lodi, R. (2017b). E-poster: Hemispheric asymmetries and grey matter projections of the arcuate fasciculus: an along-tract study of diffusion and localization properties with deterministic and probabilistic tractography. *25th International Annual Meeting of the ISMRM, April 22-27, Honolulu (USA)*.
- Tatu, L., Moulin, T., Vuillier, F., & Bogousslavsky, J. (2012). Arterial territories of the human brain. In *Manifestations of Stroke*, vol. 30, (pp. 99–110). Karger Publishers.
- Testa, C., Evangelisti, S., Popeo, M., Zanigni, S., Gramegna, L. L., Fantazzini, P., Tonon, C., Manners, D. N., & Lodi, R. (2017). The effect of diffusion gradient direction number on corticospinal tractography in the human brain: an along-tract analysis. *Magnetic Resonance Materials in Physics, Biology and Medicine*, *30*(3), 265–280.
- Tetzloff, K. A., Duffy, J. R., Clark, H. M., Strand, E. A., Machulda, M. M., Schwarz, C. G., Senjem, M. L., Reid, R. I., Spychalla, A. J., Tosakulwong, N., et al. (2017). Longitudinal structural and molecular neuroimaging in agrammatic primary progressive aphasia. *Brain*, *141*(1), 302–317.
- Thiebaut de Schotten, M., Urbanski, M., Batrancourt, B., Levy, R., Dubois, B., Cerliani, L., & Volle, E. (2016). Rostro-caudal architecture of the frontal lobes in humans. *Cerebral Cortex*, *27*(8), 4033–4047.

- Thiebaut de Schotten, M. T., Urbanski, M., Valabregue, R., Bayle, D. J., & Volle, E. (2014). Subdivision of the occipital lobes: an anatomical and functional mri connectivity study. *Cortex*, *56*, 121–137.
- Thompson, C. K., Walenski, M., Chen, Y., Caplan, D., Kiran, S., Rapp, B., Grunewald, K., Nunez, M., Zinbarg, R., & Parrish, T. B. (2017). Intrahemispheric perfusion in chronic stroke-induced aphasia. *Neural Plasticity*, 2017.
- Tournier, J.-D., Calamante, F., & Connelly, A. (2007). Robust determination of the fibre orientation distribution in diffusion mri: non-negativity constrained super-resolved spherical deconvolution. *Neuroimage*, *35*(4), 1459–1472.
- Tournier, J. D., Calamante, F., & Connelly, A. (2010). Improved probabilistic streamlines tractography by 2nd order integration over fibre orientation distributions. In *Proceedings of the international society for magnetic resonance in medicine*, vol. 18, (p. 1670). Ismrm.
- Tournier, J.-D., Calamante, F., & Connelly, A. (2012). Mrtrix: diffusion tractography in crossing fiber regions. *International journal of imaging systems and technology*, *22*(1), 53–66.
- Tournier, J.-D., Calamante, F., & Connelly, A. (2013). Determination of the appropriate b value and number of gradient directions for high-angular-resolution diffusion-weighted imaging. *NMR in Biomedicine*, *26*(12), 1775–1786.
- Tournier, J.-D., Calamante, F., Gadian, D. G., & Connelly, A. (2004). Direct estimation of the fiber orientation density function from diffusion-weighted mri data using spherical deconvolution. *NeuroImage*, *23*(3), 1176–1185.
- Tuch, D. S., Reese, T. G., Wiegell, M. R., Makris, N., Belliveau, J. W., & Wedeen, V. J. (2002). High angular resolution diffusion imaging reveals intravoxel white matter fiber heterogeneity. *Magnetic Resonance in Medicine: An Official Journal of the International Society for Magnetic Resonance in Medicine*, *48*(4), 577–582.
- Tustison, N. J., Cook, P. A., Klein, A., Song, G., Das, S. R., Duda, J. T., Kandel, B. M., van Strien, N., Stone, J. R., Gee, J. C., et al. (2014). Large-scale evaluation of ants and freesurfer cortical thickness measurements. *Neuroimage*, *99*, 166–179.
- Veraart, J., Novikov, D. S., Christiaens, D., Ades-Aron, B., Sijbers, J., & Fieremans, E. (2016). Denoising of diffusion mri using random matrix theory. *NeuroImage*, *142*, 394–406.
- Von Der Heide, R. J., Skipper, L. M., Klobusicky, E., & Olson, I. R. (2013). Dissecting the uncinate fasciculus: disorders, controversies and a hypothesis. *Brain*, *136*(6), 1692–1707.

- White, R. L. (1994). Image restoration using the damped richardson-lucy method. In *Instrumentation in Astronomy VIII*, vol. 2198, (pp. 1342–1348). International Society for Optics and Photonics.
- Yeatman, J. D., Dougherty, R. F., Myall, N. J., Wandell, B. A., & Feldman, H. M. (2012). Tract profiles of white matter properties: automating fiber-tract quantification. *PloS one*, 7(11), e49790.
- York, G. K., & Steinberg, D. A. (2006). An introduction to the life and work of john hughlings jackson with a catalogue raisonné of his writings.
- Zhang, H., Schneider, T., Wheeler-Kingshott, C. A., & Alexander, D. C. (2012). Noddi: practical in vivo neurite orientation dispersion and density imaging of the human brain. *Neuroimage*, 61(4), 1000–1016.
- Zhang, H., Van Kaick, O., & Dyer, R. (2010). Spectral mesh processing. In *Computer graphics forum*, vol. 29, (pp. 1865–1894). Wiley Online Library.
- Zhang, J. (2019). *Applications of NODDI for imaging in vivo white matter pathology in neurodegenerative diseases*. Ph.D. thesis, UCL (University College London).
- Zilles, K., & Amunts, K. (2010). Centenary of brodmann’s mapconception and fate. *Nature Reviews Neuroscience*, 11(2), 139.

CURRICULUM VITAE

Lia Talozzi

Date of birth: 21st March 1992

Home Street
Via Metauro 22,
Peglio (PU) IT.
+39 3291332001
liatalozzi@gmail.com

Work at
Dep. of Biomedical and
Neuromotor Sciences,
Bologna University
lia.talozzi2@unibo.it

Education and Training

- 10/2019(expected) PhD, Alma Mater Studiorum, University of Bologna; Biomedical and Neuromotor Sciences.
- 06/2019 Research programme, King's College London, Pyschiatry.
- 04/2016 MA Alma Mater Studiorum, Univeristy of Bologna; Applied Physics.
- 2015-*in itinere* Internship at the Functional MR Unit, Department of Biomedical and Neuromotor Sciences, University of Bologna.
- 10/2013 BA Alma Mater Studiorum, University of Bologna; Physics.
- 04/2013 X-ray absorbtion measurement training, ESRF (European Synchrotron Radiation facility) in Grenoble, France.
- 7/2010 High school degree, Liceo Classico Raffaello, Urbino; Classical studies.

Multicenter collaborations

- 2016-*in itinere* Member of the Ataxia group in the Enhancing Neuro Imaging Genetics Through Meta Analysis (ENIGMA) consortium, University of South California.
- 08/2018 Collaborator contract (12 months) for the Italian IRCCS Multi-center Imaging Project, IRCCS *Istituto delle Scienze Neurologiche di Bologna*, Bellaria Hospital.

Grants

- 2019 **Guarantors of brains travelling grant** to attend the OHBM 25th annual meeting presenting the poster *Intra-hemispheric cortical connectivity patterns defined by pca of advanced diffusion tractography*, 9-13/06/2019, Rome (Italy).
- 2019 **AIRMM grant 2019** - from the Italian Association of Magnetic Resonance in Medicine (AIRMM) to attend the X AIRMM congress, presenting the poster *Multivariate analysis of left hemisphere cortical thickness discriminates PPA, AD and healthy subjects*, Italian ISMRM Chapter, 28-29/03/2019, Milan (Italy).
- 2018 **Marco Polo 2018** - International Research Exchange Scholarship which cover a six months period (1/9/2018 to 28/2/2019), at the Neuroanatomy and Tractography Laboratory, Kings College London, tutor Prof. Marco Catani.
- 2018 **Educational stipend** - to attend the Joint Annual Meeting ISMRM-ESMRMB, presenting the E-poster *The uncinate fasciculus: hemispheric asymmetries of DTI metrics and curvature mapping*, 16-21/06/2018, Paris, (France).
- 2017 **Educational stipend** to attend the 25th ISMRM Annual Meeting and Exhibition, presenting the E-poster *Hemispheric asymmetries and grey matter projections of the arcuate fasciculus: an along-tract study of diffusion and localization properties with deterministic and probabilistic tractography*, 22-27/04/2017, Honolulu (USA).

Doctoral Research

- Title:** Advanced neuroimaging methodologies to improve connectivity detection in normal and abnormal language brain networks
- Thesis advisors:** Primary Advisor, MD PhD Prof. Caterina Tonon
Secondary Advisor, PhD Claudia Testa

Peer Reviewed Publications

1. Evangelisti S, Pittau F, Testa C, Rizzo G, Gramegna LL, Ferri L, Coito A, Cortelli P, Calandra-Buonaura G, Bisquoli F, Bianchini C, Manners DN, **Talozzi L**, Tonon C, Lodi R, Tinuper P. *L-Dopa Modulation of Brain Connectivity in Parkinson's Disease Patients: A Pilot EEG-fMRI Study*. Front Neurosci. 2019 Jun 14;13:611. doi: 10.3389/fnins.2019.00611. eCollection 2019. PubMed ID [31258465](https://pubmed.ncbi.nlm.nih.gov/31258465/).

2. Mitolo M, Stanzani-Maserati M, Capellari S, Testa C, Rucci P, Poda R, Oppi F, Gallassi R, Sambati L, Rizzo G, Parchi P, Evangelisti S, **Talozzi L**, Tonon C, Lodi R, Liguori R. *Predicting conversion from mild cognitive impairment to Alzheimer's disease using brain (1)H-MRS and volumetric changes: A two-year retrospective follow-up study*. *Neuroimage Clin*. 2019 Apr 30;23:101843. doi: 10.1016/j.nicl.2019.101843. PubMed PMID [31071594](#).
3. Testa C, Calandra-Buonaura G, Evangelisti S, Giannini G, Provini F, Ratti S, Cecere A, **Talozzi L**, Manners DN, Lodi R, Tonon C, Cortelli P. *Stridor-related gray matter alterations in multiple system atrophy: A pilot study*. *Parkinsonism Relat Disord*. 2019 May;62:226-230. doi: 10.1016/j.parkreldis.2018.11.018. Epub 2018 Nov 17. PubMed PMID: [30509725](#).
4. **Talozzi L**, Testa C, Evangelisti S, Cirignotta L, Bianchini C, Ratti S, Fantazzini P, Tonon C, Manners DN, Lodi R. *Along-tract analysis of the arcuate fasciculus using the Laplacian operator to evaluate different tractography methods*. *Magn Reson Imaging*. 2018 Dec;54:183-193. doi: 10.1016/j.mri.2018.08.013. Epub 2018 Aug 27. PubMed PMID: [30165094](#).
5. Morisi R, Manners DN, Gnecco G, Lanconelli N, Testa C, Evangelisti S, **Talozzi L**, Gramegna LL, Bianchini C, Calandra-Buonaura G, Sambati L, Giannini G, Cortelli P, Tonon C, Lodi R. *Multi-class parkinsonian disorders classification with quantitative MR markers and graph-based features using support vector machines*. *Parkinsonism Relat Disord*. 2018 Feb;47:64-70. doi: 10.1016/j.parkreldis.2017.11.343. Epub 2017 Nov 28. PubMed PMID: [29208345](#).